DETERMINING THE INTRINSIC PROPERTIES OF THE C1B DOMAIN THAT INFLUENCE PKC LIGAND SPECIFICITY AND SENSITIVITY TO REACTIVE OXYGEN SPECIES

A Dissertation

by

MIKAELA DANIELLE STEWART

Submitted to the Office of Graduate Studies of
Texas A&M University
in partial fulfillment of the requirements for the degree of

DOCTOR OF PHILOSOPHY

Chair of Committee,	Tatyana I. Igumenova
Committee Members,	Gregory D. Reinhart
	Ryland Young
	Janet Bluemel
Head of Department,	Gregory D. Reinhart

August 2013

Major Subject: Biochemistry

ABSTRACT

Each member of the protein kinase C (PKC) family activates cell signaling pathways with different and sometimes opposing cell functions, such as cell division, migration, or death. Because of the importance of these processes in human diseases and disorders like cancer, stroke, and Alzheimer's disease, there is a need for drugs which modify the action of PKC. However, drug design is difficult due to the complicated nature of PKC regulation.

To better understand the differential regulation of PKC activity, these studies probe the structure, dynamics, and reactivity of one of the domains responsible for PKC regulation, C1B. C1B binds signaling molecules and translocates PKC to membranes in order to release the kinase domain from inhibition. Mutagenesis and ligand-binding assays monitored with fluorescence and nuclear magnetic resonance (NMR) techniques show that a single variable residue in C1B dramatically affects the sensitivity to signal activators. Investigation of the domain structure and dynamics using NMR revealed the identity of this residue alters the dynamics of the activator binding loops, without changing the structure. NMR studies of the C1B variants in membrane-mimicking micelles showed this residue also changes the interaction of the regulatory domain with lipids. These results demonstrate PKC isoforms have evolved specific functions by tuning dynamics and membrane affinity.

Alternatively, PKC can be activated by reactive oxygen species by a mechanism that does not require binding of signaling molecules or membrane localization. To

investigate the role of C1B in this type of signaling, the regulatory domain reactivity is monitored via NMR and gel electrophoresis. These studies reveal a particular cysteine residue in C1B that is most reactive, an alternative conformation of C1B in which this residue is more exposed, and modification of C1B leads to unfolding and zinc loss. Because the regulatory domains are responsible for auto-inhibition of the kinase domain, C1B unfolding provides a plausible explanation for activation of PKC by reactive oxygen species.

The relation of the intrinsic C1B properties to the activation of PKC can be used to develop drugs with a single mechanism and to better understand how closely related signaling proteins develop specific functions.

ACKNOWLEDGEMENTS

I would like to thank my committee chair and principle investigator, Dr. Tatyana Igumenova, and my committee members, Dr. Reinhart, Dr. Young, and Dr. Bluemel, for their training and guidance throughout the course of this research and my graduate studies. I appreciate the other members of the Igumenova Laboratory for their feedback and for keeping me grounded. Thanks also go to the faculty and staff that work hard to make the Biochemistry and Biophysics Department a great place to learn and work.

I also want to extend my gratitude to Texas A&M Biochemistry and Biophysics Department, National Science Foundation, PEO International, and National Institutes of Health for funding this research. I want to recognize Dr. Mauricio Lasagna and the Reinhart Laboratory for fluorescence training and use of their fluorometer. I acknowledge my collaborators, Dr. Francesca Massi and Dr. Brittany Morgan, for performing molecular dynamic simulations of C1B.

Final thanks go to my parents and friends for their encouragement and to my husband, Jared, for his proof-reading, support, patience, and love.

NOMENCLATURE

14-doxyl PC	1-Palmitoyl-2-Stearoyl-(14-Doxyl)-sn-Glycero-3-Phosphocholine
CPMG	Carr-Purcell-Meiboom-Gill
CRIP	Cysteine-Rich Intestinal Protein
DAG	Diacylglycerol
DARR	Dipolar Assisted Rotational Resonance
DMSO	Dimethyl Sulfoxide
DOG	1,2-Dioctanoyl-sn-Glycerol
DPC	Dodecylphosphocholine
DPS	2-Dihexanoyl-sn-Glycero-3-[Phospho-L-Serine]
DTT	1,4-Dithiothreitol
EDTA	Ethylenediaminetetraacetic
fHSQC	Fast Heteronuclear Single Quantum Coherence
HDex	Hydrogen-Deuterium Exchange
HSQC	Heteronuclear Single Quantum Coherence
IAC	Iodoacetamide
IPAP	In-Phase Anti-Phase
IPTG	Isopropyl-D-1-Thiogalactopyranoside
KSR	Kinase Suppressor of Ras
MES	2-(N-Morpholino)Ethanesulfonic Acid
MRCK	CDC42-Binding Protein Kinases

NMR	Nuclear Magnetic Resonance
NOE	Nuclear Overhauser Effect
OD	Optical Density
P13A	Phorbol 13-Acetate
PAR	4-(2-Pyridylazo)-Resorcinol
PC	Phosphatidylcholine
PDB	Protein Data Bank
PDB ID	Protein Data Bank Identification Number
PDBu	Phorbol 12,13-Dibutyrate
PE	Phorbol Ester
PEG-mal	Polyethylene Glycol Maleimide
PG	Phosphatidylglycerol
PKC	Protein Kinase C
PKD	Protein Kinase D
PLC	Phospholipase C
PRE	Paramagnetic Relaxation Enhancement
PS	Phosphatidylserine
Pyk2	Proline-Rich Tyrosine Kinase 2
RACK	Receptor for Activated C-Kinase
RAG-1	Recombination Activating Gene Product
Ras GRP	Ras Guanyl Nucleotide-Releasing Protein
RDC	Residual Dipolar Coupling

sub-ns	Sub-Nanosecond
SUMO	Small Ubiquitin-Like Modifer
TCEP	Tris(2-Carboxyethyl)phosphine
WT	Wild-Type

TABLE OF CONTENTS

Page

Page

LIST OF FIGURES

Page

Page

Page

LIST OF TABLES

Page

CHAPTER I

INTRODUCTION

PKC function and regulation

Since the discovery of protein kinase C (PKC) as the target of the tumor promoting plant compounds called phorbol esters, it has been the subject of much research. PKC is a family of highly regulated multi-modular serine/threonine kinases that act in cell signaling. PKC proteins phosphorylate a diverse group of protein targets, playing a role in several cell signaling pathways such as: adhesion, migration, transformation, apoptosis, and cell cycle checkpoint.[1-3] Regulation of signaling is achieved through maturation of PKC by phosphorylation,[4] differential cell localization through interactions with other anchoring proteins,[5] and an autoinhibitory region that responds to second messengers. Misregulation of PKC has been implicated as a contributing factor to cardiovascular disease, cancer progression, mental illness, and Alzheimer's disease.[6-9] However, a better understanding of PKC regulation is required to effectively utilize PKC activation or inhibition as a disease therapy. For this reason, this dissertation is focused on differentiating the roles that one of the domains in the autoinhibitory region plays in activation of PKC family members in the presence of various ligands/ activators.

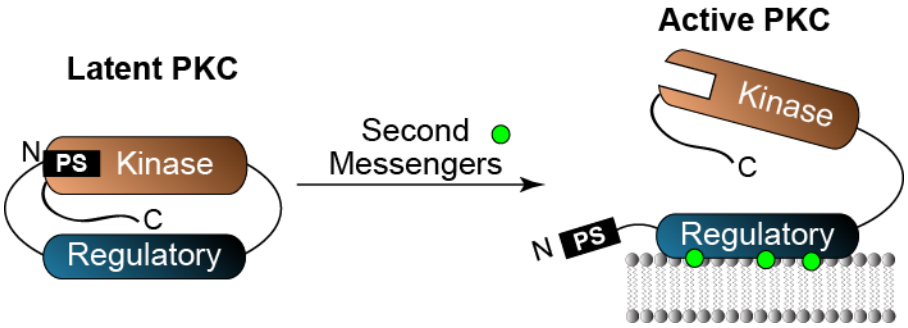

Figure 1. Model of PKC autoinhibition. "PS" represents the pseudo-substrate region. "N" and "C" mark the N- and C- termini. Domains not to scale.

A model of PKC regulation by the autoinhibitory region is shown in Figure 1. The N-terminal autoinhibitory region in the latent cytosolic PKC, places the pseudo-substrate region in the catalytic active site located on the C-terminal kinase domain. This inhibits the activity of the mature phosphorylated form of PKC until the regulatory domains within the autoinhibitory region bind to second messengers. This localizes the protein to the membrane and releases the pseudo-substrate domain so that the kinase domain is available to bind and phosphorylate the substrate.[10] There are at least 10 isoforms of PKC in humans which are divided into three sub-classes based upon the composition of the regulatory domains: conventional, novel, and atypical.

Conventional PKC's, such as α, βI, βII, and γ, contain three independently folded and conserved domains in the regulatory region called C1A, C1B, and C2 (Figure 2). The C2 domain binds to calcium allowing it to associate with the phosphatidylserine (PS) containing plasma membrane.[11] Next, the C1 domains bind to diacylglycerol (DAG), which releases the pseudo-substrate region to fully activate conventional PKC.[12] DAG and calcium are both products of phosphatidylinositol triphosphate cleavage by

phospholipase C (PLC), which makes conventional PKC isoforms unique in their ability to respond specifically to this signaling source.

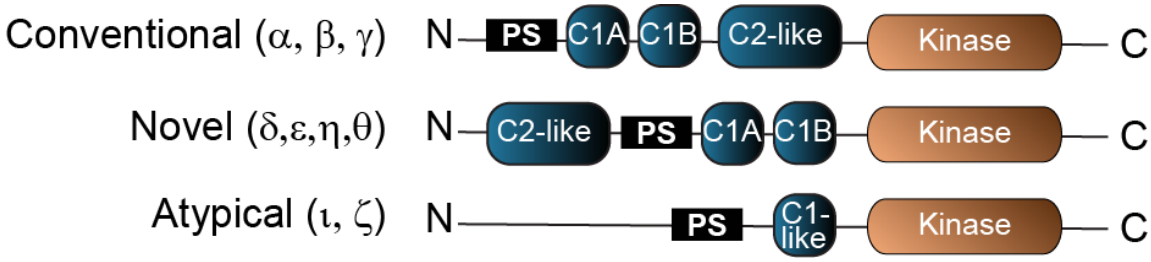

Figure 2. PKC subfamilies categorized by regulatory domains. "PS" represents the pseudo-substrate region. "N" and "C" mark the N- and C- termini. Domains not to scale.

Novel PKC isoforms (δ, ε, η, θ) shown in Figure 2 have a C2-like domain that does not bind calcium, and therefore C1A and C1B are solely responsible for membrane binding and activation. However, the C2-like domain plays a role in PKC activation through protein-protein interactions and/or associates with acidic components in membranes.[13] Due to higher DAG affinities, the novel PKC isoforms are localized to subcellular compartments which contain high local concentrations of DAG, such as the Golgi, endoplasmic reticulum, or nucleus, even with basal levels of PLC or phosphatidic acid phosphatase signaling.[14,15] Some novel isoforms then translocate to the plasma membrane when DAG concentrations are high during PLC or phosphatidic acid phosphatase signaling similar to conventional isoforms.[16]

Atypical PKC isoforms (ζ, ι) do not respond to changes in calcium or DAG concentrations because they do not contain a C2 domain and possess only a C1-like domain (Figure 1). Atypical PKC isoforms are regulated through protein-protein

interactions which occur in regions of the regulatory domain, as well as interactions between the C1-like domain with the kinase domain or ceremide.[17,18]

The arrangement of the domains in the latent PKC that promotes the pseudo-substrate interaction with the active site is not known for any PKC isoforms. Recently, the first structure of a complete PKC protein was determined to 4.0 Å resolution using x-ray diffraction and small-angle X-ray scattering.[19] However, because C2 was bound to calcium, this structure represents an intermediate in the activation pathway and does not contain any inter-regulatory domain interactions. Binding and PKC activation studies have shown that a C1A to C2 domain interaction occurs in the absence of DAG signaling and maintains the PKC latent state.[20,21] The binding interface and the changes that occur due to ligand binding have still yet to be elucidated. The dynamics and flexibility between the domains as well as the overall instability makes studying the full length PKC difficult. For this reason, the work presented here was carried out on either the C1B domain or the joint C1B-C2 domain, in attempts to apply the knowledge learned to the overall PKC activation mechanism.

C1 domains

There are 15 structures from different C1 domains deposited in the protein data bank (PDB), two are crystal structures and the rest were determined with NMR. Figure 3A shows the structures of the C1B domains from novel PKCδ determined by x-ray crystallography [22] and conventional PKCα determined by NMR (PDB ID = 2ELI, lowest energy structure). These structures demonstrate the common features seen for all known C1 structures: a β-sheet core with a C-terminal α-helix, two zinc coordination sites

which maintain the fold, and what is best described as an unzipped β-sheet that forms two ligand binding loops referred to as β12 and β34. The backbone structures are super-imposable with an RMSD of 1.8 Å and the greatest variability is in the β34 ligand binding loop.

In spite of the structural similarities, the affinity of C1 domains for DAG varies over several orders of magnitude between C1 domains from different isoforms and between C1A and C1B of the same isoform.[23,24] The crystal structure of PKCδ C1B domain bound to a water soluble phorbol ester shows that the ligand is hydrogen bonded to the amide backbone of three residues in the ligand binding loops: T242, L251, and G253.[22] Phorbol esters are tumor promoting plant compounds that constitutively activate PKC. Ligand binding, either phorbol ester or DAG, is thought to conceal a hydrophilic patch between the loops allowing the hydrophobic side-chains to interact with membranes. However, there are no structures available of DAG bound C1 or C1 bound to any ligands in the presence of membrane-mimics. Several non-DAG-binding C1 domains homologous to the atypical PKC isoforms (PKCζ and PKCι) have also been identified, such as those in c-Raf, kinase suppressor of Ras (KSR), and Vav. The loss of conventional DAG binding is attributed to either missing residues in the β34 loop (c-Raf and KSR)[25] or replacement of the hydrophobic residues with hydrophilic residues (Vav and atypical PKC).[26,27] While it is clear the β34 loop contributes to ligand binding, the relationship between the subtle differences in the loops of various C1 domains and the drastic difference in ligand affinities is unclear.

The sequence within the ligand binding loops of novel and conventional C1 domains is 30% identical and 46% similar, compared to the overall 26% identity and 50% similarity of the entire domain as shown in Figure 3B. Conserved residues include the zinc coordination residues (highlighted in green), a PT pair at the C-terminal hinge of the β12 loop, and the QG motif on the C-terminal hinge of the β34 loop (all highlighted in pink). Interestingly, only one of the residues hydrogen bonding to phorbol ester in the crystal structure is conserved amongst all phorbol ester binding C1 domains. However, there is a distinct trend in the 22nd C1 residue, located in the N-terminal hinge of the β34 loop (labeled in Figure 3A and highlighted in yellow in Figure 3B). C1 domains which contain a tryptophan at position 22 have a high affinity for DAG, such as those in novel PKC isoforms or conventional PKC C1A domains. Conversely, conventional PKC C1B domains, with a tyrosine at position 22 bind weakly to DAG even though they bind tightly to phorbol ester. Mutation of this residue, Tyr123 in the conventional C1Bβ to Trp and Trp252 in the novel C1Bδ to Tyr, led to reversed ligand affinity and specificity.[28] This residue does not contact the ligand in any known C1-ligand complexes; therefore it is unclear why its identity affects ligand binding. The work in chapter II attempts to elucidate the role that this residue plays to tune DAG affinity. This knowledge used in combination with the role of lipid binding determined in chapter III, will be a powerful tool in designing C1 domain isoform specific drugs.

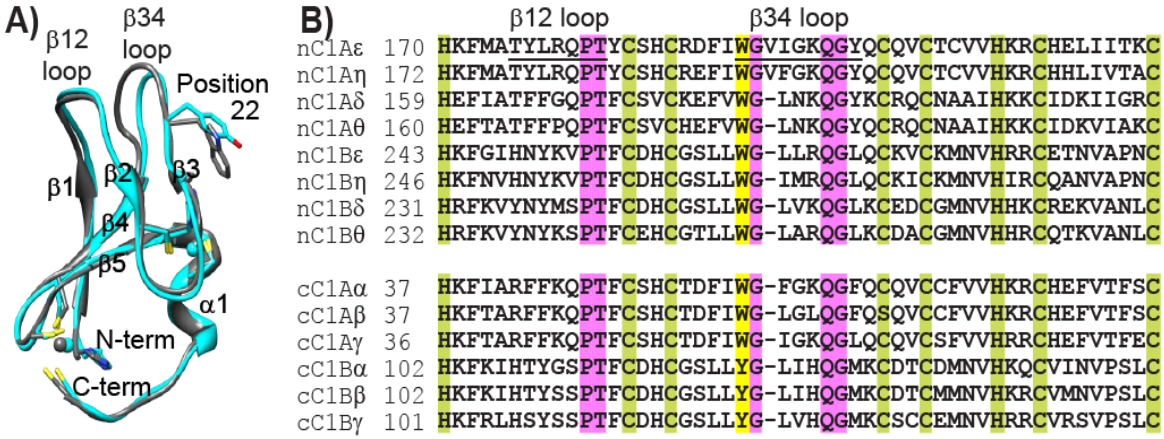

Figure 3. C1 domain structure and sequence comparison. A) Structure alignment of a C1B domains from a novel PKCδ (crystal structure PDB ID: 1PTQ) and a conventional PKCα (NMR structure PDB ID: 2ELI) with the termini, secondary structure, and position 22 labeled. B) Sequence alignment of all C1A and C1B from novel ("n") and conventional ("c") PKC isoforms of *Rattus norvegicus*. Zinc coordinating residues are highlighted in green, conserved loop residues in pink, and position 22 in yellow. The ligand binding loops are labeled and underlined in nC1Aε.

C1 domain as a drug target

Since the discovery of the PKC membrane targeting C1 domain as the receptor for tumor-promoting phorbol esters, C1 has been an attractive drug target. One of the major challenges with this approach is that in addition to the various C1 domain physiological ligands and functions, many of the C1 domains are promiscuous with several possible ligands. The diacylglycerol-binding C1 domains of PKC have been reported to bind not only to phorbol ester, diacylglycerol (DAG), and their analogs, but also interact with macrocyclic lactones, indolactams, iridals, polyacetates, alcohols, and other proteins. To complicate matters further, the affinity to a given ligand varies dramatically between the different domains. For example, while both of the tandem C1 domains from the PKC γ, δ, ε, η, and θ isoforms have a high affinity for DAG, only the

first C1 domain (C1A) in PKCα and PKCβ maintain this high affinity. However, the second C1 domain (C1B) from PKCα and PKCβ has a higher affinity to phorbol ester than the C1A domains. The various PKC isoforms activate different signaling pathways, bringing about sometimes opposing cellular events. An effective drug must be able to act specifically on the intended isoform, but there are still many questions as to what dictates C1 domain ligand affinities and specificities.

In spite of these challenges, several natural products have been found to effectively target C1 and treat devastating human diseases. Ingenol-3-angelate (PEP005) derived from plant sap has been used successfully as a topical treatment for skin cancers.[29] It was shown to act via binding to the C1 domain to activate PKCδ.[30] In addition to prevention of tumor growth, marine microbe produced bryostatins are a promising treatment for cognitive impairment. At low doses, bryostatin-1 selectively binds and activates C1 domains of PKCδ and PKCε, which up-regulates the α-secretase amyloid processing pathway, decreasing the formation of plaques found in Alzheimer's disease.[31] Treatment of transgenic Alzheimer's diseased mice with bryostatin-1 prevented synaptic loss, plaque deposition, and memory deficits.[32] Similarly, when given to rats after a stroke, bryostatin-1 improved learning and memory, prevented the loss of neurons, and restored the spines and synapses of dendrites.[33,34] Prostratin, a C1 domain-binding drug isolated from tree bark, has potential to eradicate HIV in infected individuals. It has been shown to induce expression of latent HIV proviruses in T-cells, making infected cells susceptible to the current antiretroviral therapy.[35] While treatment with prostratin activates multiple PKC isoforms, this effect has been attributed to

activation of novel PKC(s).[36] These studies conducted using natural products demonstrate the potential human health benefit that could come of designing drugs to target C1 domains.

Current efforts focus on chemical modification of these and other known C1 ligands to increase PKC isoform specificity. For example, compounds referred to as DAG-lactones are made by circularizing DAG and subsequent modification of the exposed chemical functional groups. C1 domains bind to DAG-lactones with multiple orders of magnitude higher affinity than to DAG, and some have shown promising selectivity among the PKC isoforms.[37] A branched DAG-lactone (HK654) reduced tumor growth in two human prostate cancer cell lines by specifically activating PKCα, demonstrating the potential DAG derivatives have for development of cancer treatment.[38]

Analogs of the naturally occurring high affinity ligands have also been made by substituting different functional groups;[39] however, these molecules have a large number of asymmetric centers, resulting in complicated synthesis. Studies using modified phorbol esters and the naturally occurring variations point to the hydrophobicity of the side-chain being a major factor dictating tumor promotion versus tumor inhibition.[40,41] Indolactam, a natural occurring tumor promoter, was modified to form benzolactam and subsequently to form 8-octyl-benzolactam-V9 which shows selective binding to the C1B domain of novel PKC isoforms and selectively translocates two of the novel PKC isoforms.[42] As mentioned above, bryostatin has already been proven to be a useful drug without modification, however synthesized bryostatin analogs have been designed which

can be produced in larger quantities and exhibit isoform selectivity.[43] Because C1 domains are not only found in all twelve human PKC isoforms, but also several other signaling proteins, designing specific activators or inhibitors for this domain could have an even further reaching impact.

Homologous DAG-binding C1 domains have been found in several other types of mammalian proteins such as protein kinase D (PKD), chimaerins, Ras guanyl nucleotide-releasing proteins (Ras GRP), Munc-13, DAG kinases, and the CDC42-binding protein kinases (MRCK). Like PKC, many of these protein families have potential as cancer treatment targets. PKD inhibitors have proven effective against prostate and pancreatic cancer, but the search for selective inhibitors is still ongoing.[44] β2-chimaerin is down regulated in several types of cancer, and overexpression has been shown to stop breast cancer cell proliferation.[45] Conversely, Ras GRP3 is overexpressed in several types of cancer, and down regulation led to a decreased cancer phenotype in a human prostate cancer cell line.[46] DAG kinases regulate the other DAG signaling pathways by depleting DAG levels, and have recently been implicated in hepatocellular carcinoma progression.[47] Knockdown of MRCKα/β isoforms along with inhibition of ROCK prevented colorectal carcinoma cell invasion[48] and decreased breast cancer cell invasion.[49] The functional diversity of these C1 domains containing proteins and their link to multiple cancer types provides even more motivation for development of selective activators and inhibitors. The work presented here is a significant step in determining factors that dictate the differences in affinity and specificity of C1 domains for ligands and lipids.

Zinc coordination in the C1 domain

In addition to investigations of C1 domain ligand and lipid binding properties in Chapters II and III, properties of C1B that allow for activation of PKC by reactive oxygen species are also characterized in Chapter IV. Results show a specific zinc-coordinating cysteine residue makes C1B susceptible to reactive oxygen species. The coordination number and geometry of this zinc site change depending on the environmental conditions. In order to put this work into the context of the large field of zinc coordinating proteins, a brief introduction to the types and properties of zinc binding sites is presented here.

C1 domains are just one of the many types of proteins which coordinate zinc. It is estimated that 10% of the human proteome is made up of zinc binding proteins.[50] Zinc sites in proteins are classified according to their biological function as catalytic, regulatory, or structural zinc sites. Catalytic zinc sites contain three or four protein ligands of histidine, glutamate, aspartate, or sometimes cysteine residues and almost always one water molecule. To aid in catalysis, the zinc acts as a Lewis acid and the water is hydrolyzed to a hydroxide ion, polarized to act as a base, or displaced so that zinc stabilizes a negative reaction product. A thorough review of catalytic zinc sites in all six types of enzyme families has been written by David Auld.[51]

Regulatory zinc sites are found in proteins responsible for zinc storage or transport. These proteins function to ensure zinc is available for the proteins that require it, but not free in an uncoordinated form in the cell because of its toxicity.[52] This family varies wildly in the identity and number of residues coordinating zinc, in order to

accommodate both weak binding in the case of zinc transport and tight binding in the case of zinc scavenging.

C1 domains belong to the largest class of zinc binding proteins, which are those with structural zinc sites, often referred to as zinc fingers.[50] In this class of proteins the zinc is present to stabilize the proper fold of the protein. Molecular dynamics simulations of a zinc finger revealed that zinc binds at an early stage of folding and facilitates the formation of the native protein structure.[53] Zinc fingers are important for many cellular processes such as transcription regulation, metabolism, and signal transduction.[51] They are characterized by the presence of a four residue zinc binding motif that is made up of a combination of cysteine and histidine residues. In "classical" zinc fingers the zinc binding motif is close together in primary structure, with only a couple residues separating the zinc ligands. In the case of C1 domains, the zinc ligands are far apart in primary sequence, with 48 residues separating ligands for the same zinc site. This type of zinc finger fold is referred to as the treble clef motif.

In addition to C1 domains, the treble clef motif is found in proteins such as recombination activating gene product (RAG-1), ribosomal proteins S14 and L24e, FYVE domains, retinoic X receptor, T4 endonuclease VII, cysteine-rich intestinal protein (CRIP), proline-rich tyrosine kinase 2 (Pyk2)-associated protein β, and the MH1 domain of Smad3. These proteins have a wide variety of functions from binding to DNA, protein, or small molecules to enzymatic activities.[54] However, zinc coordination is considered only important to maintain the proper fold, with the functional areas lying outside of the zinc coordination sphere.

A growing body of evidence is revealing that zinc finger metal coordination can serve a direct role in protein regulation. One function of particular interest to the C1 domain is that the coordination sites can act as redox switches for sensing reactive oxygen species in the cell.[55,56] This is of interest because PKC plays a major role in cell signaling triggered by reactive oxygen species that are generated by the mitochondria during metabolism.[57] The data presented in chapter IV characterizes the role of the C1B domain zinc coordination sites in activation of PKC via reactive oxygen species. Further investigation of zinc coordination dynamics of other zinc fingers could reveal a wide spread mechanism of protein regulation.

CHAPTER II

THE DAG SENSITIZING RESIDUE 22 MODULATES BINDING LOOP CONFORMATIONAL EXCHANGE*

Background

The ligand affinity and specificity of C1 domains varies drastically between the various PKC isoforms, in spite of their sequence and structural similarities shown in Figure 3. While several small molecules show promise in binding C1 domains to treat human disorders such as cancers, strokes, Alzheimer's disease, HIV, and cardiovascular disorder (see Chapter I), rational drug development is difficult without understanding the properties that dictate ligand affinity and specificity. Because the different PKC isoforms bring about different, and sometimes even opposing, cell signaling events, it is vital that C1 targeting drugs bind specifically to the intended isoform.[2] Furthermore, these small molecules would also be useful to deconvolute the specific pathways activated by the different isoforms. The work presented in this chapter addresses the effect that a single variable residue has on the DAG and phorbol ester binding affinity and specificity of C1B domains. Through the use of ligand binding studies and NMR, properties of C1B are determined that vary consistently between conventional and novel

*Parts of this chapter are reprinted with permission from Stewart MD, Morgan B, Massi F and Igumenova TI (2011) Probing the determinants of diacylglycerol binding affinity in the C1B domain of protein kinase Cα. Journal of Molecular Biology 408: 949-70. Copyright 2011 Elsevier.

PKC isoforms. This information could be used to aid in the design of selective C1 binding small molecules.

The variable residue of interest is the 22nd residue within the C1 domain, which is highlighted in yellow in Figure 3B. In C1 domains that bind tightly to DAG such as those from C1A domains or novel PKC C1B domains, there is a Trp at position 22. Conversely, there is a conserved Tyr at position 22 in conventional PKC C1B domains, which bind weakly to DAG. Replacement of Trp with Tyr in novel PKCδ C1B or Tyr with Trp in conventional PKCβ C1B reversed the affinities for DAG such that the Trp containing constructs bound with high DAG affinity, regardless of the isoform.[28] In the known structures of both novel and conventional C1B domains, the side-chain of this residue faces away from the ligand binding pocket that lies between the β12 and β34 loops (Figure 3A). Because it does not form the ligand binding surface, the strong dependence on its identity is not easily understood.

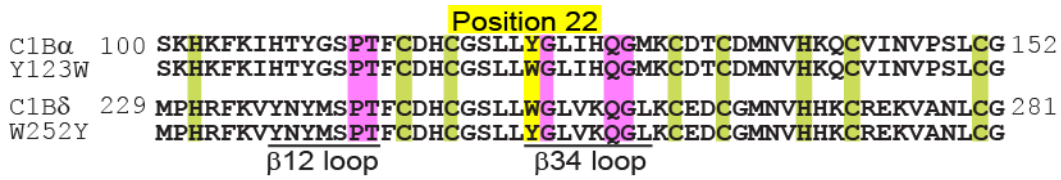

Figure 4. The sequence alignment of the constructs used in this study. The sequences of 53 amino acid constructs of conventional PKCα C1B (C1Bα), novel PKCδ C1B (C1Bδ), and their position 22 mutants (Y123W and W252Y respectively) are shown. Position 22 is highlighted in yellow, zinc coordinating residues in green, and conserved loop residues in pink. Numbering corresponds to the first and last residue of the construct in their respective full length PKC proteins.

To gain insight into the origin of these effects, experiments are performed using the conventional C1B domain from PKCα (C1Bα) and a position 22 Tyr to Trp mutant (residue 123 in the PKCα numbering scheme, Y123W), as shown in Figure 4. Similar to the study described above with C1Bβ, the mutation increases DAG affinity by more than an order of magnitude. Consistent with what is known about the structures of novel and conventional C1 domains, there are no substantial structural differences between C1Bα and Y123W. Dynamics studies show that the mutation does not change the sub-nanosecond dynamics, but there are large differences in conformational exchange in the absence of DAG.

Next, to test the correlation between conformational exchange and DAG affinity the effects of the reverse mutation is tested using the C1B domain from novel PKCδ (C1Bδ) and its position 22 mutant (residue 252 in the PKCδ numbering scheme, W252Y), as shown in Figure 4. The DAG affinity measured with NMR and fluorescence titrations decreased more than 30-fold in the mutant. Similar to C1Bα, the structure and sub-nanosecond dynamics are not affected by the mutation. However, R1ρ relaxation dispersion NMR experiments revealed a significant decrease in conformation exchange in W252Y. Together the data suggest a connection between ligand affinity/specificity and conformational exchange dynamics of the apo C1 domain. Future drug design could take advantage of the different dynamic properties of C1 domains to alter ligand affinity or select for a given C1 domain.

Methods

Protein sample preparation and assignments

53 amino acid constructs of C1B were amplified by PCR using PKC cDNA obtained from Open Biosystems. For C1Bα the sequence was of *Mus musculus* (residues 100-152) and C1Bδ sequence was from *Rattus norvegicus* (residues 229-281). The primary structure in the C1B region does not vary between these two species. The amplified DNA was cloned as a fusion to the small ubiquitin-like modifier (SUMO) into the pET SUMO vector using the provided protocol (Invitrogen). Mutagenesis was performed on the resulting plasmids to make the Y123W mutant from C1Bα and W252Y mutant from C1Bδ using the QuikChange® Site-Directed Mutatgenesis kit from Stratagene and appropriate primers. The purified plasmids were transformed into BL21(DE3) *E. coli* cells for over-expression and purification.

All four proteins (C1Bα, Y123W, C1Bδ, and W252Y) were expressed as SUMO-fusion proteins by induction with 0.5 mM IPTG (isopropyl-D-1-thiogalactopyranoside, purchased from Fisher Scientific) overnight at 15 °C. For natural abundance protein preparations, the cells were induced upon reaching an optical density at 600 nm (OD600) of 0.6 - 0.8. Isotope labeling was accomplished using the method of Marley et al.[58] The method involved re-suspending cells grown on Luria-Bertani broth in M9 minimal medium supplemented with 3 g/L of [^{13}C-6]-D-glucose and 1 g/L of $^{15}NH_4Cl$ (Cambridge Isotopes), and inducing over-expression at OD600 of 1.8-2.0. Fractionally deuterated protein samples were produced using M9 minimal media containing 75% $^{2}H_2O$, 3 g/L of [^{13}C-6]-D-glucose, and 1 g/L of $^{15}NH_4Cl$. The cells were

harvested by centrifugation at 4 °C and lysed at room temperature using a B-PER protein-extraction reagent (Thermo Scientific). The fusion protein was purified using a HisTrap HP Ni affinity column (GE Healthcare Life Sciences). The fractions containing fusion protein were pooled and SUMO was cleaved from C1B with 0.25 mg of SUMO protease at room temperature in the presence of 1 mM 1,4- dithiothreitol (DTT). The vector for his-tagged SUMO protease was provided by Dr. Pingwei Li and SUMO protease was purified by members of our laboratory. Cleavage was >90% complete in ~3 hours for C1Bα constructs and in 12 hours for C1Bδ constructs. Fresh DTT was added half way through C1Bδ construct cleavage due to DTT instability in solution. C1B was separated from SUMO and SUMO protease using gel-filtration on a HiPrep 16/60 Sephacryl S-100 column (GE Healthcare Life Sciences) carried out in 50 mM 2-(N-morpholino)ethanesulfonic acid (MES) buffer and 150 mM KCl at pH 6.5.

All NMR experiments were carried out in NMR Buffer (10 mM [^{2}H-4]imidazole (pH 6.5; Cambridge Isotopes), 150 mM KCl, 8% $^{2}H_2O$, 1 mM tris(2-carboxyethyl)phosphine, and 0.02% NaN_3) at 25ºC on Varian Inova or VNMRS spectrometers operating at 500 (11.7 Tesla) or 600 MHz (14.1 Tesla) unless otherwise stated. The temperature was calibrated using methanol. NMR data were processed with nmrPipe[59] and assigned using SPARKY 3.[60] Backbone resonance assignments for apo C1Bα and C1Bδ were carried out on uniformly ^{15}N,^{13}C enriched 1 mM samples using CBCA(CO)NH and HNCACB three-dimensional NMR experiments.[61] Y123W and W252Y spectra were assigned using C1Bα and C1Bδ assignments.

Ligand binding assays

2-dihexanoyl-sn-glycero-3-[phospho-L-serine] (DPS) and 1,2-dioctanoyl-*sn*-glycerol (DOG) were purchased from Avanti Polar Lipids. [$^{2}H_{38}$]-dodecylphosphocholine (DPC) and [$^{2}H_{6}$]-dimethyl sulfoxide (DMSO) were from Cambridge Isotopes, and phorbol 12,13-dibutyrate (PDBu) was from Sigma-Aldrich. A stock solution of mixed micelles was prepared by combining chloroform solutions of DPS and DPC with a molar ratio of 3:7. Chloroform was removed under a stream of nitrogen gas until only a dry film remains, and then placed under vacuum for two hours. The detergent film was re-suspended in the NMR buffer and vortexed for one minute to form a clear micelle solution. The NMR titration samples contained DPC/DPS micelles with a total detergent concentration of 10 mM and 0.1 mM uniformly ^{15}N-enriched C1 domain. DOG or PDBu dissolved in [$^{2}H_{6}$]-DMSO was added stepwise directly to the NMR sample and ^{1}H-^{15}N heteronuclear single quantum coherence (HSQC) spectra were collected at each concentration. The concentration of DMSO at the titration endpoint was less than 8% (v/v). Three-dimensional assignment experiments were performed on 0.5 mM C1Bδ or 0.4 mM C1Bα saturated with DOG or PDBu respectively in DPC/DPS micelles to verify the assignments.

Titration curves were constructed using the above ligand titrations for all cross-peaks that shift more than 0.05 ppm due to ligand addition by plotting either the change in ^{1}H or ^{15}N (ΔδH or ΔδN respecitively), whichever shift was larger for C1Bα constructs or the overall change in chemical shift (Δ) normalized to ^{1}H for C1Bδ constructs using the following equation [62]:

Equation 1 $\Delta = [\Delta\delta H^2 + (0.152\Delta\delta N)^2]^{1/2}$

versus the absolute ligand concentration (L_0). The curves were then fit with the following single-site binding equation [63]:

Equation 2 $\Delta = (\Delta\delta_{PL} / 2P_0) \times [K_d + P_0 + L_0 - ((K_d + P_0 + L_0)^2 - 4P_0L_0)^{1/2}]$

where $\Delta\delta_{PL}$ is the difference between chemical shifts of the apo and bound states and P_0 is the total protein concentration. Total chemical shift perturbation analysis was calculated as the difference between the apo spectrum and the spectrum at saturation using Equation 1.

DOG titration of C1Bδ and Y123W for fluorescence measurements was carried out in the exact same manner as the NMR titration with the exception of the protein concentration which was 0.5 μM and the buffer used which was 10 mM MES (Fisher Scientific) instead of imidazole. DOG in DMSO was added using a 25μl Hamilton syringe, the cuvette was mixed by tapping, and then set for ten minutes before measurement. After each subsequent addition of DOG the total fluorescence intensity was measured with a 335-nm cutoff filter on an ISS Koala fluorometer (ISS, Champaign, IL) after excitation at 295 nm. The total fluorescence intensity of an identical sample without protein and titrated simultaneously was subtracted to correct for any change due to DOG/DMSO addition that did not arise from protein binding. The fraction of protein bound to DOG was calculated as $\Delta F/F_0$, where ΔF is the absolute value of the intensity change corrected for protein dilution during the titration, and F_0 is the fluorescence intensity before titrating DOG. The average fraction bound from three titrations

corrected for the overall change at DOG saturation versus the total DOG concentration was fit with the following equation:

Equation 3 $$(\Delta F / F_0)_{norm} = (1/2P_0) \times [K_d + P_0 + L_0 - ((K_d + P_0 + L_0)^2 - 4P_0L_0)^{1/2}]$$

where the parameters are the same as those in Equation 2. Using SDS-PAGE combined with silver-staining, it was established that about ~50% of the protein adsorbs on the quartz cuvette walls. This behavior was not alleviated by coating the cuvette with Sigmacote (Sigma-Aldrich). Therefore, the total protein concentration was treated as an adjustable parameter when fitting the binding data.

Sub-ns dynamics

The amide backbone transverse (R_2), longitudinal (R_1), and ^1H-^{15}N heteronuclear Overhauser effect (NOE) relaxation rate constants were obtained for all spectrally resolved high-signal to noise cross-peaks at two fields (14.1 T and 11.7 T) using standard methods.[64] R_2 and R_1 were collected in an interleaved pseudo-3D manner with nine time points from 12-180 ms for R_2 and 30-600 ms for R_1, three of which were duplicates. The NOE data were collected with a 3 s saturation period and 5 s recycle delay. Peak intensities were used to quantify relaxation rates and duplicate points (R_1 and R_2) or root-mean-square noise level of the base planes (NOE) were used to estimate the error of the measurement.

The rotational diffusion properties of C1Bα were evaluated with HYDRONMR[65] and R_2/R_1 ratios,[66] using the ensemble-averaged NMR structure of C1Bα[67] kindly provided by Dr. Ulrich Hommel. HYDRONMR calculations were carried out with atomic element radii *a* of 2.5 Å (minimum) and 2.8 Å (maximum). The *a* values in this

range were shown previously to provide the best agreement with experimental data for proteins with intermediate anisotropy.[68] Estimation of the rotational diffusion tensor based on the R_2/R_1 ratios was done using the program R2R1_diffusion (available from the laboratory of Dr. Arthur G. Palmer, III at Columbia University). Residues that are exchange-broadened and/or have NOE values less than 0.65 were eliminated from the analysis using the criteria outlined in Tjandra et al.[66] and the results of the rotating-frame relaxation dispersion experiments described below.

Relaxation data sets were analyzed using Lipari-Szabo model-free formalism[69] for the case of axially symmetric rotational diffusion, as implemented in the program ModelFree4.20.[70] The formalism relies on the explicit separation of timescales for local and overall rotational motions. The information on the internal motions of ^{15}N-^{1}H vectors is obtained in the form of generalized order parameters, S^2, which report on spatial restriction of motion, and effective correlation times, τ_e, which report on the rate of motion. Five different models having the following parameterization are implemented in ModelFree4.20 to facilitate the relaxation data analysis: (1) S^2; (2) S^2, τ_e; (3) S^2, R_{ex}; (4) S^2, τ_e, R_{ex}; and (5) S^2_f, S^2_s, τ_s. R_{ex} is the contribution of conformational exchange to the R_2; S^2_f and S^2_s are the generalized order parameters for the fast and slow internal motions; and τ_s is the time constant for the slow internal motion.

The Fast-Modelfree program[71] was used to generate the input files and carry out the model selection according to Mandel et al.[70] ModelFree4.20 was used for the simultaneous optimization of the rotational diffusion tensor and motional parameters for the ^{15}N spins assigned to Models 1 and 2. Model selection and rotational diffusion

tensor optimization were iterated until no changes were detected in the model assignment and tensor parameters. The optimized values of the axially symmetric rotational diffusion tensor were τ_m=3.19 ± 0.03 (3.07 ± 0.03) ns, $D_{\|}/D_{\perp}$=1.36 ± 0.08 (1.37 ± 0.08), Ω=92.1 ± 7.1° (94.7 ± 7.6°), and Φ=267.8 ± 9.4° (275.9 ± 9.2°) for C1Bα (Y123W), respectively. Ω and Φ are the Euler angles relating the principle Z axis of the diffusion tensor to the Z axis of the molecular frame of the ensemble-averaged NMR structure of C1Bα. The final calculation was carried out for all spins using the optimized parameters for the rotational diffusion tensor.

Because of the many missing loop residues in intermediate change on the NMR timescale and number of residues with R_{ex} contributions to R_2 in C1Bδ, model-free analysis was not possible for C1Bδ and W252Y sub-ns dynamics comparison. Instead, the R_1 and NOE relaxation rates of C1Bδ and W252Y were used to determine sub-ns dynamics on a per residue basis with the reduced [72,73] spectral density mapping approach [74,75]:

$$J(0.87\omega_H) = \frac{4\gamma_N}{5d^2\gamma_H} R_1(NOE - 1)$$

Equation 4

where $d = (\mu_0 h \gamma_H \gamma_N / 8\pi^2)(1/\langle r_{XH} \rangle^3)$; μ_0 is the permeability of free space; h is Planck's constant; γ_H (γ_N) is the gyromagnetic ratio of ^1H (^{15}N), and r_{XH} is the length of the N-H bond.

Conformational exchange

In order to quantify conformational exchange in all four constructs, off-resonance and near-resonance relaxation dispersion ($R_{1\rho}$) experiments were performed at 11.7 T

and 14.1 T with established pulse sequences. The radio frequency amplitudes (ω_1) were calibrated using the scaling of the $^1J_{NH}$ coupling constant with varying off-resonance decoupling. $R_{1\rho}$ is modulated according to the following relationships by varying ω_1 and the resonance offset (Ω):

Equation 5 $$R_{1\rho} = R_1 \cos^2\theta + R_2 \sin^2\theta$$

Equation 6 $$\theta = \arctan(\omega_1 / \Omega)$$

Equation 7 $$\omega_e = \sqrt{\omega_1^2 + \Omega^2}$$

where θ is the angle between the effective radiofrequency field (ω_e) and the direction of the static magnetic field. R_2 is a sum of the transverse relaxation rate constant in the absence of exchange (R_2^0) and the contribution due to exchange (R_{ex}). For a two-state fast conformational exchange between A $\leftrightarrow$ B, R_{ex} is related to the exchange parameters as follows:

Equation 8 $$R_2 = R_2^0 + R_{ex}$$

Equation 9 $$R_{ex} = \frac{k_{ex}\Phi_{ex}}{k_{ex}^2 + \omega_e^2}$$

in which $\Phi_{ex} = p_A p_B \Delta\omega_N^2$ and $k_{ex} = k_1 + k_{-1}$. k_1 and k_{-1} are the forward and reverse rate constants; p_A and p_B are the populations; and $\Delta\omega_N$ is the residue-specific ^{15}N chemical shift difference for the conformers A and B.

^{15}N magnetization was aligned with ω_e using a $90°_x$-delay-$90°_y$ element for near-resonance experiments and a 6 ms tan/tanh adiabatic ramp starting -15,000 Hz from the carrier frequency for off-resonance experiments. Relaxation delays were a maximum of

160 ms. $\omega_1/2\pi$ varied 560-1270 Hz for near-resonance and 1110-1980 Hz for off-resonance experiments. The carrier offset was varied such that θ ranged from 68-90º for near-resonance and 25-68º for off-resonance experiments.

R_2 was calculated using Equation 5 and plotted against ω_e^2. The curves collected at 11.7 T and 14.1 T were fit to Equation 8 and Equation 9 with Φ_{ex}, k_{ex}, and R_2^0 as adjustable parameters. Because individually fit curves converged with similar k_{ex} values, (C1Bα 1.29–2.25 / Y123W 0.78–1.68 / C1Bδ 0.69-1.03 / W252Y 1.59-2.06) x10^4 s^{-1} all residues with $R_{ex} > 1$ s^{-1} at 11.7 T were fit with a global k_{ex} value. Φ_{ex} was scaled to 14.1 T when globally fitting with data collected at 11.7 T to account for differences in $\Delta\omega_N^2$.

Measurements of ^{15}N-^{1}H residual dipolar couplings (RDCs)

Weakly aligned samples of C1Bα and Y123W were prepared in stretched polyacrylamide gels.[76,77] 6% gels were prepared using the appropriate dilution of 40% acrylamide and bis-acrylamide solution, 37.5:1 (Bio-Rad), 0.1% w/v ammonium persulfate (Fisher Scientific), and 0.08% v/v N,N,N',N'-tetramethylethylenediamine (Fisher Scientific), and cast at a diameter of 6 mm. The gel was soaked overnight with 0.5 mM C1Bα or Y123W and then axially stretched into a 4.2 mm NMR tube using the apparatus obtained from New Era Enterprises.[78] Site-specific residual dipolar couplings, $^1D_{NH}$, were calculated from the in-phase anti-phase (IPAP)[79] spectra as the difference between the splitting of the ^{15}N doublet components in the aligned and isotropic spectra.

Water exchange

The rate of quickly exchanging amide ^{1}H was measured using the CLEAN-EX pulse sequence, [80] in which water magnetization is transferred to exchanging ^{1}H with subsequent detection of excited amide ^{1}H with a fHSQC. The experiment was performed as described with mixing times varying from 4-50 ms using excitation sculpting[81] of the 3-9-19 water gate sequence[82,83] for water suppression on a Bruker 800 Avance system with a cryoprobe. The resulting data were fit to the following equation to obtain the exchange rate with water, H_2O_{ex}:

Equation 10
$$\frac{V}{V_0} = \frac{H_2O_{ex}}{R_{1A} + k_{ex} - R_{1B}} \times e^{-R_{1B,app} \times \tau_m} - e^{-(R_{1A,app} + k)\tau_m}$$

where V is the peak volume at a given mixing time, τ_m; V_0 is the peak volume in a reference fully relaxed fHSQC with a 9s relaxation delay; R_{1A} and R_{1B} are the relaxation rates of the amide ^{1}H and water ^{1}H respectively under the conditions of the CLEAN-EX experiment. R_{1A} was fit as an adjustable parameter. R_{1B} was measured using mixing times up to 200 ms and fit linearly to obtain the water decay rate. After fitting, H_2O_{ex} was corrected for the degree of water saturation as described.[80] Correction of H_2O_{ex} rather than individual points was appropriate as the saturation was found to be 73% and varied less than 1% between the different mixing times and samples.

The rate of slowly exchanging amide ^{1}H was measured by dissolving a dehydrated NMR sample containing protein and NMR buffer with D_2O and rapidly collecting a series of HSQC spectra over time. The rate of decay in the peak intensity for slowly exchanging peaks was fit to an exponential decay using the same methods as

relaxation data fitting described above. The rates were corrected for the initial delay between D_2O addition and beginning data collection.

Determining Trp252 side-chain NOEs

The interactions of the native Trp253 side-chain in C1Bδ were investigated using ^{15}N-edited NOESY, ^{15}N-edited ROESY, and ^{13}C-edited NOESY tuned for aromatic residues. ^{15}N-edited experiments were collected on 0.3 mM uniformly enriched ^{15}N C1Bδ, and ^{13}C-edited NOESY was collected on 2.4 mM uniformly enriched ^{13}C-^{15}N C1Bδ. The ^{13}C-edited NOESY was collected as described in the Varian BioPack User Guide using the supplied pulse sequence with the appropriate flag for aromatic carbons and 100 ms mixing time. The ^{15}N-NOESY experiment was executed using a pulse sequence supplied by Dr. Lewis Kay as described previously with a 140 ms mixing time.[84] The ROESY experiment was implemented in the same manner as TOCSY as described[84] except for a square 5 KHz spinlock pulse was applied during a 60 ms mixing time.

Results of C1Bα and Y123W studies

Y123W mutation increases the affinity of C1Bα to DAG

To determine the lipid cofactor binding affinities of C1Bα and Y123W, diacylglycerol binding assays were carried out in a micellar environment. Because chemical shifts change based upon the local chemical environment, NMR is an excellent method for observing ligand binding. By observing the ^{15}N-^{1}H HSQC spectra of uniformly ^{15}N-enriched C1Bα as a function of increasing concentration of DOG, a short-chain DAG analog, the residues which undergo the largest change in chemical

environment upon binding can be determined. All residues, with the exception of proline, contain an amide group in the protein backbone. The residue identity of the cross-peaks in the spectra can be assigned using three-dimensional NMR experiments as described in the methods, which then provides residue specific information about the ligand binding site.

These titration experiments were carried out in the presence of DPC/DPS mixed micelles with a ratio of 30% phosphatidylserine and 70% phosphatidylcholine head-group components, in order to keep the protein-DOG complex soluble and to mimic the composition of the plasma membrane where the phosphatidylserine content is 25-35% (data shown in Figure 5).[85] For C1Bα, the binding regime is intermediate-to-fast on the chemical-shift time scale, which is reflected in the smooth trajectories of the cross-peaks in response to increasing DOG concentration. This occurs when the sum of the k_{on} and k_{off} (k_{ex}) is significantly greater than the difference in chemical shifts between the apo and bound protein. In Y123W, the binding regime is slow-to-intermediate, which indicates the k_{ex} is significantly less than the difference in chemical shifts of the apo and bound protein. The differences in the DOG titration behavior between C1Bα and Y123W proteins are illustrated in the insets of Figure 5 using Leu122 as an example. Leu122 is located at the N-terminal hinge of loop β34 adjacent to the mutation site and is one of the residues that show a strong response to ligand binding.

For all C1Bα residues that show a strong response to DOG in the HSQC spectra, binding curves were constructed by plotting the absolute change in ^{1}H and/or ^{15}N chemical shifts as a function of DOG concentration. The curves were fit using Equation

2, with $\Delta\delta_{PL}$ and K_d treated as local and global parameters, respectively. Representative ^{1}H and ^{15}N binding curves for several residues are shown in Figure 6A and B. The dissociation constant K_d for DOG in the presence of micelles was determined to be 24.2 ± 2 μM.

In the mutant, the slow-to-intermediate regime of the DOG binding process has precluded the determination of K_d by NMR methods. While there are no Trp residues in the primary structure of C1Bα, the Y123W mutation provides Trp at position 123 for use as a fluorescence probe of protein-DOG interactions. Fluorescence spectroscopy was used to monitor the quenching of Trp fluorescence for Y123W in response to DOG binding in the presence of DPC/DPS micelles. The normalized change of fluorescence intensity as a function of DOG concentration is shown in Figure 6C. Fitting the curve of Figure 6C with Equation 3 revealed that even at the total protein concentration in the low μM range the protein-DOG interaction still remains in the tight binding regime. Further decrease in the total protein concentration was not a viable option due to the high background fluorescence of detergent micelles and the low efficiency of chemical quenching of Trp fluorescence by DOG.[86] Using the data presented in Figure 6C, an upper limit of 0.23 μM can be placed on the K_d.

In addition to DOG-binding studies, NMR titrations of C1Bα and Y123W were carried out with PDBu, a short-chain phorbol ester (Figure 7). In both proteins, the binding regime is slow-to-intermediate, indicating the formation of high-affinity complexes. This result is in complete agreement with previous studies of C1B from

PKCβI/βII, where the affinities of wild-type and mutant proteins to the phorbol ester were similar, and comparable to the affinity of the Y123W mutant to DAG.[28]

A comparison of the titration spectra of Figure 5 and Figure 7 indicates that binding of PDBu and DOG affects the same set of residues in C1Bα. One feature that is common to all three high-affinity complexes (C1Bα-PDBu, Y123W-DOG, and Y123W-PDBu) is the appearance of the Gly110 resonance under conditions close to ligand saturation. Gly110 is located at the tip of loop β12 and is the only residue that is broadened beyond detection in the spectra of apo-forms. Overall, the DOG and PDBu titration data suggest that (i) C1Bα interacts with both ligands using the same structural segments, and (ii) formation of high-affinity protein-ligand complexes is accompanied by the structural rearrangement of the β12 and β34 loops and partial or complete loss of their mobility.

The results of the ligand-binding experiments demonstrate that the Y123W mutation increases the affinity of C1Bα to diacylglycerol at least 100-fold, from 24.2 μM to <0.23 μM. These findings are in good agreement with the data obtained for the C1B domain from PKCβI/βII, where a 33-fold increase in DOG binding affinity was detected, while both constructs bound tight to PDBu using ultracentrifugation lipid-binding assays.[28] The next step was to understand the molecular basis of this drastic change in the DOG-binding affinity. To accomplish this, the effect of the Y123W mutation on both the structure and dynamics of C1Bα was investigated using NMR techniques.

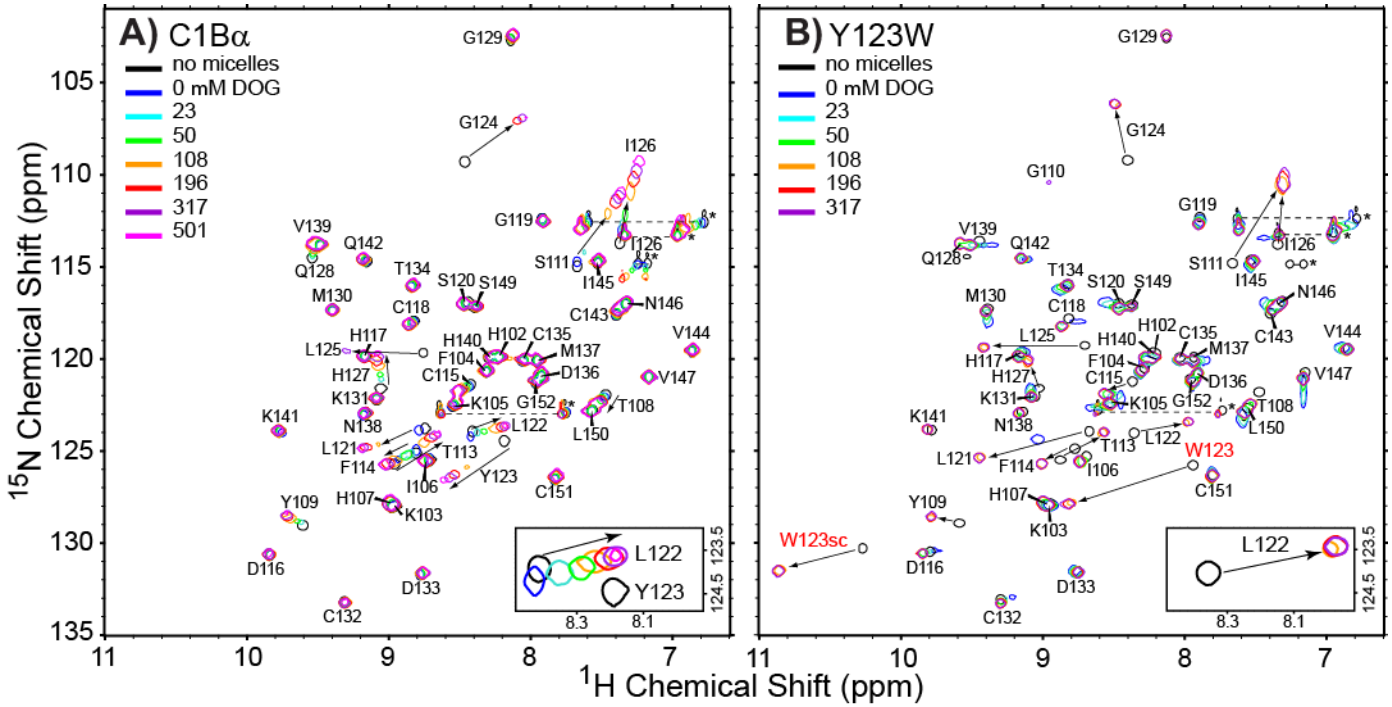

Figure 5. NMR-detected titration of C1Bα (A) and Y123W (B) with DOG in the presence of DPC/DPS micelles. The binding process is intermediate-to-fast and slow-to-intermediate on the chemical-shift timescale for C1Bα and Y123W, respectively. The insets show the differences in the binding regimes for C1Bα and Y123W using Leu122 as an example. Large chemical shift perturbations are observed in the ligand-bound versus apo-spectra.

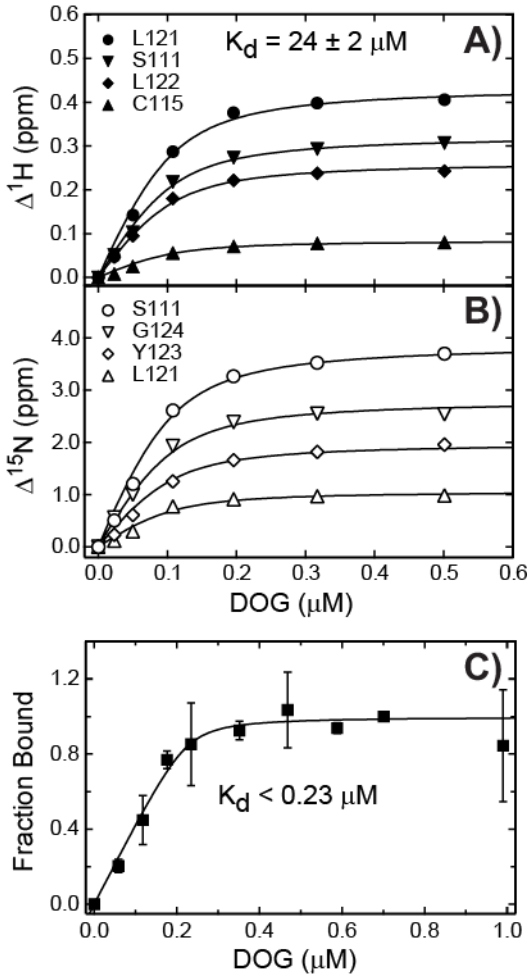

Figure 6. DOG binding curves for C1Bα and Y123W detected by NMR and fluorescence spectroscopy. In (A) and (B), the absolute values of the ^{1}H and ^{15}N chemical shift changes, Δ^{1}H and Δ^{15}N, are plotted as a function of DOG concentration for several representative residues. The binding curves were fit with Equation 2 using the dissociation constant K_d as a global parameter. (C) Normalized change in the fluorescence of Y123W plotted as a function of DOG concentration. The error bars represent the standard deviation between three experiments. Large errors in K_d indicate that, in this protein concentration range, the binding is still tight, and only an upper limit of 0.23 μM can be given to the K_d value. The solid line is provided as a visual aid.

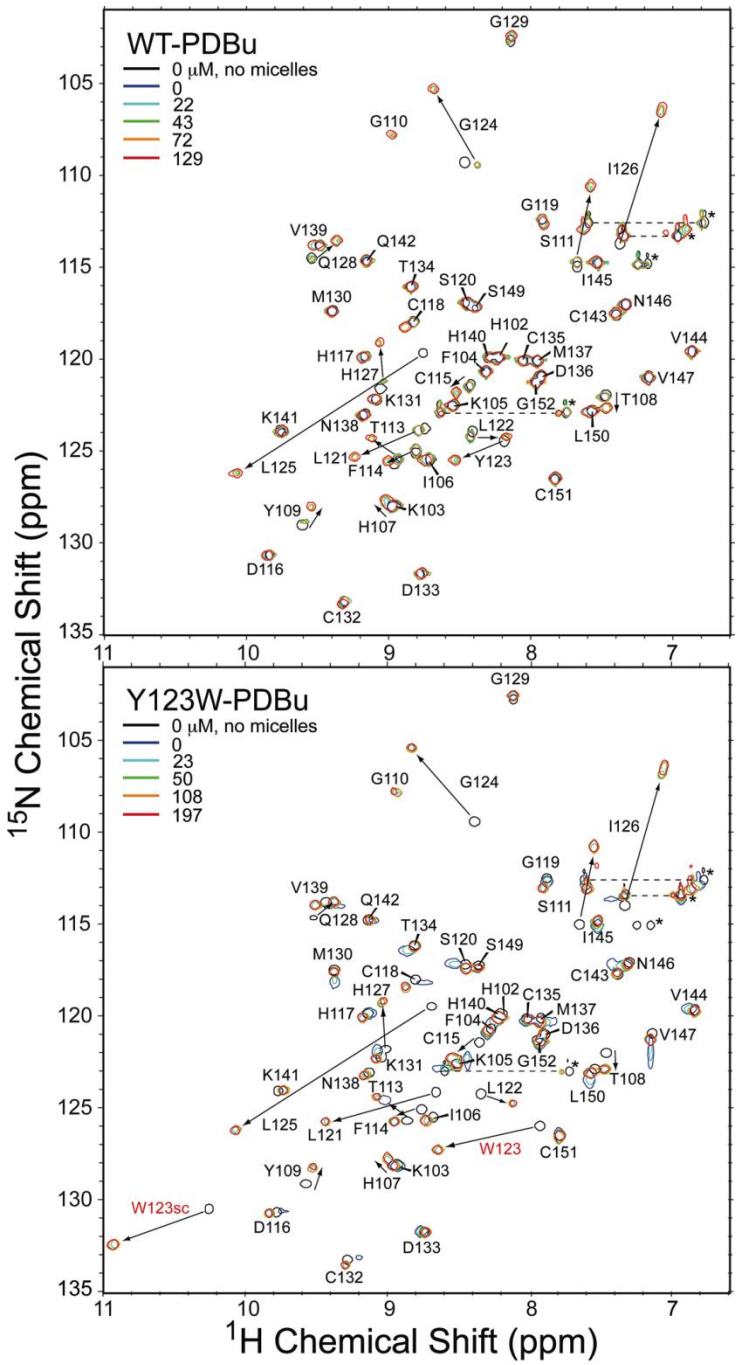

Figure 7. NMR-detected titration of C1Bα (WT) and Y123W with phorbol 12,13-dibutyrate (PDBu) in the presence of 10 mM DPC/DPS micelles. The binding process is slow-to-intermediate on the chemical-shift timescale for both C1Bα and Y123W indicating comparable PDBu affinities. Large chemical shift perturbations are observed in the apo- versus ligand-bound spectra, suggesting that binding of PDBu with concomitant micelle insertion is accompanied by changes in the conformation of the ligand-binding loops.

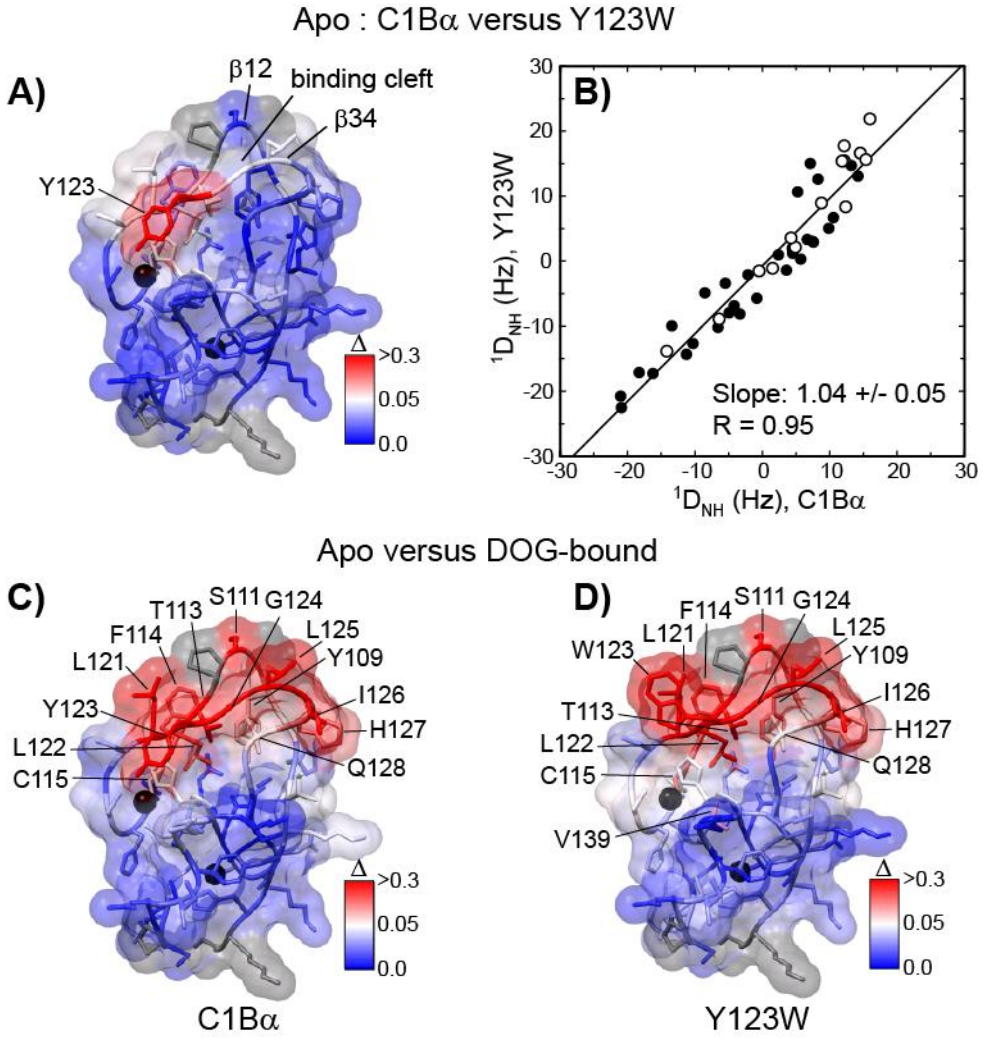

Figure 8. Assessment of structural differences between C1Bα and Y123W using chemical shift perturbation analysis and RDCs. Structural Zn^{2+} ions are shown as black spheres in (A), (C), and (D). Prolines and residues that are missing from the ^{15}N-^1H HSQC spectra are shown in grey. In (A), chemical shift perturbation (Δ) was calculated between the apo-forms of Y123W and C1Bα, and mapped onto the ensemble-averaged NMR structure of C1Bα. (B) Comparison of the $^1D_{NH}$ RDCs between the Y123W and C1Bα. Empty circles correspond to the β12 and β34 loop residues. Fitting the data with a linear function produces a slope of 1.0 within experimental error, suggesting that minimum perturbations are imposed on the backbone of C1Bα by the Y123W mutation. In (C) and (D), Δ was calculated between the DOG-bound and apo forms of C1Bα (C) and Y123W (D). In both proteins, the regions involved in interactions with ligand are the β12 and β34 loops and their hinges. In (D), the Tyr at position 123 was replaced with Trp in the ensemble-averaged NMR structure of C1Bα using WHATIF.[87]

The structures of C1Bα and Y123W are similar in both apo- and ligand-bound forms

The structural perturbation imposed on C1Bα by the Y123W mutation were assessed using chemical shift perturbation analysis (Δ) and RDCs measured for all spectrally resolved ^{15}N-^{1}H groups. The results for the apo-forms of C1Bα and Y123W are shown in Figure 8A and B. In Figure 8A, Δ values are color-coded and mapped onto the NMR structure of C1Bα. Only the site of the mutation experiences a noticeable change in the electronic environment, whereas other parts of the protein, including ligand-binding loops β12 and β34, are essentially unperturbed. RDCs between the ^{15}N and ^{1}H spins of amide groups, $^{1}D_{NH}$, are exquisitely sensitive to the changes of the backbone conformation and have been previously used to evaluate structural perturbations in point mutants.[88,89] $^{1}D_{NH}$ values were measured for the apo-forms of both C1Bα and Y123W weakly aligned in 6% stretched polyacrylamide gels. Figure 8B shows the correlation between the $^{1}D_{NH}$ values in Y123W and C1Bα. Data points corresponding to the loop residues are shown with open circles. Fitting the data with an unconstrained linear function produces an intercept of 0 and a slope of 1 within experimental error. Based on the results of chemical shift perturbation analysis and good correlation between the $^{1}D_{NH}$ values, it can be concluded that the mutation at position 22 does not impose any significant perturbation on the conformation of the C1Bα backbone.

The DOG titration data were used to generate Figure 8C and D, where the chemical shift perturbations Δ were calculated between the DOG-bound and apo-forms

of C1Bα (C**)** and Y123W (D). The regions affected by DOG binding in the presence of DPC/DPS micelles are essentially the same in C1Bα and Y123W and include the following structural elements: the C-terminal half of loop β12 (residues Tyr109 and Ser111); the C-terminal hinge of β12 (Thr113, Phe114, and Cys115); the N-terminal hinge of β34 (Leu121 and Leu122); and the entire loop β34 comprising the stretch of residues from Tyr123 to Gln128, with the only exception of Gly129. Thus, the data suggest that the C1Bα and Y123W interact with micelle-embedded DOG using the same structural segments that include the β12 and β34 loops and their hinges. Given the similarities in the patterns of chemical shift perturbations and site-specific $^{1}D_{NH}$ values, it appears that in both apo- and DOG-bound forms the structure of C1Bα is not substantially affected by the mutation.

Sub-nanosecond dynamics of C1Bα backbone are not affected by the Y123W mutation

Relaxation parameter sets comprising R_1, R_2, and ^{1}H-^{15}N NOE were measured for all spectrally resolved ^{15}N-^{1}H groups in C1Bα and Y123W at two static magnetic fields, 11.7 and 14.1 T. The generalized order parameters, S^2_{NH}, generated by the model-free analysis of the relaxation data were used to assess the effect of the mutation on the sub-ns dynamics of C1Bα backbone. S^2_{NH} values report on the spatial restriction of the motions of ^{15}N-^{1}H vectors, with 1 and 0 corresponding to completely restricted and unrestricted motions, respectively.

Model-free treatment requires an estimate of the rotational diffusion properties of C1Bα. HYDRONMR calculations were carried out on an ensemble-averaged C1Bα

NMR structure with two values of *a*, 2.5 and 2.8 Å, as described in Materials and Methods. For *a* = 2.5 (2.8) Å, the overall rotational correlation time τ_m was calculated as 3.13 (3.40) ns with the following eigenvalues of the diffusion tensor: D_z=6.41 (5.88) x 10^7 s^{-1}, D_y=4.67 (4.33) x 10^7 s^{-1}, and D_x=4.88 (4.51) x 10^7 s^{-1}. Because the difference between D_x and D_y is small (4% for both values of *a*), the diffusion tensor can be treated as axially symmetric with $D_{\|}/D_{\perp}$=1.34 (1.33). The analysis of R_2/R_1 ratios for C1Bα produced τ_m=3.28 ns and $D_{\|}/D_{\perp}$=1.30, which is in good agreement with HYDRONMR results. Since the R_1 and R_2 values are essentially identical between C1Bα and Y123W for all ^{15}N spins not subject to conformational exchange, the conclusion about the axial symmetry of the rotational diffusion tensor holds for Y123W as well. The values of τ_m and $D_{\|}/D_{\perp}$ obtained from the R_2/R_1 analysis were used as an initial input for the first round of model selection.

A comparison of the calculated S^2_{NH} for C1Bα and Y123W, along with the diagram of secondary structure elements and ligand-binding loop regions β12 and β34, is shown in Figure 9A. In C1Bα, the mean S^2_{NH} for the secondary structure elements and β12/β34 loop regions is 0.852 ± 0.031 and 0.813 ± 0.074, respectively. For the Y123W mutant, the values are quite similar to those of the C1Bα, 0.856 ± 0.031 and 0.826 ± 0.069. Thus, the differences in the mobility between the loop regions and the secondary structure elements are subtle. However, in both proteins the two most dynamic non-terminal residues belong to the loop regions. Ser111, with S^2_{NH} of 0.729 ± 0.018 (0.750 ± 0.019) in C1Bα (Y123W), is located in the middle of loop β12. Residue

123, with S^2_{NH} of 0.653 ± 0.020 (0.687 ± 0.024) in the C1Bα (Y123W), is the mutation site located at the N-terminal hinge of the loop β34.

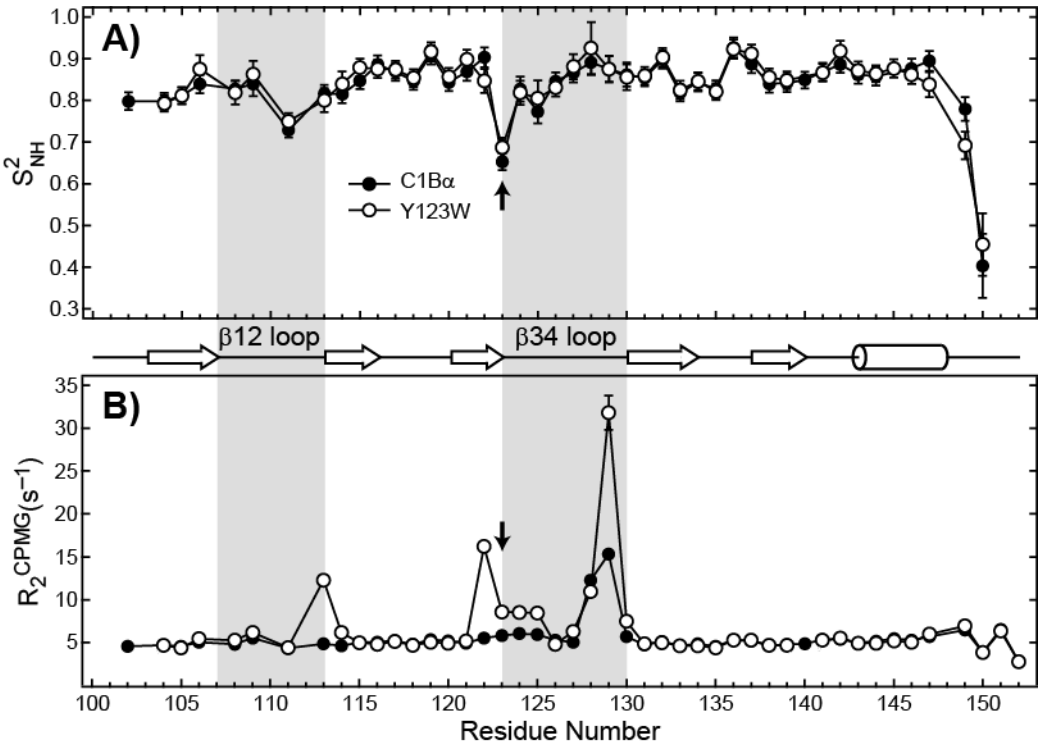

Figure 9. Comparison of the backbone dynamics of C1Bα and Y123W. (A) The generalized order parameters, S^2_{NH}, are plotted as a function of primary structure. Shaded areas correspond to β12 and β34 loops, and the mutation site is indicated with an arrow. It is evident from the plot that sub-nanosecond dynamics of the protein backbone are not perturbed by the Y123W mutation. (B) Comparison of the R_2^{CPMG} values for C1Bα and Y123W. Elevated R_2^{CPMG} values indicate the presence of conformational exchange on the μs-ms timescale. In C1Bα, the most dynamic region is the C-terminal hinge of loop β34, while in Y123W it is both hinges of β34 and the C-terminal hinge of β12.

Another noteworthy feature of the S^2_{NH} profile of Figure 9A is the mobility of the N- and C-termini. In C1Bα, His102, Cys132, Cys135 and Cys151 coordinate one of the

two structural Zn^{2+} ions (Figure 3). His102 is the third and Cys151 is the next-to-last residue of the N- and C-termini, respectively. The S^2_{NH} of His102 is 0.798 ± 0.021 in C1Bα (it is unresolved in Y123W), indicating that the coordination bond with Zn^{2+} restricts the motion of His102. S^2_{NH} values for Cys151 and Gly152 are not available, since neither residue could be adequately fit with any of the five models. However, their R_2 values are substantially reduced compared to the mean values for non-exchanging residues, indicating increased flexibility. Leu150 immediately precedes Cys151 and is highly dynamic with S^2_{NH} of 0.403 ± 0.077 (0.455 ± 0.075) in C1Bα (Y123W). This increase in the flexibility of the Leu150-Gly152 stretch is attributed to the loss of the coordination bond between Cys151 and structural Zn^{2+}. This will be discussed in more detail in Chapter IV.

While the sub-ns dynamics of C1Bα and Y123W are very similar, there are significant differences in their conformational exchange behavior. Conformational exchange refers to the processes that occur on the μs-ms timescale and manifest themselves in the elevated R_2 values for all ^{15}N spins whose magnetic environment changes as a result of the exchange process. R_2 values measured in a Carr-Purcell-Meiboom-Gill (CPMG)-type experiment, R_2^{CPMG}, are shown in Figure 9B. In C1Bα, the most dynamic region is the C-terminal hinge of loop β34, comprising residues Gln128 and Gly129. In Y123W C1Bα, there are two additional regions that are affected by the exchange process, the C-terminal hinge of the β12 loop and the N-terminal region of the β34 loop. The implication of these findings for the model-free analysis of sub-nanosecond dynamics is that the subset of residues fit by Models 3 and 4 in the Y123W

mutant is significantly larger than that in C1Bα (Figure 10). The next step was to determine how the kinetics of the exchange process is altered in the Y123W mutant and evaluate the relevance of these changes to the observed DAG binding affinities.

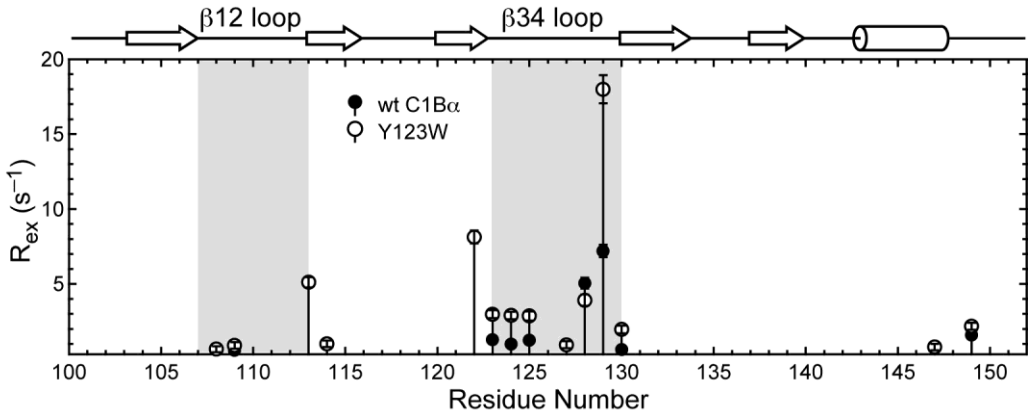

Figure 10. A plot of R_{ex} values obtained from the model-free analysis of C1Bα and Y123W. Eight residues the C1Bα and thirteen residues in Y123W were fit with Models 3 and 4, which explicitly account for the contribution of chemical exchange to the observed relaxation rates. The differences in the conformational dynamics are pronounced for the hinges of the ligand-binding loops (highlighted in gray).

Conformational dynamics of C1Bα are altered by the Y123W mutation

The conformational dynamics of C1Bα backbone was characterized using relaxation dispersion analysis of ^{15}N rotating-frame relaxation rate constant, $R_{1\rho}$. $R_{1\rho}$ experiments are sensitive to the exchange processes that occur on the timescale of microseconds. The relaxation dispersion data for C1Bα and Y123W were fit with a two-state model for the exchange process that is fast on the chemical-shift timescale. The parameters of the model describe the exchange between two conformers A and B, A⇔B, in terms of the exchange rates k_{ex} and a composite parameter Φ_{ex} (Equation 9).

The latter contains information on the structural differences between the conformers ($\Delta\omega_N^2$) and the thermodynamics of the process ($p_A p_B$). The conformers A and B will be referred to as the ground and excited states, respectively.

Table 1 summarizes the results of the global fit for all exchange-broadened residues whose $R_{ex} > 0.5\ s^{-1}$ at 11.7 Tesla. k_{ex} decreased significantly, from 15,400 to 9,600 s^{-1}, in the Y123W mutant. The "Group" column in Table 1 indicates the location of the residues in relation to the ligand-binding loops. β12N, β12C, β34N, and β34C refer to the N- and C-terminal hinges of the β12 and β34 loops. It is evident from Table 1 that all residues for which quantifiable dispersion was detected are located in the hinge regions of β12 and β34. In addition, four residues in Y123W (Gly111, Leu125, His127, and Gln128) and two in C1Bα (Gly111 and Leu125) are broadened by the exchange process, but the low intensity of their cross-peaks precluded the measurement of relaxation dispersion curves.

Table 1. Summary of the conformational exchange parameters in C1Bα and Y123W.

Residue	R_2^0 (s^{-1}), 14.1 T	R_2^0 (s^{-1}), 11.7 T	$\Phi_{ex} \times 10^3$ (s^{-2})[a]	k_{ex} (s^{-1})	Group[b]
C1Bα					
Tyr109	4.87 ± 0.12	4.65 ± 0.11	21.6 ± 3.0	15400 ± 400	β12N
Tyr123	4.17 ± 0.07	4.00 ± 0.05	31.5 ± 1.7		β34N
Gln128	5.52 ± 0.17	5.06 ± 0.13	115.9 ± 5.0		β34C
Gly129	5.48 ± 0.22	5.10 ± 0.15	164.8 ± 7.0		β34C
Met130	4.80 ± 0.06	4.79 ± 0.04	13.8 ± 1.1		β34C
Other dynamic residues: G111 (β12) and Leu125 (β34)					
Y123W					
Ile106	4.84 ± 0.05	4.59 ± 0.04	10.5 ± 0.8	9600 ± 200	β12N
Thr108	4.74 ± 0.07	4.60 ± 0.07	8.2 ± 1.3		β12N
Thr113	4.52 ± 0.21	4.27 ± 0.19	99.1 ± 4.5		β12C
Phe114	4.84 ± 0.06	4.63 ± 0.05	17.8 ± 1.1		β12C
Leu122	5.26 ± 0.17	4.91 ± 0.14	138.5 ± 4.0		β34N
Trp123	4.18 ± 0.08	3.70 ± 0.07	58.3 ± 1.8		β34N
Gly124	5.58 ± 0.10	5.16 ± 0.08	37.5 ± 1.9		β34N
Gly129	6.10 ± 0.41	5.48 ± 0.25	284.0 ± 8.1		β34C
Met130	4.82 ± 0.06	4.74 ± 0.06	29.6 ± 1.3		β34C
Other dynamic residues: Gly111 (β12), Leu125 (β34), His127 (β34), and Gln128 (β34C)					

[a] Φ_{ex} is given for 14.1 T.

[b] β12N, β12C, β34N, and β34C refer to the N- and C-terminal hinges of the β12 and β34 loops.

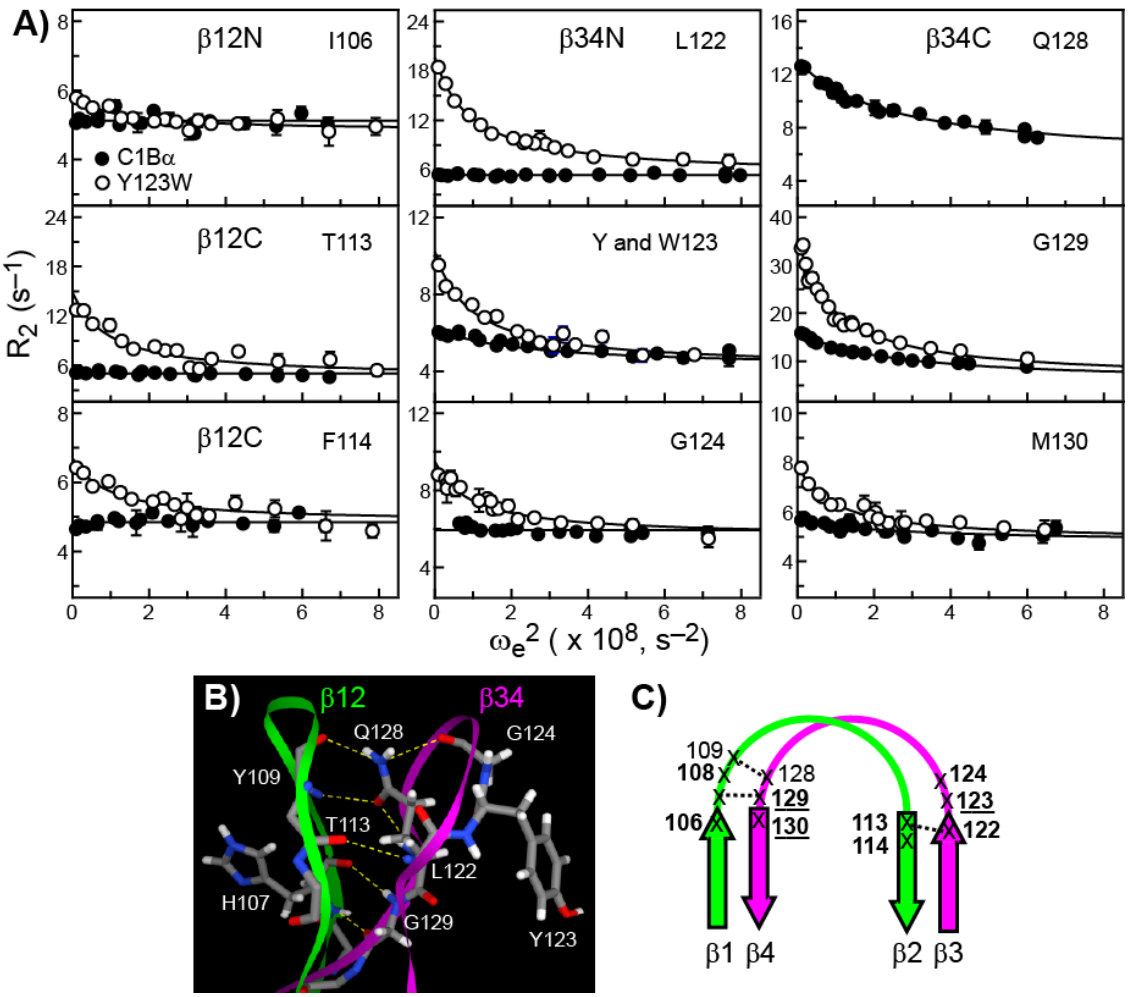

Figure 11. Comparison of conformational dynamics in C1Bα and Y123W. (A) Comparison of relaxation dispersion curves for individual residues in C1Bα (solid circles) and Y123W (open circles). For clarity, only the 14.1 T data are shown. The solid lines correspond to the global fits with parameters summarized in Table 1. Residue groups are defined in Table 1. (B) Intra- and inter-loop hydrogen bonds that stabilize β12 and β34. Because the loop region in the NMR ensemble of C1Bα is poorly defined, a homology model of C1Bα that is based on the structure of C1Bδ (1PTQ) is presented. Five residues that show quantifiable dispersion amplitudes in either C1Bα or mutant, Thr113, Leu122, Gly124, Gln128, and Gly129, are involved in those hydrogen bonds. (C) Conformational dynamics of loop hinges in β12 and β34. Residues that have quantifiable dispersion in both C1Bα and Y123W are underlined. Residues with quantifiable dispersion in either C1Bα or Y123W are shown with regular and bold fonts, respectively.

Residue-specific relaxation dispersion curves showing the dependence of R_2 values on the spin-lock amplitude are presented in Figure 11A. The residues of β12N show very small dispersion amplitudes in both proteins. The β12C hinge comprising residues Thr113 and Phe114 does not undergo conformational exchange in C1Bα. In contrast, these two residues show significant dispersion in the mutant (Figure 11A, first column). The same pattern is observed for the β34N, which includes Leu122, the mutation site Tyr/Trp123, and Gly124 (Figure 11A, second column). While Tyr123 shows small but non-negligible dispersion in C1Bα, the profiles are flat for Leu122 and Gly124. In the Y123W mutant, the dispersion for all three residues of the β34N hinge is prominent. The β34C region comprising Gln128, Gly129, and Met130 is dynamic in both proteins, but the dispersion amplitude in the mutant is substantially increased for Gly129 and Met130 compared to C1Bα (Figure 11A, third column). To summarize, the Y123W mutation leads to a significant increase in conformational flexibility of C1Bα on the μs timescale, especially in the β12C and β34N regions.

Figure 11B highlights several residues that are involved in the formation of hydrogen bonds that stabilize both intra- and inter-loop structure. Because the loops are poorly defined in the NMR ensemble of C1Bα, a homology model generated using the crystal structure of C1Bδ is presented.[22] This hydrogen-bonding pattern is also shared by C1Bγ[90,91] which has a 75.5% sequence identity with C1Bα. The C=O group of Gln128 side-chain serves as a hydrogen bond acceptor for its own backbone N-H group and the N-H of Tyr109. In addition, the NH_2 group of the Gln128 side-chain is a

hydrogen-bond donor to Gly124, located on the same loop β34, and Tyr109 located on loop β12. The N-H of Gly129, which shows the largest dispersion amplitude in both C1Bα and Y123W, is involved in the hydrogen-bonding interaction with the C=O of H107. Finally, Leu122 N-H and Thr113 C=O form a donor-acceptor pair that stabilizes the inter-loop structure. These hydrogen bonds are essential to maintaining the integrity of the anti-parallel β-sheets formed by strands β1/β4 and β2/β3, as shown in Figure 11C.

Three residues that have measurable dispersion in both C1Bα and Y123W are Tyr/Trp123, Gly129, and Met130. The cross-peak positions of Met130 and Gly129 are essentially coincident in C1Bα and Y123W HSQC spectra, yet their Φ_{ex} values are drastically different. The implications are that (i) in both proteins, the population of the excited state is fairly small and the major contribution to the observed population-averaged chemical shift comes from the ground state; and (ii) the conformational equilibrium between the ground and excited states in the Y123W mutant is altered compared to that in C1Bα. The k_{ex} value in the mutant is 9,600 s^{-1} compared to 15,400 s^{-1} in C1Bα. This means that either k_1 or k_{-1} or both decrease as a result of the mutation. A simultaneous increase of the activation energies in forward ($E_{a,1}$) and reverse ($E_{a,-1}$) directions is unlikely because that would imply a substantial increase in the energy of the transition state due to the mutation. Because the excited state populations are small, $k_1 << k_{-1}$ and $E_{a,1} >> E_{a,-1}$ for both proteins. The change in the energy of the excited state brought about by the mutation would contribute significantly to $E_{a,-1}$ and negligibly to $E_{a,1}$. Then, $k_1^{C1B\alpha} \approx k_1^{Y123W}$ and the ratio of the fractional populations of the excited states in the mutant and C1Bα can be estimated as: $p_B^{Y123W}/p_B^{C1B\alpha} = k_{ex}^{C1B\alpha}/k_{ex}^{Y123W} =$

1.60. In addition, the plot of Φ_{ex} values in the mutant versus C1Bα for Tyr/Trp123, Gly129, and Met130 shows a linear correlation with a slope of 1.73 (Figure 12). If it is assumed that $\Delta\omega_N$ is similar for these three residues in C1Bα and Y123W, then the linear correlation implies a 1.73-fold population shift in the mutant. This means the mutation alters the conformational exchange equilibrium, thereby increasing the population of the excited state by 60-70%.

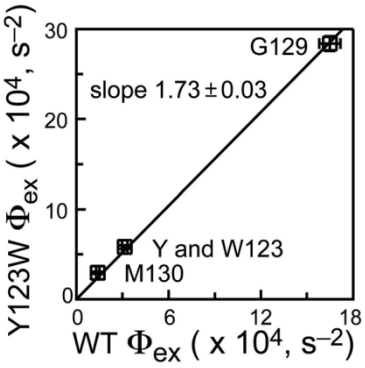

Figure 12. Φ_{ex} values in Y123W compared to C1Bα. A plot of Φ_{ex} values of Y123W versus C1Bα (WT) for three residues that show quantifiable dispersion in both proteins. The slope of the fitted line is 1.73 ± 0.03.

In addition to the population shift, some structural features of the excited state in the Y123W mutant are likely to be different from those of the C1Bα. This conclusion is based on the observation that residues Thr113, Phe114, Leu122, Trp123, and Gly124 have substantial dispersion amplitudes in Y123W but show either very little (Tyr123) or no (all others) dispersion in C1Bα. These regions correspond to the C- and N-terminal hinges of β12 and β34 loops that stabilize the structure of the β2/β3 anti-parallel beta-sheet, as shown in Figure 11C.

Based on the identity of the residues affected by the conformational exchange and their position in the three-dimensional structure of C1Bα, the process that is detected in the relaxation dispersion experiments may involve transient breaking and formation of hydrogen bonds between the anti-parallel β1/β4 strands in C1Bα, and both β1/β4 and β2/β3 strands in the Y123W mutant (Figure 11C**)**. This process may also be accompanied by the opening and closing of ligand-binding loops.

Results of C1Bδ and W252Y studies

W252Y mutation decreases C1Bδ affinity for DOG

To assess the effect of the W252Y mutation on ligand binding, DOG was added stepwise to C1Bδ or W252Y in the presence of DPC/DPS mixed micelles and observed by a decrease in tryptophan fluorescence or with HSQC spectra (Figure 13). When observed with NMR HSQC spectra, C1Bδ exhibited slow-exchange behavior; cross-peaks corresponding to the bound conformation were present at DOG concentrations below the C1Bδ concentration (Figure 13A). The decrease in tryptophan fluorescence was used to estimate the binding affinity. The K_d value from the fit of the fluorescence data is lower than the detectable protein concentration, so only an upper limit can be placed on the K_d of less than 0.2 μM. However, W252Y exhibited fast-exchange behavior similar to the DOG titration of C1Bα (Figure 13B and Figure 5A). By plotting the change in chemical shift that occurs for a given DOG concentration and globally fitting all affected residues to Equation 2, the K_d of W252Y for DOG in mixed micelles was determined to be 5.5 ± 0.4 μM. The fitting results of four representative residues

are shown in Figure 13D. From these data, it is concluded the W252Y mutation decreases the DOG affinity more than 28-fold. Together with the C1Bβ / Y123W reported by Newton's group[28] and the C1Bα / Y123W reported in the previous section, there is good evidence that Trp at position 22 increases DOG affinity well over an order of magnitude regardless of the PKC isoform.

Changes in ^{15}N or ^{1}H chemical shift reflect a change in the electronic environment of the corresponding residue backbone. Figure 14 shows the changes in chemical shift between apo and DOG-bound in DPC/DPS micelles plotted for all quantifiable residues and mapped onto the crystal structure and W252Y homology model. C1Bδ and W252Y residues located on the α-helix and both ligand binding loops show a large change in chemical shift due to DOG binding. The chemical shift perturbation is not quantifiable for many loop residues due to exchange broadening in the absence of ligand (denoted with purple asterisks or colored purple in Figure 14). Once both constructs are saturated with DOG, the exchange broadening in the loops is quenched. The residues that are quantifiable for both constructs have similar chemical shift perturbations due to DOG binding, revealing a similar chemical environment for residues in the DOG-bound structure regardless of the W252Y mutation.

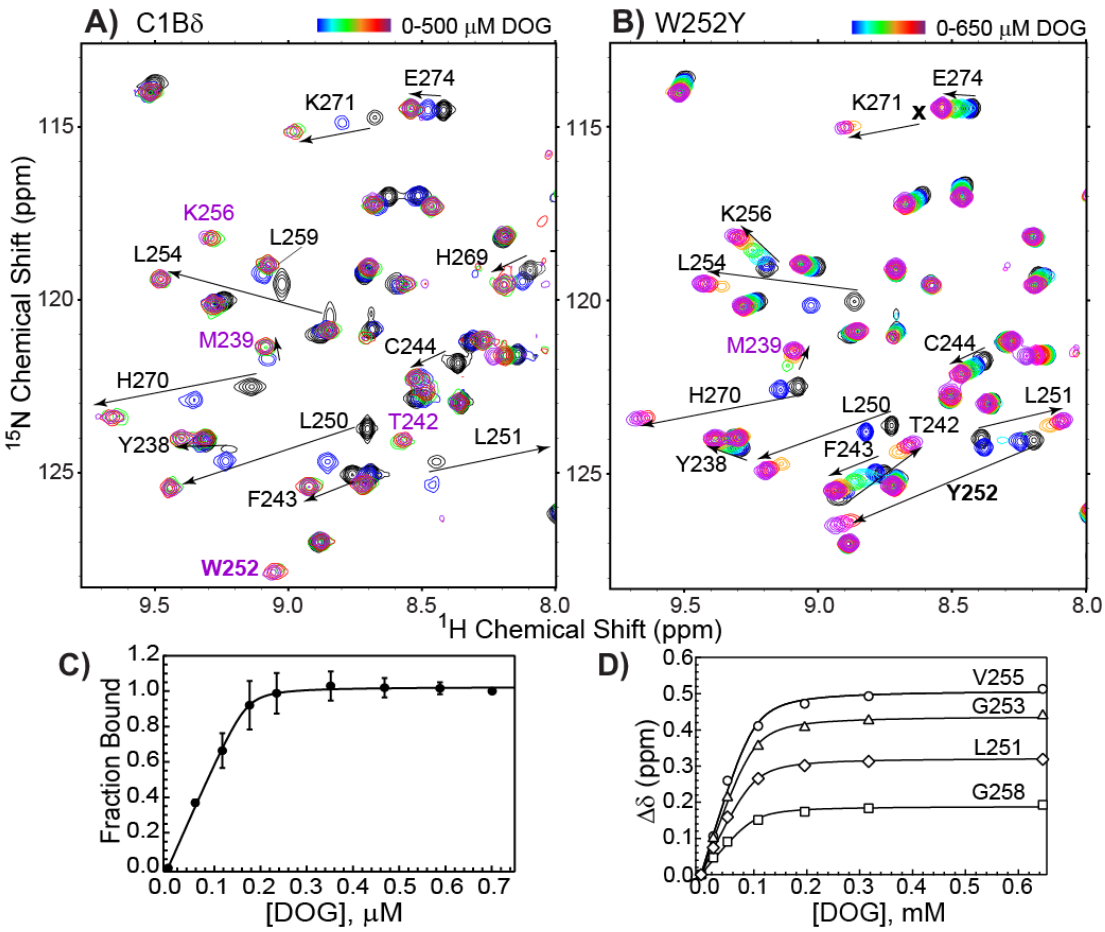

Figure 13. C1Bδ and W252Y binding to DOG in the presence of mixed micelles. An overlay of HSQC spectra excerpts collected on uniformly ^{15}N enriched C1Bδ (A) or W252Y (B) in apo-state (black), or increasing concentration of DOG in the presence of 10 mM DPC/DPS micelles (blue to red rainbow colored). Labels of residues exchange-broadened in the apo spectrum are purple. Due to the fast exchange regime of C1Bδ shown in (A), the affinity of C1Bδ for DOG was estimated using the decrease in fluorescence as shown in (C) and described in the methods. Each point is an average of three trials normalized to fluorescence decrease at the highest DOG concentration. The curve is a fit to Equation 3 which produced values of P_0 = 0.17 ± 0.01 μM and K_d = 2.6 ± 1.1 nM. Because of the tight binding regime, only an upper limit is put on the K_d of 0.2 μM. (D) The change in chemical shift due to binding DOG is plotted in for representative residues in W252Y. The curves represent a global fit of all significantly shifting residues to Equation 2 to yield a K_d of 5.5 ± 0.4 μM.

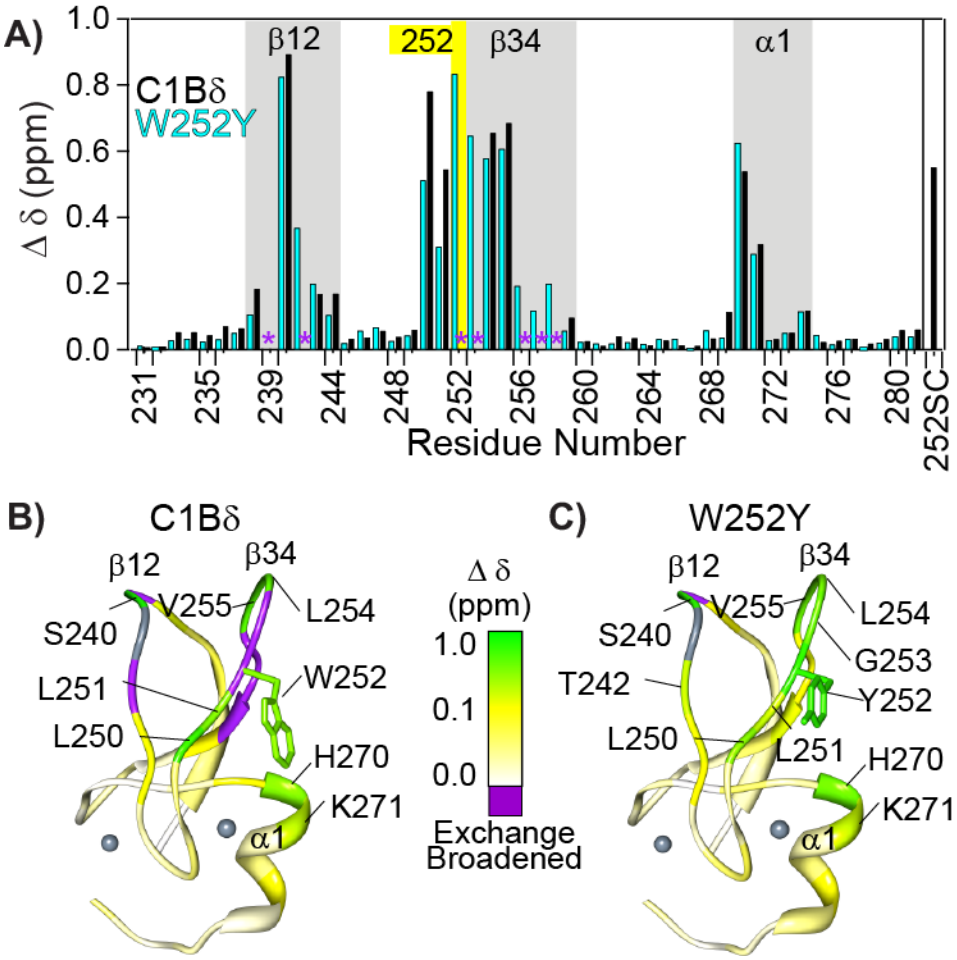

Figure 14. The change in chemical shift between apo and DOG saturated C1Bδ varients. Chemical shift change determined by Equation 1 is plotted versus the primary structure in (A) and onto the C1Bδ apo crystal structure for C1Bδ (B) and homology model for W252Y (C). Significantly shifting residues are labeled in (B) and (C). Residues which are exchange-broadened in apo are denoted with a purple asterisk (A) or colored purple (B and C). Proline is colored gray in (B) and (C).

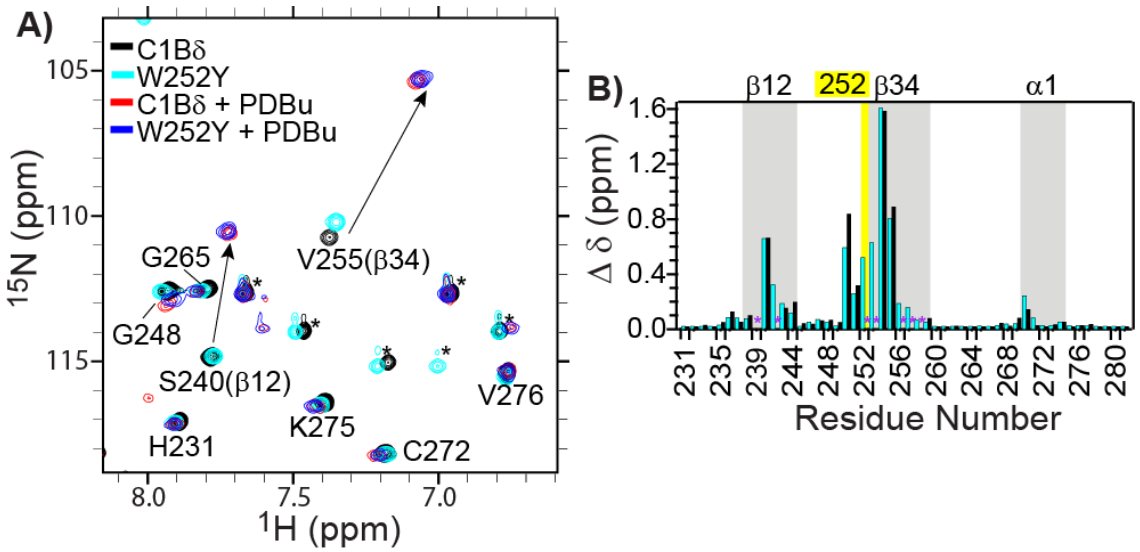

Figure 15. Phorbol ester binding properties of C1Bδ and W252Y. (A) An overlay of HSQC spectra of C1Bδ and W252Y in apo-state (black and cyan respectively) and in the presence of two fold PDBu with respect to protein concentration and mixed DPC/DPS micelles (red and blue respectively). Side-chain cross-peaks are denoted with "*". (B) The change in backbone chemical shift due to binding PDBu (two fold protein concentration) in the presence of mixed micelles, as determined with Equation 1. The ligand binding loops, α-helix, and mutation site are highlighted with gray and yellow respectively. The residues exchange-broadened in the apo spectrum are denoted with a purple asterisk.

In a similar experiment, PDBu was added stepwise to C1Bδ and W252Y in mixed micelles. An overlay of HSQC spectra is shown in Figure 15A. Both constructs bind PDBu in the slow NMR timescale regime, reminiscent of the tight C1Bδ DOG binding. This is consistent with the Newton Laboratory's previous results showing that even though mutation of Trp252 in C1Bδ to Tyr caused a 10-fold decrease in membrane localization in response to DAG, it retained similar membrane localization in response to PDBu.[28] In addition, the same residues respond to PDBu binding and to the same degree in both C1Bδ and W252Y. Comparison of the change in chemical shifts due to DAG

binding to the change caused by PDBu binding (Figure 13 and Figure 15B) reveals the same loop residues respond to the binding of both ligands. These residues are also similar to the conventional C1Bα residues which respond to DOG and PDBu binding (Figure 8 and Figure 7). Both phorbol esters and DAG bind in the β12-β34 loop pocket as previously hypothesized from the crystal structure of C1Bδ bound to water soluble phorbol ester.[22]

W252Y mutation has a minor affect on the chemical shifts of C1Bδ

To access the effect of the mutation on the structure of C1Bδ, chemical shifts were compared to those of W252Y in Figure 16 for apo and DOG saturated states. The data are not available for seven of the loop residues in the apo comparison due to exchange broadening in one or both of the constructs (purple asterisks in Figure 16). An overlay of C1Bδ and W252Y spectra in each state is shown for a β12 residue (Ser240) and a β34 residue (Val255). In the apo state, small differences in chemical shifts are observed for residues close in space to the mutation site (Figure 16A). Cross-peaks from all of the non-proline residues are present in the DOG-bound spectra; from this it is clear that the only significant chemical shift differences due to the mutation are at or directly adjacent to the mutation site (Figure 16B). This is an indication that similar to C1Bα, the dominant structure of C1Bδ in solution does not change dramatically due to the identity of residue 22.

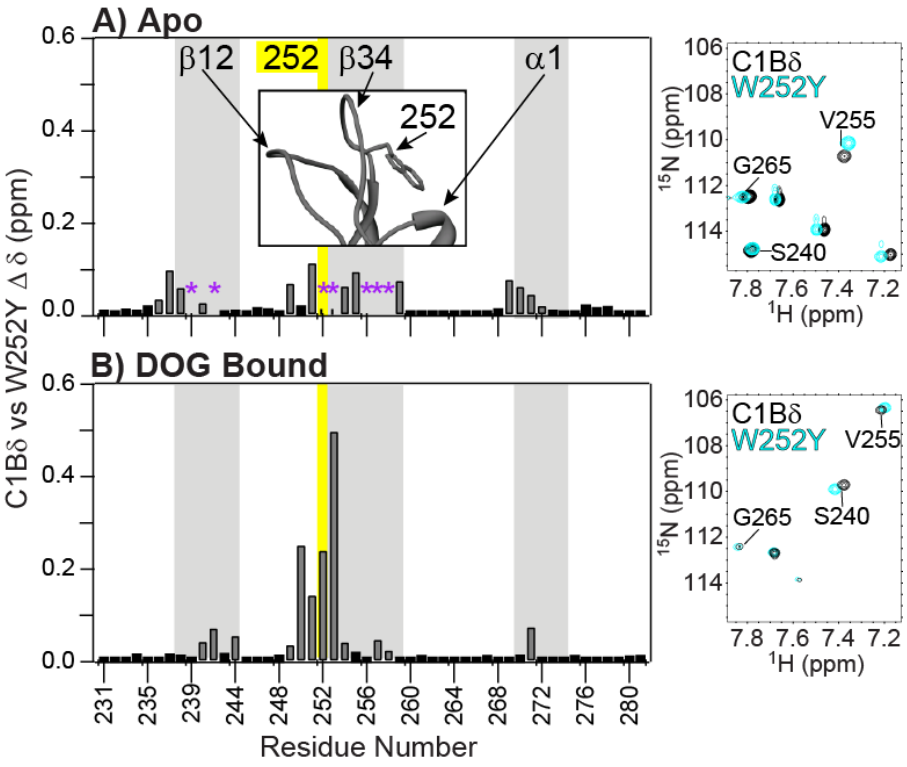

Figure 16. The overall change in chemical shifts due to the W252Y mutation when apo (A) or DOG saturated (B). The residues surrounding the mutation site are significantly shifted and other residues near the mutation in tertiary structure in the β12 and α-helix are also affected. An excerpt of the C1Bδ and W252Y HSQC spectra in each state is shown for a β12 loop residue (Ser240) and β34 loop residue (Val255), showing that while the change in chemical shift due to binding is large, the change due to the mutation is small in comparison.

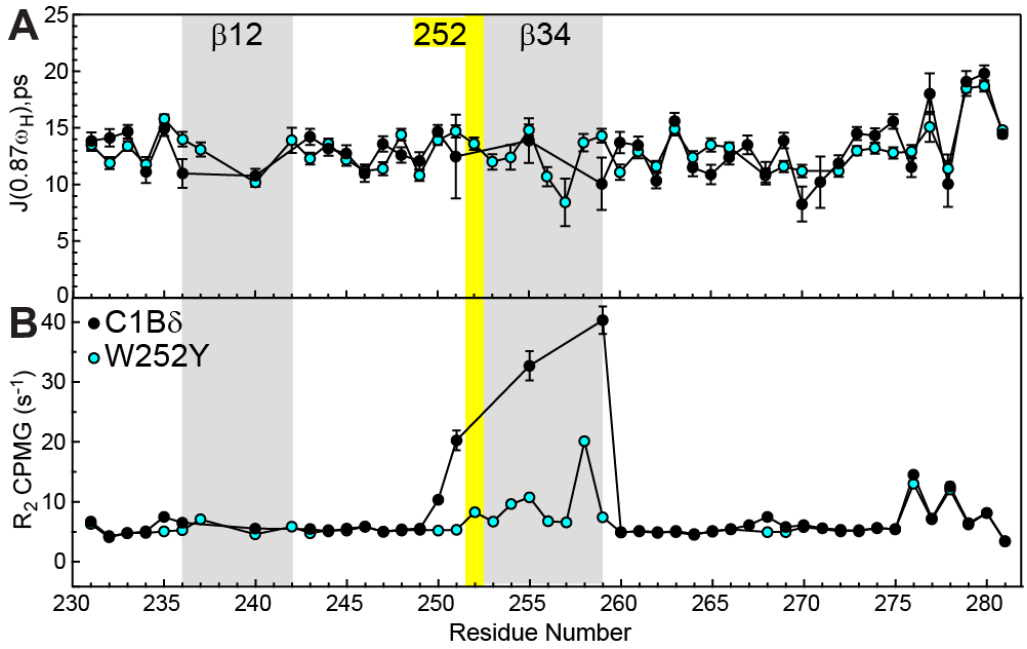

Figure 17. Effect of W252Y mutation on backbone dynamics. (A) $J(0.87\omega_H)$ calculated using R_1 and NOE collected at 14.1 T and (B) R_2 values measured with CPMG at 14.1 T are plotted for all high signal-to-noise and resolved residues in C1Bδ (black) and W252Y (cyan). Black lines connect residues with available data.

The W252Y mutation alters conformational exchange, without affecting sub-nanosecond dynamics

The reduced spectral density mapping approach was used to determine $J(0.87\omega_H)$ from R_1 and NOE collected at 14.1 T for all spectrally resolved backbone cross-peaks in C1Bδ and W252Y. $J(0.87\omega_H)$ is an average of 13 ± 2 ps for C1Bδ and W252Y constructs. Figure 17A shows the $J(0.87\omega_H)$ obtained for both constructs. The only residues more than two standard deviations from the average are Leu279 and Cys281. They exhibit elevated dynamics in both constructs, likely due to zinc coordination dynamics of Cys281 as discussed in Chapter IV. There are no significant changes in sub-nanosecond timescale dynamics due to the mutation.

As mentioned above in the context of C1Bα results, R_2 is reflective of both sub-nanosecond timescale dynamics as well as conformational exchange on the μs-ms timescale (Equation 8). If the backbone of a residue experiences a different electronic environment in two exchanging conformations, the R_2 as determined using CPMG experiments will be elevated as is seen for both C1Bδ and W252Y. The most dynamic region in both constructs is the β34 loop. Many of the C1Bδ β34 loop cross-peaks are exchanged broadened to the extent that R_2 cannot be accurately measured; however, all those that are measureable are significantly more elevated in C1Bδ than in the mutant (Figure 17B). Several residues in the C-terminal region also show elevated R_2, but the elevation is the same for both C1Bδ and W252Y. These residues show little to no dispersion in the following analysis, thus likely represent a dynamic process independent of loop motion and on a different timescale, such as zinc coordination dynamics (more in Chapter IV).

$R_{1\rho}$ experiments were performed on C1Bδ and W252Y, in a similar manner as C1Bα and Y123W, to quantify and better understand the nature of the conformational exchange process. For both C1Bδ and W252Y C1Bδ, five residues produced cross-peaks which were well resolved, high signal-to-noise, and had a R_{ex} greater than 1 s^{-1} at 11.7 T. The data collected at 14.1 T and fit to Equation 8 and Equation 9 are shown in Figure 18A with the location of the residues in the structure highlighted in red in Figure 18B. Three of these residues (left column) are dispersive in C1Bδ, but show no dispersion in W252Y. Two residues are dispersing in both constructs (middle column),

but the R_{ex} is much larger for C1Bδ. The three residues which show the largest quantifiable dispersion in W252Y (right column) are too broadened by the exchange process to quantify in C1Bδ. The severely broadened residues, which are intermediate on the NMR chemical shift timescale (11 total in C1Bδ and 2 total in W252Y), are colored in purple in Figure 18B. Asn267 and Tyr238 were not quantifiable in W252Y due to overlap of the cross-peaks in the HSQC spectra. These residues are colored white in Figure 18B along with proline. Two residues in C1Bδ and four in W252Y also showed some contribution of R_{ex} to R_2 (gold in Figure 18B), but were left out of global analysis because R_{ex} was less than 1 s^{-1}. While all of these residues are located on or near the hinge of the ligand binding loops, the difference in identity and quantity of exchanging residues likely points to a difference in the structure of the higher energy conformation sampled by the two constructs, as was seen for C1Bα and Y123W.

The five quantifiable residues in each construct were fit globally for data collected at 11.7 and 14.1 T to determine a k_{ex} for the exchange process. A summary of the fitting parameters is given in Table 2. The conformational exchange occurs faster for the W252Y mutant (k_{ex} 18,300 ± 900 s^{-1}) than for C1Bδ (k_{ex} 8,100 ± 200 s^{-1}). The two residues with quantifiable dispersion in both constructs have a significantly larger Φ_{ex} in C1Bδ compared to W252Y as shown in Table 2 for Val255 and Leu259. Val255 decreases almost 3-fold in the mutant, while Leu259 decreases more than an order of magnitude. Because Φ_{ex} does not systematically vary for the two residues as was seen for C1Bα / Y123W in Figure 12, the change cannot be due solely to a change in

thermodynamics. This means that there is a larger difference in chemical shifts between the ground and excited states for at least one of these residues in the C1Bδ construct compared to W252Y and the populations may or may not be shifted more toward the excited state in C1Bδ. Because the chemical shifts in the HSQC represent a population weighted average of the ground and excited states and C1Bδ has similar chemical shifts as W252Y, the population of the excited state is small for both constructs. The residue specific Φ_{ex} does not correlate with the change in ^{15}N chemical shift of the given residue due to binding DOG, or PDBu. For instance, the residue with the largest Φ_{ex} in each construct (Gly258 in W252Y and Leu259 in C1Bδ) show relatively small shifts due to ligand binding. To gain insight into the structural changes between the ground and excited states these residues are examined in the crystal structure of C1Bδ.

The dotted lines in Figure 18B depict the hydrogen bonds that form between the β12 and β34 ligand binding loops (1PTQ) as discussed in the C1Bα results section. All of the residues forming these hydrogen bonds in C1Bδ respond to the process that is causing conformational exchange. In contrast, only Gly258 shows quantifiable dispersion in W252Y, while Thr242, Gly253, and Gln257 show a weak response to this process. In summary, C1Bδ is undergoing a conformational exchange process that may be linked to breaking and formation of hydrogen bonds that bridge the ligand binding loops. When W252 is mutated to Tyr, the conformational exchange becomes faster, the excited state that is sampled is closer in structure to the ground state, and fewer residues are affected.

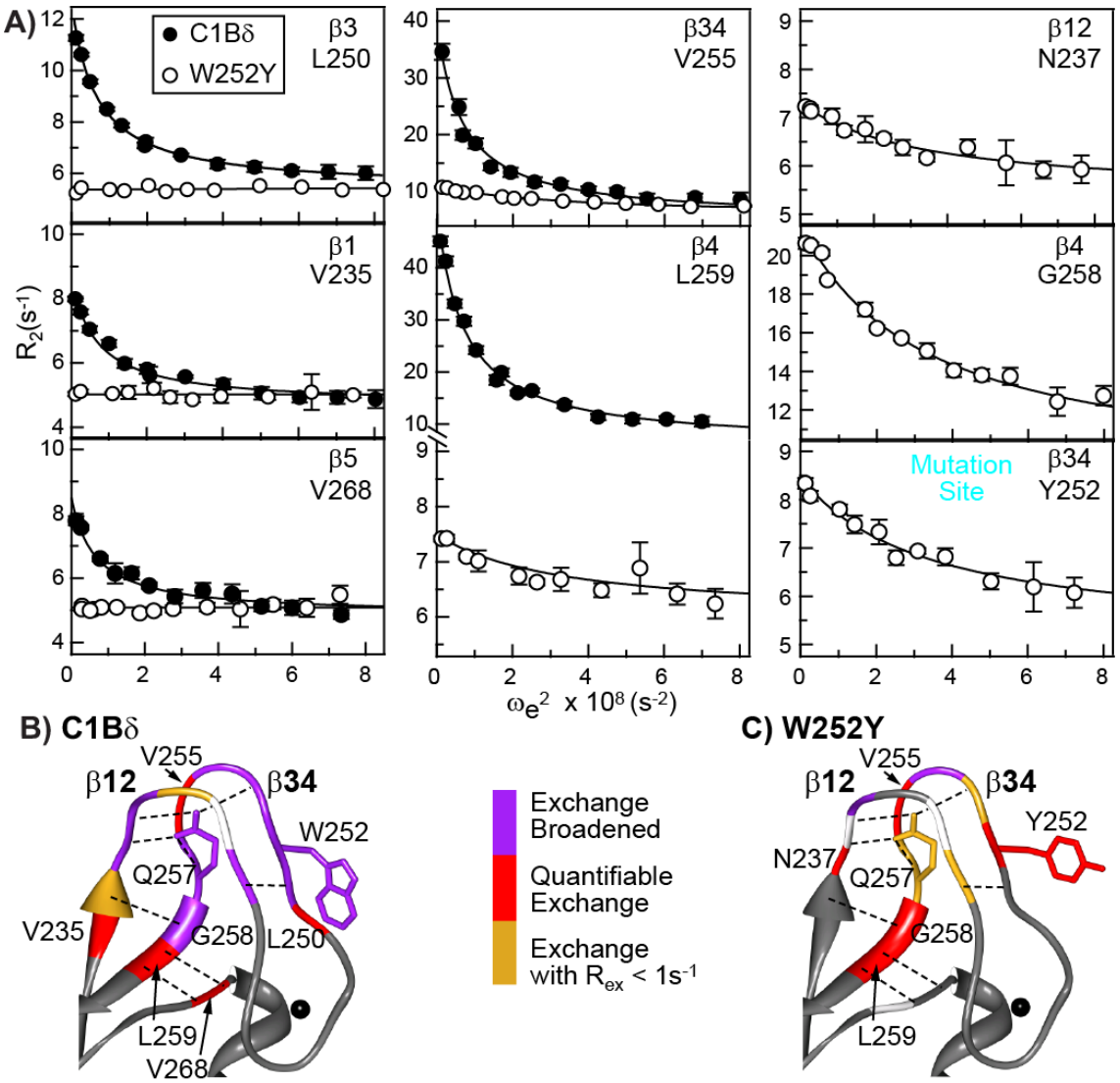

Figure 18. Conformational exchange in loop residues is attenuated in W252Y. A) Relaxation dispersion data measured with $R_{1\rho}$ experiments at 14.1 T are shown for the five residues with quantifiable dispersion in C1Bδ (filled circles) and W252Y (open circles). Curves are a result of globally fitting with data at 14.1 T and 11.7 T. Data for Asn237, Gly258, and Trp252 (right column) were not available for C1Bδ due to severe exchange broadening. The location of residues broadened beyond quantification (purple), quantifiable with $R_{1\rho}$ (red), and in exchange with R_{ex} less than $1s^{-1}$ at 11.7 T (yellow) are mapped onto (B) C1Bδ crystal structure (1PTQ) and (C) a mutant in which Trp252 is replaced with Tyr using Swiss PDB viewer. Proline and unresolved residues are colored white. Loop stabilizing hydrogen bonds are shown with black dotted lines.

Table 2. Parameters from $R_{1\rho}$ global fitting.

Residue	R_2^0 at 14.1 T	R_2^0 at 11.7 T	Φ_{ex} x 10^3 (s^{-2})
C1Bδ global k_{ex} = 8100 ± 200 s^{-1}			
L250	5.38 ± 0.28	5.30 ± 0.24	58.7 ± 5.4
L259	5.89 ± 0.41	5.32 ± 0.32	388.8 ± 8.8
V235	4.70 ± 0.28	4.69 ± 0.25	32.7 ± 5.3
V255	5.09 ± 0.34	4.96 ± 0.28	279.0 ± 7.3
V268	4.86 ± 0.29	4.92 ± 0.24	29.5 ± 5.5
W252Y global k_{ex} = 18,300 ± 900 s^{-1}			
G258	8.38 ± 0.45	7.24 ± 0.32	239.7 ± 17.7
L259	5.69 ± 0.23	5.63 ± 0.13	27.6 ± 4.9
N237	5.38 ± 0.17	5.15 ± 0.13	35.3 ± 5.0
V255	5.99 ± 0.16	5.24 ± 0.17	95.9 ± 8.0
Y252	5.09 ± 0.19	4.53 ± 0.15	61.8 ± 6.4

Probing changes in loop conformations with H_2O exchange rates

Water exchange rates for apo C1Bδ and W252Y were measured using CLEAN-EX and hydrogen-deuterium exchange (HDex) methods. Half of the C1 domain residues exchange at a rate quantifiable with one of these two methods. The rates for quantifiable residues are plotted in Figure 19A, and the approximate exchange rate for each residue is mapped onto the structure in Figure 20. The lack of large differences in exchange rates is consistent with the two domains having a similar structure in the dominant conformation. In many cases, a slow rate of amide to water exchange correlates with the amide forming a hydrogen bond in the protein structure.[92-94] For both constructs, the residues which were quantifiable with CLEAN-EX are located on the tips of the ligand binding loops, the exterior side of the α-helix and near the C-terminus. None of these

rapidly exchanging residue's amide groups adopt a hydrogen bonding geometry in the crystal structure. The residues exchanging slowly with water were quantifiable with HDex and are located in the β-sheets and zinc binding regions of the tertiary structure. All of the amide groups with hydrogen bonding geometry in the β-sheets slowly exchange with water (green or blue in Figure 20), as would be expected.

Contrary to the prediction from the structure, the amides found in hydrogen bonding geometry which originate from or coordinate to a side-chain atom to form the inter-loop network, are exchanged to deuterium to a point beyond detection in the first HSQC in both C1Bδ and W252Y. This includes the three amides participating in the four hydrogen bonds formed by the Gln257 side-chain, as well as the Lys256 backbone amide on the β34 loop, which is hydrogen bonding with the side-chain of a β12 loop residue, Asn237 (amide residues are yellow in Figure 20). These hydrogen bonds are likely less stable than those formed by the core of the protein, consistent with the theory that their loss/formation leads to a change in loop conformations which gives rise to the conformational exchange described above.

Because most of the ligand binding loop residues exchange in a timescale between what is quantifiable with either CLEAN-EX or HDex, it is difficult to speculate on differences between C1Bδ and W252Y in loop hydrogen bonding patterns. However, the largest quantifiable differences in water exchange rates between C1Bδ and W252Y are seen for Ser240 and His270 as plotted in Figure 19B. His270 is located on the α-helix, close in tertiary structure to the mutation site, while Ser240 is located on the β12 loop, across the ligand binding cavity from the mutation site (Figure 19C). The faster

exchange of His270 and slower exchange of Ser240 in C1Bδ, when compared to W252Y, is consistent with C1Bδ existing in a more "closed-loop" form in which the β34 loop is shifted toward the β12 loop and away from the α-helix. However, because what is measured is the exchange rate of the averaged populations in conformational exchange, it is not possible to say from these data if C1Bδ is slightly more closed when compared to W252Y in one or both of the conformations, or if it samples the same closed population but more frequently than W252Y.

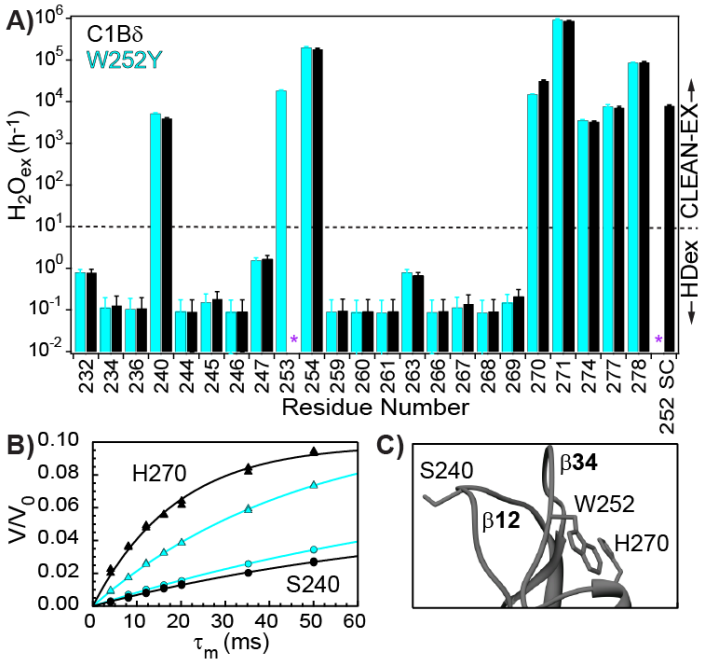

Figure 19. Water exchange rates determined by CLEAN-EX and HDex experiments. Exchange rates are plotted for quantifiable residues in (A) for C1Bδ (black) and W252Y (cyan). (B) The ratio of the CLEAN-EX peak volume (V) at a given mixing time (τ_m) divided by the peak volume in the reference fHSQC (V_o) for His270 (triangles) and Ser240 (circles) in both C1Bδ (black) and W252Y (cyan). Curves are a result of the fit to Equation 10. C) The location of Ser240 and His270 relative to the mutation site and the β34 loop in the C1Bδ crystal structure.

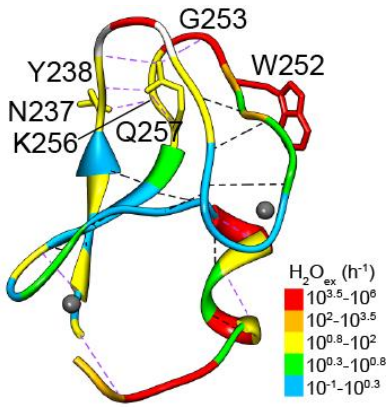

Figure 20. Ranges of C1Bδ water exchange rate ranges mapped onto the structure. The range in yellow was determined by residues which exchange in a timescale between what is observable for CLEAN-EX or HDex. When C1Bδ residues were exchanged broadened, the residues are colored according to W252Y. The Trp252 side-chain is colored based on exchange of $H_{\varepsilon 1}$. Pro241 and Met239 for which data are not available are colored white. The hydrogen bonds found in the crystal structure are shown with dashed lines. Those involving an amide group in slow exchange are shown in black, while the others are shown in purple.

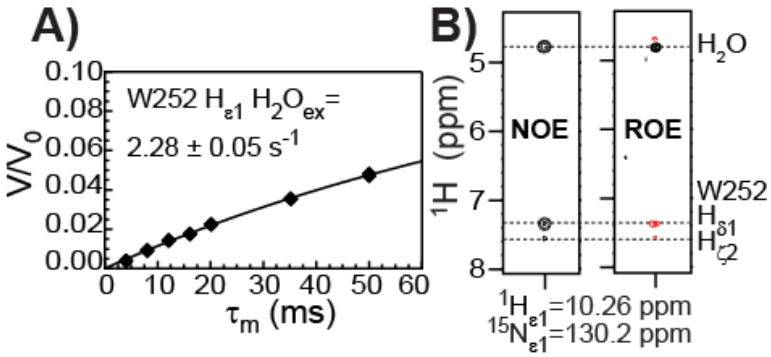

Figure 21. Trp252 side-chain solvent accessibility. A) The ratio of the CLEAN-EX peak volume (V) at a given mixing time (τ_m) divided by the peak volume in the reference fHSQC (V_o) for the W252 side-chain amide. B) NOE and ROE cross-peaks from the W252 side-chain amide. Red cross-peaks are opposite the sign of the diagonal.

It is also interesting to note that the W252 side-chain amide proton, $H_{\varepsilon 1}$, exchanges rapidly with water at a rate of 2.3 s^{-1} as shown in Figure 21A. In addition, $NH_{\varepsilon 1}$ gives rise to a strong NOE cross-peak in ^{15}N-edited NOESY at the resonance of

water that can be seen in Figure 21B. Also shown in Figure 21B, ^{15}N-edited ROESY revealed this cross-peak has the same sign as the diagonal, indicating it is due to chemical exchange.[95] No other inter-residue NOE cross-peaks were found in these NOESY experiments or in aromatic ^{13}C-edited NOESY. Together, these data support the theory that the W252 side-chain is predominantly solvent exposed without contacts with other residues.

Discussion

The objective of this study was to investigate the properties of C1 domains that produce varying DAG binding affinities. This is an important objective to achieve in order to eventually develop drugs which target a specific C1 domain to bring about an intended action on a specific PKC isoform or signaling protein. It was previously established that the identity of the residue at position 22, whether Trp or Tyr, tuned the DAG affinity of the C1B domain from PKCδ and PKCβ and led to differing cellular localization.[28] However, this residue does not make direct ligand contacts in the crystal structure of C1Bδ bound to a water soluble phorbol ester.[22] Therefore, it is unclear how to use this information to engineer a drug that can take advantage of this difference. These experiments investigate the underlying changes in structure or dynamics that are brought about by this varying residue and lead to drastically different DAG binding affinities, in attempts to eventually target these differences.

First, it is established that differences in DAG affinity seen by Newton's group were mimicked by the lone C1B domains in this *in vitro* system. This was evidenced by the titration of C1Bα, C1Bδ, and their position 22 mutants, Y123W and W252Y, with

DOG in the presence of mixed micelles, which serves as a membrane mimic and keeps the resulting complex soluble. Fitting of the change in Trp fluorescence or chemical shift measured by NMR resulted in K_d's that follow the same trend seen in C1Bδ and C1Bβ and their position 22 mutants studied by Newton's laboratory (Figure 6 and Figure 13); in both conventional and novel isoforms, DAG affinity is increased when a Trp is at position 22. In addition, phorbol ester binding affinity remains high as demonstrated by binding on the slow NMR timescale (Figure 7 and Figure 15) regardless of Tyr or Trp at position 22, which was also the case for C1Bβ.[28]

In spite of the differences in binding affinities, the structure does not change significantly based upon the identity of position 22. This is based on the similarity in the chemical shifts of the wild-type and mutant proteins in the apo-state, as well as bound to DOG in the presence of mixed micelles (Figure 8 and Figure 16). This is consistent with the available C1 domain structures revealing similar structures for constructs with Trp or Tyr at position 22 (example in Figure 3). In addition, Figure 8B shows similar residual dipolar coupling values of PKCα and Y123W. Residual dipolar coupling values reflect changes in the backbone angle relative to the alignment of the protein in the magnetic field, thus report directly on the protein structure. Together, these data provide strong evidence for the residue at position 22 modulating DAG affinity without having a significant effect on the structure.

In the absence of structural changes, the dynamic properties of apo C1Bδ and W252Y are explored. Intrinsic dynamics on timescales ranging from the sub-ns vibrational motion to the millisecond timescale conformational exchange have been

found to correlate with ligand binding affinity and specificity in other protein systems.[96] Model-free analysis was used to determine S^2 order parameters for C1Bα and Y123W, while reduced spectral density mapping was applied to C1Bδ and W252Y. Both methods revealed the fast vibrational motions on the sub-ns timescale are not affected by the identity of residue 22 (Figure 9A and Figure 17A). In contrast, differences in R_2 rates revealed a dramatic quenching in conformational exchange dynamics of the ligand binding loops when Trp was at position 22 instead of Tyr (Figure 9B and Figure 17B). Quantification of the process using $R_{1\rho}$ revealed that all of the constructs are undergoing a fast conformational exchange process involving the ligand binding loop residues; but, the exchange is faster in the Tyr containing constructs, with fewer loop residues affected by the process.

Table 3 lists the results of $R_{1\rho}$ and binding measurements of all four constructs, showing the similar trend observed in both novel and conventional PKC isoforms. The decrease in k_{ex} for Trp containing constructs (1.6-fold for PKCα and 2.3-fold for PKCδ) means the presence of Trp at position 22 lowers the k_1, k_{-1}, or both. Because the apo chemical shifts which represent the weighted average of the two conformations are not considerably affected by the identity of residue 22, the excited state is very minor in comparison to the ground state, thus k_1 is much larger than k_{-1}. Therefore, it is most likely that the k_{ex} differences are due to Trp at 22 lowering k_{-1} by increasing the stability of the excited state, which would contribute least to the observed apo chemical shifts.

Table 3. DOG binding affinity and conformational exchange summary for novel and conventional C1B and their position 22 mutants.

C1B Domain	Residue 22 Identity	Total with $R_{ex} > 0$ (# fit)	k_{ex} (s^{-1})	K_d (μM)
C1Bδ	Trp	18 (5)	8,100 ± 200	< 0.17
W252Yδ	Tyr	11 (5)	18,300 ± 900	5.2 ± 0.5
Y123Wα	Trp	13 (9)	9,600 ± 200	< 0.23
C1Bα	Tyr	7 (5)	15,400 ± 400	24 ± 2

The location of the exchanging residues in the structure, in combination with previous C1 structural and dynamic studies, provides insight into the possible exchanging conformations. The conserved QG motif in all DAG binding C1 domains (Figure 3) is involved in five of the six hydrogen bonds that stabilize the ligand binding loops according to the C1Bδ crystal structure.[22] All of the residues in this hydrogen bonding network both in the loops and at the loop hinges are in exchange in the Trp containing constructs, while only the residues in the loops and in the β4 hinge region show significant dispersion when Tyr is at position 22 (Figure 11C and Figure 18B and C). Further importance of this hydrogen bonding network to DAG affinity comes from mutating this conserved Gln residue to Glu such that two of the 6 loop stabilizing hydrogen bonds is eliminated in both C1Bα[97] and C1Bδ.[98] While the mutant C1B domains still bound phorbol ester, binding to DAG or a cyclic-DAG-mimic was eliminated or severely attenuated, respectively. In addition, the amides in this side-chain hydrogen bonding network undergo ^{1}H exchange with water more rapidly than other residues in hydrogen bonding geometry in the structure (Figure 20). This is further supported by molecular dynamics simulations using a structure from the C1Bα NMR

structure ensemble, which revealed ligand binding loop opening correlates with the partial loss of Gln128 hydrogen bonding network.[97] Taken together, these studies suggest the conformational exchange is due to the transient forming and breaking of ligand binding loop hydrogen bonds.

Specifically, I propose that a closed loop conformation is the high energy state sampled in solution and is more stabilized in the Trp containing constructs. This conformation which contains the hydrogen bonding network between the loops holding them in close proximity to one another, is the conformation competent for DAG binding. This hypothesis is supported by the conformational exchange rates of the Tyr and Trp containing C1B constructs presented here and previously, the Gln128 mutant which destabilizes the closed loop conformation and eliminates DAG binding, the molecular dynamics simulation which reveals hydrogen bond loss and loop opening takes longer in the Trp containing construct, and the differences in H_2O exchange rates of C1Bδ and W252Y (Figure 19). Furthermore, a measurement of C1 binding loop tip-to-tip distance in the solution ensembles of five different PKC C1 domains (C1Aδ, C1Aθ, C1Bθ, C1Bα, and C1Bγ) reveals the ligand opening sizes all vary, with the least variability being 2 Å (C1Bγ) and the largest over 5 Å (C1Bθ). Another indication of binding loop dynamics is seen in the high B-factors for the ligand binding loops in a recent C1Bδ crystal structure solved to 1.3 Å.[99] This hypothesis also lends insight into the dramatic differences in affinity for smaller ligands such as diacylglycerol and the large cyclic ligands such as bryostatins and phorbol esters. The lower energy open loop conformation can bind to the large ligand, while the higher energy closed loop

conformation is required to bind the smaller ligands. This insight coupled with a better understanding of the dynamic loop sampling taking place in the different C1 domains could be used to develop better drugs targeting a specific protein or PKC isoform.

It is difficult to speculate on the role that the Trp side-chain plays in stabilization of the closed loops. The Trp side-chain is solvent exposed and not involved in any detectable interactions according to the side-chain $H_{\varepsilon 1}$ rapid water exchange and lack of inter-residue NOEs (Figure 21). Position 22 side-chain is solvent exposed and mobile in all of the C1 solution structures, except for that of the weak DAG binding munc13 C1 where the side-chain is positioned between the ligand binding loops. However, the C1Bδ crystal structure reveals a π–π ring stacking between Trp252 side-chain and a conserved zinc coordinating His269. Since, the Tyr side-chain in not large enough to reach the distance to His269 and form this interaction, the π–π ring stacking between Trp252 and His269 could be stabilizing the higher energy closed loop conformation if it occurs in solution. Even when interacting with His269, the Trp side-chain is solvent exposed; therefore, it is not surprising that the $N_{\varepsilon 1}$ does not show dispersion in $R_{1\rho}$ when going from one solvent exposed state to another as the chemical shifts may not change.

In summary, NMR based ligand binding studies and relaxation measurements demonstrate the different properties of the conventional C1Bα and a novel C1B mimicking mutant, Y123W, as well as the novel C1Bδ and a conventional C1B mimicking mutant, W252Y. The Trp residue at position 22 increases the DAG affinity over an order of magnitude by one or both of the following mechanisms: 1) Trp side-chain stabilizes a high energy apo conformation that is competent for DAG binding

and/or 2) Trp side-chain more readily partitions into the hydrophilic/ hydrophobic interface than Tyr, increasing ligand-free membrane binding affinity, and in turn driving the first step of DAG binding. The second possible mechanism will be discussed in Chapter III. All of the data together provides a strong case for applying these driving mechanisms to understanding differences in ligand binding affinities amongst C1 domains from different PKC isoforms. By designing small molecules which bind a specific C1 domain to stabilize the open or closed conformation, or modulate the dynamics between the exchanging conformations, it may be possible to develop drugs for cancers and cognitive impairment with a single mode of action.

CHAPTER III

EFFECTS OF LIGAND BINDING AND POSITION 22 IDENTITY ON C1B MICELLE INTERACTIONS*

Background

The experiments presented offer insight into the interactions of C1B with a membrane-like hydrophobic environment and with membrane components that have been reported to activate PKC. In addition to revealing differences between isoforms that lead to their functional divergence, these interactions can also be used as restraints in order to determine the solution structure of C1B in the bound state. The binding studies presented in Chapter II revealed the residues affected by ligand binding in the presence of mixed micelles. However, it is difficult to separate the residues which are affected by ligand binding, by micelle binding, or by both events. These types of interactions will be required to determine the structure of a C1 domain bound to ligand in a hydrophobic environment. A better understanding of the C1 structure in the active form of PKC could reveal key interactions for targeting PKC for treatment of human diseases.

The first step in C1 ligand binding is thought to be an initial interaction with membranes in order to begin a two-dimensional search for membrane-bound DAG.[86]

* Parts of this chapter are reprinted with permission from Stewart MD, Morgan B, Massi F and Igumenova TI (2011) Probing the determinants of diacylglycerol binding affinity in the C1B domain of protein kinase Cα. Journal of Molecular Biology 408: 949-70. Copyright 2011 Elsevier.

However, as detailed in Chapter I, little is known about the affinity or identity of residues which interact with membranes in the absence of ligand. To investigate these properties, NMR studies were conducted on the C1Bα, Y123W, C1Bδ, and W252Y constructs used in Chapter II (Figure 4) in the presence of micelles, to mimic a ligand-free membrane-like environment. Surprisingly, these studies reveal a more extensive interface with micelles in the absence of ligand than when ligand is bound. In addition, Trp at position 22 increases the protein-micelle interface in C1Bα constructs and increases the ligand-free micelle affinity and depth of insertion in C1Bδ constructs. These differences in the initial membrane binding event likely play a role in the DAG affinities and specificities seen in the various PKC isoforms *in vivo*.

Currently, the only experimentally determined structure of a C1-ligand complex is the crystal structure of C1Bδ bound to a water soluble phorbol ester known as phorbol 13-acetate (P13A).[22] Three residues (Thr242, Leu251, and Gly253) form hydrogen bonds with the alcohol and carbonyl groups that are marked on the ligand structure in Figure 22. In addition, van der Waals interactions occur between the three-, five-, and seven-carbon rings of the ligand and the hydrophobic pocket formed by the β12 and β34 loops. P13A does not contain hydrophobic tails like most other phorbol esters. However, it is hypothesized that the tails do not contribute to binding, because the phorbol ester ring atoms where they attach make the least protein contact in the complex. This is supported by molecular dynamics studies using a more typical phorbol ester, phorbol 12,13 dibutyrate (PDBu), which show similar hydrogen bonding and van der Waals interactions as reported in the crystal structure.[100] Figure 22 shows the location of

the hydrophobic C_3H_7 tails on PDBu and highlights the ligand groups which form hydrogen bonds with C1 in the simulation.

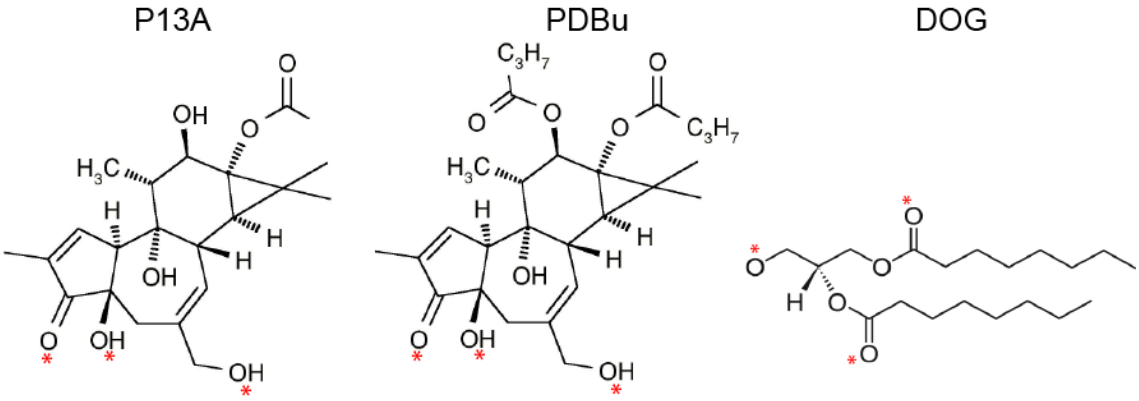

Figure 22. Structures of P13A, PDBu, and DOG. Groups predicted to form hydrogen bonds to C1 are marked with red asterisks.

None of these protein ligand contacts have been verified in solution or in a hydrophobic environment to more accurately represent the ligand-C1 complex in the cell. In order to test which residues are important for phorbol ester binding in a more native-like environment, binding experiments were conducted on 37 single residue mutants in the presence of lipids.[101] These studies revealed that all three mutants of the proposed Thr252 interacting residue retained tight binding, while mutation of the non-coordinating Leu254 resulted in complete loss of binding. The explanation of this is not clear from the crystal structure of the complex, highlighting the need for further investigation of the interactions in the C1-phorbol ester-lipid complex. Furthermore, ligand contacts with the diacylglycerol head group, the native C1 second messenger,

have only been predicted from docking studies (predicted hydrogen bonding functional groups are marked in Figure 22).

In this chapter, NMR is used to investigate C1Bα in the presence of P13A, PDBu, and PDBu in micelles. Comparison of the different ligand-bound states reveals an additive effect on most loop residues due to binding of the rings of the phorbol ester, the presence of the hydrophobic phorbol ester tails, and the presence of the membrane mimic. This is in contrast to the prediction from the P13A-bound crystal structure and simulations described above. A comparison of C1Bδ bound to micelles with the DOG/micelle binding studies in Chapter II reveals which residues are specifically affected by binding to micelles and those more affected by the presence of DOG. Furthermore, these studies reveal DOG binding causes a change in orientation of the C1 domain insertion in the membrane mimic. These changes in orientation could be transferred to the other regulatory domains to lead to the PKC activation by second messengers.

Phosphatidylserine (PS) is another important biological ligand of the C1B domain, because it both increases PKC activation and regulates cellular localization. Cellular localization is controlled primarily through isoform specific interactions with receptors for activated C-kinase (RACKs) as well as varying affinities for membrane components, such as PS, that are not equally distributed throughout the intra-cellular membranes.[102] Because the cellular localization regulates which substrates PKC has access to, the signaling events brought about by activation of different PKC isoforms strongly depend on the membrane specific localization.

While PS has been shown to be an activator of all PKC isoforms, the affinity and specificity varies between isoforms. In identical studies, PKCα was found to have a high affinity for PS compared to PKCε in both the presence and absence of DAG.[103] While both C1 and C2 domains have been reported to bind to PS, the C1 domain is thought to confer the specificity for PS over other anionic phospholipids.[104] However, this is not true for all isoforms. The C1 domain of PKCα, PKCβ, and PKCδ are specific for PS, while those of PKCγ and PKCε bind non-specifically to PS.[105] In this chapter, the effect of PS on DOG-bound C1Bδ is measured to propose the first ever PS binding site on a C1 domain. Similar studies using C1 domains from other PKC isoforms will be useful for determining the origin of PS specificity.

Methods

Micelle binding and affinity studies by NMR

C1Bα, Y123W, C1Bδ, and W252Y were prepared and assigned in the same NMR buffer as described in Chapter II. Uniformly ^{15}N enriched C1Bα and Y123W were added to 10 mM DPC/DPS micelles in a ratio of 7:3 and observed by HSQC. The protein residues which shifted or were severely attenuated were noted.

To obtain the relative affinities of C1Bδ or W252Y to DPC/DPS micelles, a fast-HSQC (fHSQC) [106] was collected using a Bruker 800 Avance system with a cryoprobe on separate samples containing varying detergent concentrations (5-200 mM) with 0.1 mM protein in the above NMR buffer with less salt 20 mM KCl). Titration curves were constructed for all cross-peaks that shift more than 0.05 ppm due to detergent addition by plotting the overall change in chemical shift (Δ) normalized to ^{1}H using Equation

1versus the absolute detergent concentration (L_0). The curves were then fit with Equation 2. Total chemical shift perturbation analysis was calculated as the difference between the apo spectrum and the spectrum at 75 mM detergent using Equation 1.

The depth of C1Bδ and W252Y insertion into the micelle in the presence and absence of DOG was probed using 1-palmitoyl-2-stearoyl-14-doxyl-sn-glycero-3-phosphocholine (14-doxyl PC), a lipid with a paramagnetic doxyl tag on the hydrophobic tail from Avanti. A fHSQC spectrum[106] was obtained using a Bruker 800 Avance system with a cryoprobe on a reference sample containing 100 mM mixed micelles (8:2 DPC:DPS), 0.15 mM protein, and NMR buffer with less salt (20 mM KCl). The paramagnetic sample contained the same concentration of DPC, DPS, and protein with 1.3 mM 14-doxyl PC incorporated into the micelles. The peak intensity ratio of the reference and paramagnetic spectra were determined using NMRpipe and then corrected such that the H231 ratio was unity. This ratio could then be compared between C1Bδ and W252Y in both the absence of DOG and in the presence of saturating concentration of DOG (1 mM). Experimental error was estimated from the root-mean-square noise level of the base plane in each spectrum.

Micelle-free ligand binding studies of C1Bα

In order to separate changes in chemical shift due to ligand binding from those due to micelle binding in the C1Bα species, micelle-free NMR studies were carried out on C1Bα 72 amino acid construct (C1Bα72) bound to P13A and PDBu. A 72 amino acid construct corresponding to residues 92-163 of C1B from PKCα *Mus musculus* gene was cloned into the PET SUMO vector from Invitrogen. Over-expression in *E. coli* and

isotopic labeling was carried out as described in Chapter II. The cells were lysed using BPER lysis reagent in the presence of lysozyme, DNAase, and HALT protease inhibitor (Thermo Scientific). The soluble fraction was purified using nickel affinity chromatography, and the fusion protein pooled and desalted into 20 mM tris-(hydroxymethyl)aminomethane buffer pH 7.0 with 150 mM NaCl. The buffer exchanged fusion protein was immediately cleaved using SUMO protease. Cleavage was > 90% complete in less than two hours. C1Bα72 was separated from SUMO and SUMO protease by nickel affinity chromatography followed by gel filtration. The pure protein was exchanged into buffer containing 20 mM MES pH 6.0, 8% D2O, and 0.02% sodium azide. All studies using C1Bα72 were performed in this buffer unless stated otherwise. Backbone assignments were carried out on the apo protein using triple resonance HNCACB and CBCA(CO)NH experiments.[61]

The water soluble phorbol ester, P13A, was obtained from Alexis Biochemicals and titrated into 80 μM C1Bα72 at concentrations between 0 and 2.4 mM in separate samples from a concentrated P13A stock in DMSO. DMSO was added to the P13A titration samples to maintain a constant 9% v/v. The change in chemical shift of either ^{1}H or ^{15}N for significantly shifting residues was fit to Equation 2 with K_d as a global parameter. The overall chemical shift perturbation was calculated using Equation 1 and the chemical shifts of C1Bα72 in apo and 2.4 mM P13A spectra.

A sample for solid-state studies was prepared by adding 3.3 mM PDBu in DMSO to 9 mg of 0.88 mM uniformly ^{15}N and ^{13}C enriched C1Bα72 in NMR buffer. The protein precipitation was ~80% efficient as analyzed by SDS PAGE. Solid-state spectra

were collected by Tatyana Polenova's group at University of Delaware. Two-dimensional NCO[107] and dipolar assisted rotational resonance (DARR)[108] spectra were used in combination with the three-dimensional spectrum of NCACX[109], to obtain nitrogen and non-aromatic carbon chemical shifts.

To ensure the precipitated protein represented the folded, PDBu-bound form, a sample similar to the above was prepared, then the unprecipitated protein in the supernatant was removed, and the pellet was resuspended in DPC/DPS micelles made in the C1Bα72mer NMR buffer described above. The sample was then observed with solution NMR ^{15}N HSQC. The cross-peaks from the 50 amino-acid "core" of the domain are very similar to the PDBu micelle-bound C1Bα53 described in Chapter II, indicating the PDBu-bound protein in the pellet is not disordered.

Measuring C1Bα detergent contacts

In order to determine the contacts between C1Bα and ligand/micelles, a sample of 0.5 mM C1Bα53, 0.65 mM PDBu, and 50 mM DPC/DPS micelles in a 7:3 ratio was prepared as described in Chapter II in the imidazole NMR buffer and 20 mM potassium chloride. Samples used for NOESY experiments contain 20% fully protonated DPC obtained from Avanti Polar Lipids in order to determine protein to DPC contacts. Samples used for ^{15}N edited NOESY contained ^{15}N uniform protein labeling. The sample used for ^{13}C edited NOESY was prepared with ^{15}N and ^{13}C uniformly enriched protein, lyophilized, and then resuspended in 99.99% D_2O. NOESY experiments were performed as described in the Varian BioPack User Guide using the supplied pulse sequence with a 100 ms mixing time on a Varian VNMRS 900 MHz instrument.

Detergent chemical shifts were assigned using literature values for similar molecules in similar conditions and a ^{13}C HSQC spectra of just the mixed micelles collected in a non-constant time manner on a Varian VNMRS 600 MHZ instrument.[110-112]

Results

Trp at position 22 in C1Bα mutant, Y123W, increases the interaction surface with ligand-free micelles

According to the current model,[86] the association of C1Bα with DAG- and phorbol ester containing membranes occurs via a two-step mechanism: 1) a non-specific association of the protein with membranes, and then 2) a two-dimensional search for the membrane-embedded ligand. To investigate the effect of the mutation on the initial membrane-binding event, ^{15}N-enriched C1Bα and Y123W were incubated with ligand-free DPC/DPS micelles. The ^{15}N -^{1}H HSQC spectra of the two proteins in the presence of micelles were collected and compared with those of the corresponding apo-states (blue compared to black spectra in Figure 6). In both C1Bα and Y123W, the intensities of several cross-peaks are substantially attenuated in the presence of micelles, sometimes leading to complete peak disappearance. This indicates that the kinetics of the binding process is intermediate on the chemical-shift timescale. In addition, several cross-peaks are shifted in the micelle-containing sample of Y123W compared to the apo-state.

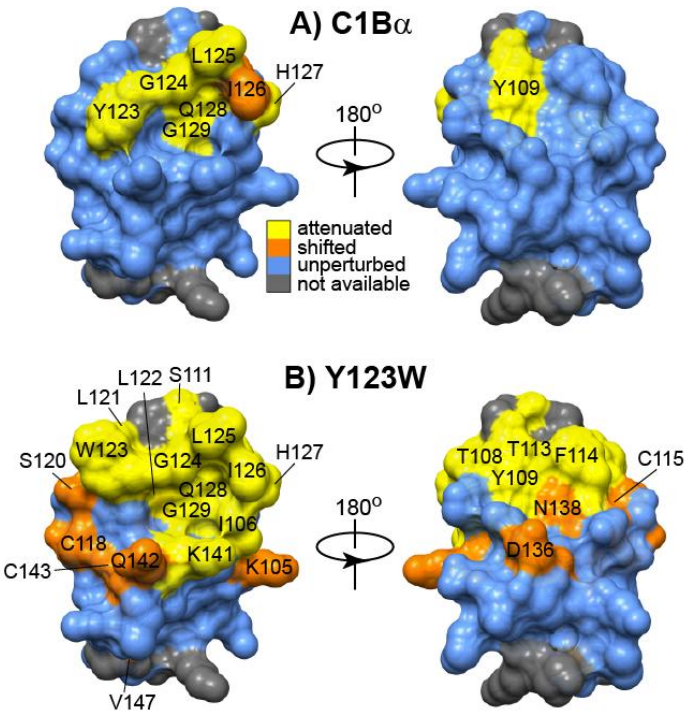

Figure 23. Mapping of the interaction surface of C1Bα (A) and Y123W (B) with ligand free micelles. The cross-peaks of residues that interact with DPC/DPS micelles are either significantly attenuated (yellow) or shifted (orange) compared to their positions in the micelle-free spectra. (A) In C1Bα, the entire β34 loop, comprising residues Tyr123-Gly129, and Tyr109 of loop β12 are involved in the interactions with micelles. (B) In Y123W, both β12 and β34 loops and several adjacent residues are involved in the interactions with micelles. In (B), the Tyr at position 123 was replaced with Trp in the ensemble-averaged NMR structure of C1Bα using WHATIF.[87] Overall, the total surface area involved in the interaction with micelles is larger in the mutant than in C1Bα.

The perturbed residues are mapped onto the structure of C1Bα in Figure 23 for C1Bα (A) and Y123W (B). In C1Bα, the intensities of cross-peaks corresponding to Tyr109 of loop β12 and the entire β34 loop comprising the Tyr123-Gly129 stretch are severely attenuated as a result of interactions with micelles. Compared to C1Bα, many more residues in Y123W respond to the presence of detergent micelles. They include the entire loop and hinge regions of β12 (Lys105-Cys115) and β34 (Ser120-Gly129). In

addition, residues Cys118, Asp136, Asn138, Lys141, Gln142, Cys143, and Val147 are also affected by interactions with micelles, as manifested in the change of their chemical shifts. It is evident that when mapped onto the C1Bα structure, the perturbed regions in the Y123W mutant form a surface that encompasses almost the entire top half of the domain. These results suggest that Trp at position 123 facilitates the interactions of C1Bα with DPC/DPS micelles. 25 residues out of the total 53 are affected by these interactions in the mutant, as opposed to just 8 in C1Bα. This difference in interaction modes disappears when the specific binding to DOG takes place, as shown in Figure 8C and D. Thus, the Y123W mutation most likely affects the kinetics of the association of C1Bα with lipid membranes in the two-step binding mechanism.[86]

Micelle-free phorbol ester studies exhibit varying degrees of C1Bα interaction with ligand rings, hydrophobic chains, and micelles

Due to the exchange broadening observed in C1Bα when bound to micelles, it is impossible to access the degree of chemical shift change due to micelle binding versus ligand binding. For this purpose, NMR studies were carried out on C1Bα bound to phorbol ester in the absence of micelles. The purpose of incorporating micelles in the ligand binding studies in Chapter II was not only to mimic the membrane where C1 binds to ligands in the cell, but also to provide solubility of the hydrophobic complex formed after ligand-binding. To avoid this problem for micelle-free ligand titrations, the water soluble phorbol ester, P13A, was used.

P13A was added to a 72 amino acid construct of C1Bα (C1Bα72) in a step-wise fashion up to 2.4 mM and observed by ^{15}N-^{1}H HSQC. The change in chemical shift of

all significantly affected residues could be plotted versus the ligand concentration and fit to Equation 2 to obtain a global K_d of 0.61 ± 0.01 mM. Representative residues can be seen in Figure 24. Because C1Bα binding of PDBu in the presence of micelles was slow-exchange on the NMR time scale (Figure 7), the affinity to phorbol ester with and without micelles cannot be directly compared. However, this binding is 25 fold weaker than even the weakly binding diacylglycerol in the presence of micelles. Conventional PKC C1B domains have been reported to bind to phorbol ester in the presence of liposomes in the low μM range. Using these data, the presence of a membrane mimic is estimated to enhance phorbol ester binding 50-75 fold.[28,104]

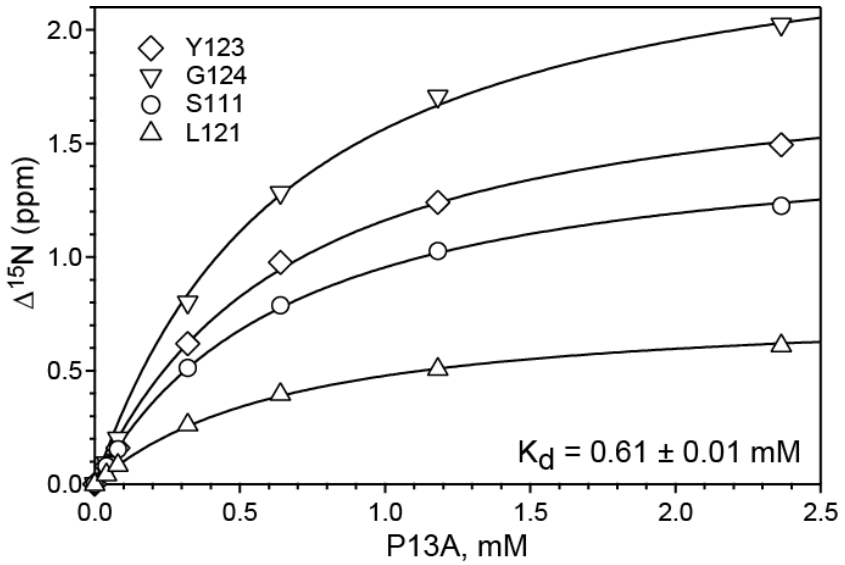

Figure 24. P13A affinity of C1Bα72 as measured by change in chemical shift during NMR observed titration. Curves represent a global fit of all significantly shifting residues to Equation 2 with a K_d of 0.61 ± 0.01 mM.

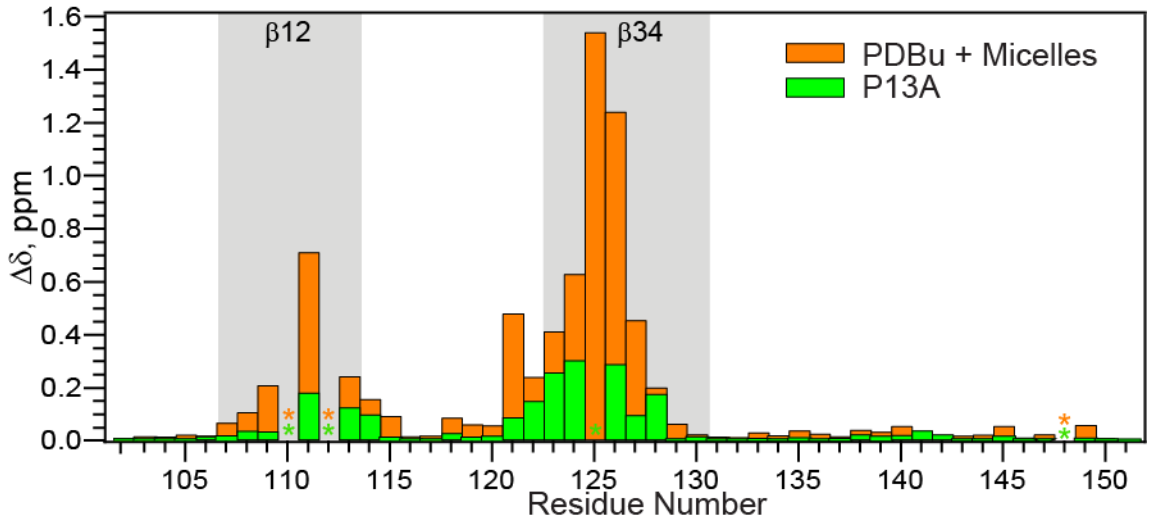

Figure 25. Chemical shift perturbation due to binding P13A (green) or PDBu in the presence of micelles (orange). Missing data are denoted with asterisks. The ligand binding loops are highlighted in gray.

The difference in chemical shifts between apo and P13A-bound C1Bα72 are plotted in green in Figure 25 for the residues in the core of the protein. Residues in both the β12 and β34 loops respond to P13A binding. Two proline residues (112 and 148), as well as two exchange-broadened residues (Gly109 in β12 and Leu124 in β34) are missing from the analysis (asterisks in Figure 25). This is in contrast to the spectrum of C1Bα72 bound to PDBu in the presence of micelles in which no residues are exchange-broadened beyond detection, including Gly109 which is missing in the apo spectrum. When considered with the exchange broadening observed upon binding micelles alone (Figure 23) this indicates that both ligand *and* micelles are needed to quench the conformational exchange observed in the loops in Chapter II.

When the change in chemical shift due to binding P13A is compared to the chemical shift differences due to binding PDBu in micelles (Figure 25), several residues

are almost equally perturbed, such as Phe114, Leu122 and Gln128. This indicates the change in environment experienced in these regions is due to phorbol ester binding, rather than burial in a hydrophobic environment. This is surprising since none of the amides from these residues are directly hydrogen bonded to the P13A ligand in the C1Bδ crystal structure. Instead, the amide groups which are reported to form protein-P13A hydrogen bonds (Gly124 and Thr113) only shift to half of the final perturbation seen when binding PDBu and micelles. This suggests that either the presence of micelles alters the structure of the protein-ligand complex or the protein-ligand interface is still accessible to detergent. With the exception of Thr113 and Phe114, the other residues in the β12 loop experience a vast majority of their chemical shift change from binding to micelles rather than ligand.

To determine if the differences seen here are due to the nature of the ligand itself (P13A versus PDBu) or due to the presence of micelles, a sample was prepared of C1Bα72 bound to PDBu in the absence of micelles. Because of the insolubility of the complex, uniformly enriched ^{15}N and ^{13}C protein was precipitated into a pellet by addition of the hydrophobic PDBu ligand. Then, solid-state NMR techniques were used to collect two-dimensional NCO and DARR spectra as well as a three-dimensional NCACX spectrum in order to determine the chemical shifts of non-aromatic ^{15}N and ^{13}C atoms in the protein. As demonstrated by the DARR spectrum seen in Figure 26, the spectra are nicely resolved and indicative of folded protein in the ligand-precipitated pellet.

All of the residues in the 50 amino-acid core of the protein are present in the spectra, except for the β34 loop residues Leu125, Ile126, and His127. Mobile residues are often missing from solid-state NMR spectra, indicating that this loop is likely undergoing motion even when bound to PDBu. This supports the claim in the previous section that both ligand and micelles are needed to quench the loop motion.

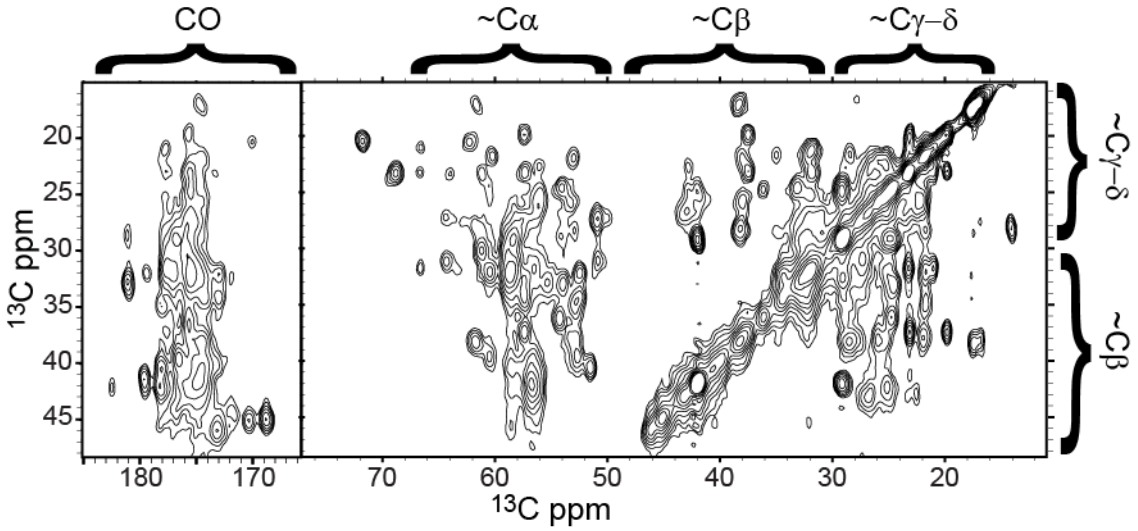

Figure 26. An excerpt of the solid-state DARR spectrum of C1Bα72 bound to PDBu. The spectrum reveals transfer from side-chain carbons (y-axis) to all side-chain and backbone carbons (x-axis) within the same residue. The approximate regions of carbon chemical shifts are labeled.

The changes in ^{15}N chemical shifts for non-proline residues in and around the ligand binding loops are plotted in Figure 27 for each of the three phorbol ester bound states. The three residues located in the loop hinge regions (Phe114, Leu122 and Gln128) that showed equal perturbation due to phorbol ester binding regardless of micelle presence also have equal shifts when using PDBu as the ligand. However, most

of the loop residues which showed significantly larger perturbation in the presence of micelles, have a PDBu-bound ^{15}N chemical shift between that of PDBu-bound in the presence of micelles and P13A-bound in solution. This indicates that the addition of the hydrophobic tails in PDBu compared to P13A as seen in Figure 22 do have an effect on ligand binding residues contrary to what was predicted from the P13A-bound C1Bδ crystal structure.[22] However, micelle binding in the presence of ligand still has the largest overall effect on the ligand binding loops. The degree of difference made by the presence of micelles will be better assessed by assignment of the ^{13}C chemical shifts for all non-aromatic side-chain carbons in the PDBu-bound solid-state spectra. These can then be compared with the chemical shifts of the same atoms in the PDBu micelle-bound C1Bα53 construct, which will be assigned in order to interpret the NOEs discussed in the next section.

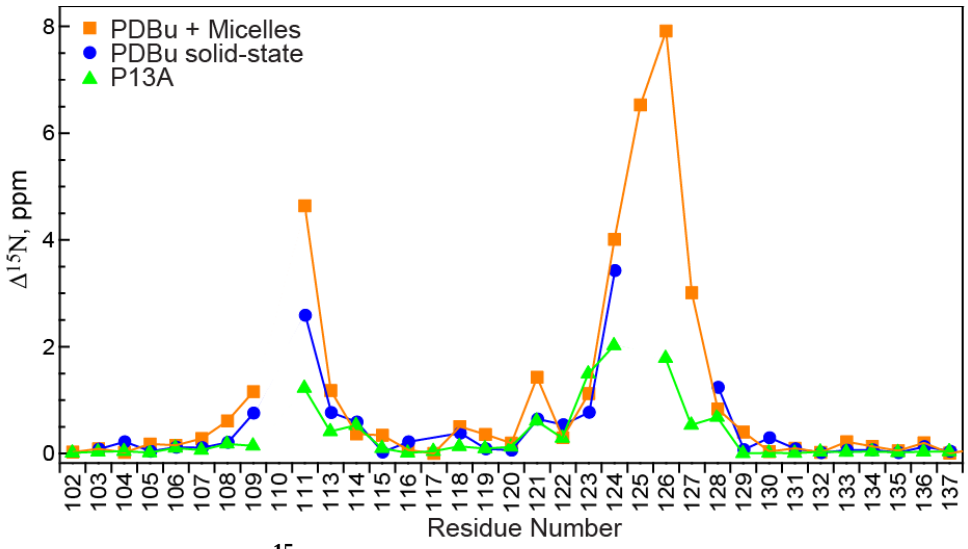

Figure 27. Comparison of ^{15}N chemical shift changes in phorbol ester bound states. The difference in ^{15}N chemical shifts of non-proline residues in and around the ligand binding loops between the apo-state and PDBu-bound-state in micelles (orange), PDBu-bound without micelles observed with solid-state NMR (blue), and P13A-bound without micelles(green). Lines connect sequential residues with available ^{15}N chemical shift data.

C1Bα detergent interactions revealed from NOESY experiments

Chemical shifts report on differences in the environment of a particular nuclei, which can occur either by direct binding to a ligand or changes in protein structure due to the ligand binding. To directly assess the proximity of affected residues to the detergent micelles, three-dimensional ^{15}N-edited and ^{13}C-edited NOESY spectra were collected. In these experiments, two dimensions are used to resolve a given ^{1}H-^{15}N or ^{1}H-^{13}C pair and NOE cross-peaks arise in the third dimension at the chemical shift of any ^{1}H within ~5 Å. The volume of the NOE cross-peak is proportional to the distance between the two ^{1}H atoms. The chemical shifts of ^{1}H in the detergent molecules were assigned as described in the methods section.

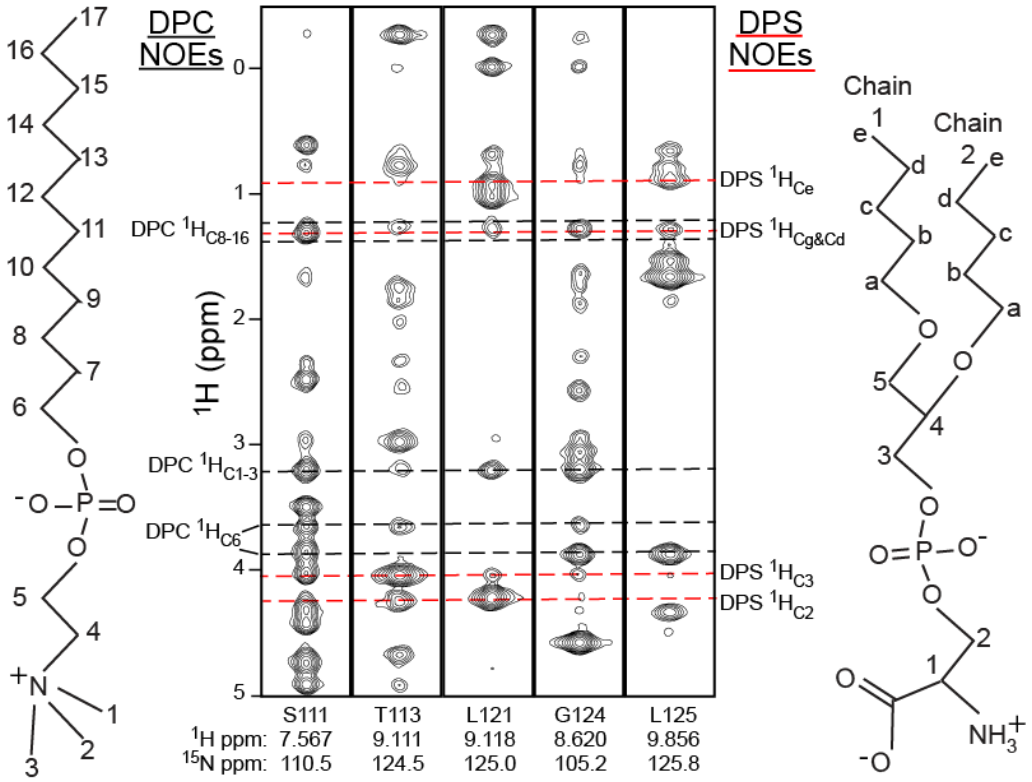

Figure 28. Strips of the ^{15}N edited NOESY spectrum illustrating NOE cross-peaks from loop residues to DPC and DPS. The NOE peak is labeled with the numbering corresponding to the DPC molecule shown on the left or the DPS molecule shown on the right and the chemical shifts are marked with a black (red) dotted line for DPC (DPS).

Figure 28 shows the NOEs detected from the backbone amides of residues in the ligand binding loop and hinge regions to ^1H's in DPC and DPS. An all-atom assignment of the protein is underway to assign the NOE cross-peaks with certainty. However, from the initial assessment of the hinge residues, Thr113 and Leu121, strong NOEs are observed to methylenes directly adjacent to the phosphate of DPS (C3 and C2 respectively). This indicates the hinge regions of the loops are in close proximity to the lipid head group, thus the surface of the micelle. Conversely, the residues in the loops (Ser111, Gly124, and Leu125) have stronger NOEs than the hinge residues to

methylenes in the hydrophobic tails of DPC and DPS, indicative of deeper insertion in the micelle. The ^{13}C- edited NOESY shows a similar pattern in the NOEs from the backbone Hα of the loop and hinge residues. Assignment of the side-chain atoms will provide more probes for assessing the degree of interaction with the detergent micelles. Not only do these experiments provide qualitative information about the placement of residues in the micelle, but quantification of the NOE cross-peak intensity will also supply valuable distance restraints for determining the first solution structure of a ligand-bound C1 domain once all ^{1}H in the protein and ligands are assigned.

Trp at position 22 in C1Bδ increases micelle affinity in the absence of ligand

Due to the intermediate exchange regime of micelle binding in C1Bα, it was not possible to measure the affinity to the micelles alone. To quantify micelle affinity and measure dependence on position 22 identity, C1Bδ and W252Y were titrated with 5-200 mM DPC/DPS mixed micelles and observed using NMR fHSQC spectra. Cross-peaks in both constructs gradually shift due to micelle binding to reflect an average of the bound and unbound populations (Figure 29A and B). This so called fast-exchange behavior allows for the K_d to be determined by fitting the change in chemical shift at increasing detergent concentrations to Equation 2 as shown in Figure 29E and described in the methods.

The residues in the β12 and β34 loops bind micelles with a higher affinity than residues in the α-helix, so global fitting was done separately for residues in these two groups. The groups are shown in Figure 29C and D. The C1Bδ residues in the β12 and β34 loops exhibit tight binding behavior. These curves can be fit with two straight lines

with an inflection point at 9.0 ± 0.3 mM as demonstrated for Leu250 in Figure 29E, which is set as the upper limit for the K_d of C1Bδ. This is significantly tighter than the loop residues in W252Y, which bind with a K_d of 10.9 ± 0.6 mM. While the α-helix from both constructs binds weaker than the β12 and β34 loops, the respective regions are each weaker in the W252Y mutant when compared to C1Bδ. Several residues located close to both the loops and helix in three-dimensional space also respond to micelle binding. These residues were fit individually with K_d's which range from 5.8 – 8.7 mM for C1Bδ and 16.1 – 21.9 mM for W252Y. These values are between the K_d's found for the loops and helix in each respective construct. While it is unclear what gives rise to the separate K_d values found in the loop residues versus helix residues, the following experiments in this chapter provide insight into the possible explanations. Overall, the mutation leads to at least 2 to 3-fold decrease in mixed micelle affinity for all regions of the protein that respond to micelle binding.

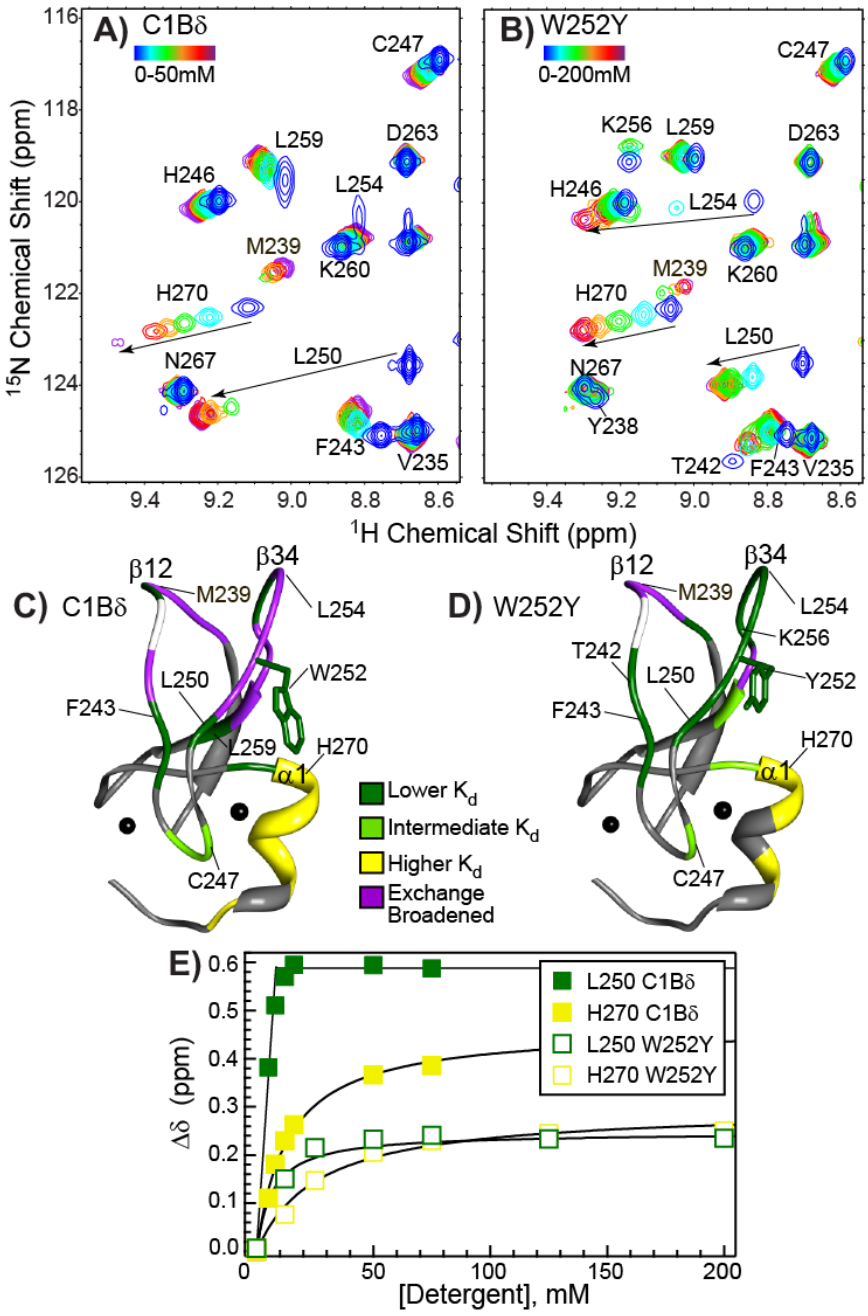

Figure 29. C1Bδ and W252Y binding to DPC/DPS mixed micelles. An overlay of HSQC spectra excerpts collected on uniformly ^{15}N enriched C1Bδ (A) or W252Y (B) at increasing concentrations of DOG micelles (blue to red rainbow-colored). Residues which fit with a lower K_d (dark green), higher K_d (yellow), or between the two K_d values (green) are highlighted on the crystal structure of C1Bδ (C) or W252Y homology model (D). (E) The change in chemical shift due to binding is plotted for representative residues that fit with a higher or lower K_d in yellow and dark green respectively. Curves represent the fit to Equation 2 with the "higher" or "lower" K_d as a global parameter.

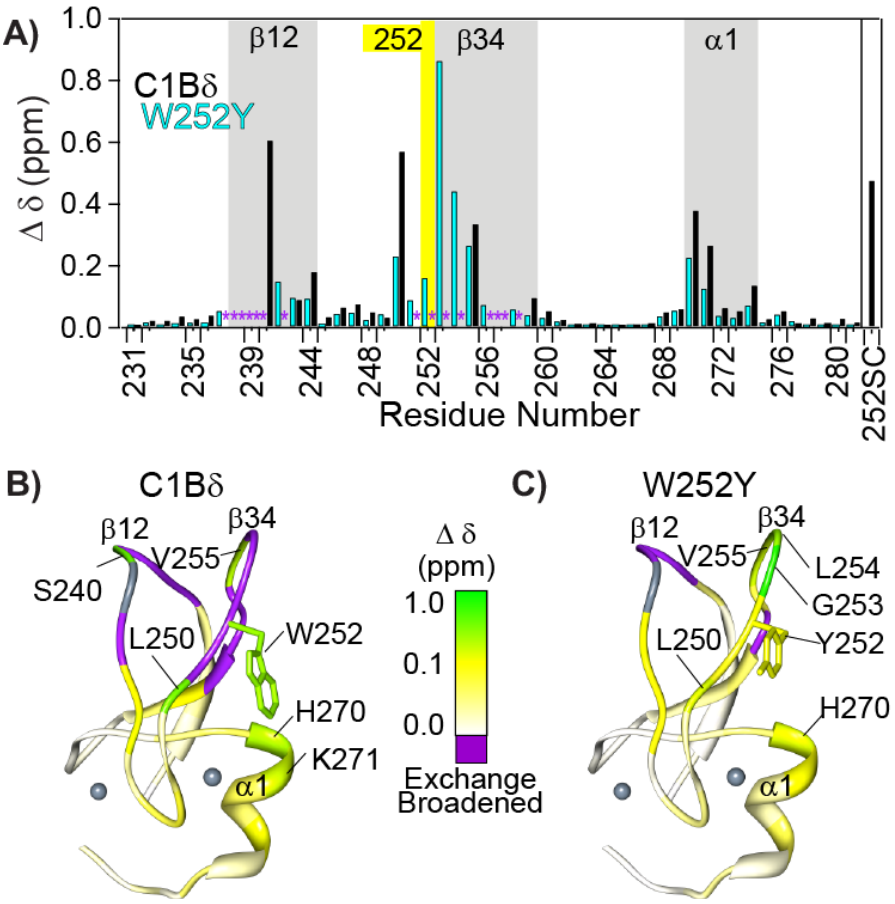

Figure 30. Chemical shift perturbation of C1Bδ and W252Y due to micelle binding at 0.75 mM detergent. The change in chemical shift calculated with Equation 1 is plotted in (A) and mapped onto the C1Bδ crystal structure in (B) and W252Y homology model in (C). Residues broadened due to conformational exchange are marked with purple asterisks in (A) or colored purple in (B) and (C). Trp252 side-chain is colored according to the shift of the $NH_{\varepsilon 1}$ amide. The figure shows that while binding occurs in the same region of both proteins, the chemical shift is larger in C1Bδ than W252Y for comparable residues.

C1Bδ and W252Y residues located on the α-helix and both ligand binding loops show a large change in chemical shift due to mixed micelle binding. The chemical shift perturbation is not quantifiable for many loop residues due to exchange broadening in apo, micelle-bound, or both spectra (colored purple or marked with a purple asterisk in

Figure 30). While the identities of affected residues are the same, comparison of the six significantly shifting residues that are quantifiable in both constructs reveals a greater chemical shift perturbation due to micelle binding in the C1Bδ construct.

Interestingly, the change in chemical shift due to micelle binding of $NH_{\varepsilon 1}$ on the Trp252 side-chain is 90% of the overall chemical shift change seen due to DOG binding in micelles. This supports the hypothesis drawn in Chapter II that the side-chain does not contact the ligand, and likely does not change structure based on ligand binding. In addition, it alludes to the importance of the position 22 side-chain in the initial partitioning into the interface of hydrophilic / hydrophobic environment of the micelle, which mimics the membrane interface.

The backbone of several residues display similar behavior, in that > 80% of the chemical shift change they experience upon binding DOG in micelles is also seen for binding micelles in the absence of DOG (Figure 14 and Figure 30). In W252Y, three significantly shifting residues fall into this category: Asn237, Cys244, and Leu254. The first two residues form the β12 hinges and Leu254 is located on the tip of the β34 loop. In C1Bδ, two of the above residues are broadened beyond detection, but Cys244 displays the same behavior as in W252Y. In addition, Leu259 on β4, and the helix residues Lys271 and Glu274, also have this pattern. These data are reminiscent of what was observed in the C1Bα72 micelle-free ligand binding studies: that the loop hinge regions and helix residues interact more with the micelle, as opposed to directly with the ligand.

Leu254 is the only residue in the middle of the ligand binding loop that responds mostly to micelle binding rather than DOG binding. This residue also has the largest chemical shift difference between PDBu and DOG binding (both in the presence of micelles). Leu254 PDBu-bound versus DOG-bound chemical shift difference is greater than 1.2 ppm, while the difference between the cross-peaks for other residues in these two spectra, even those proposed in hydrogen bonding interactions, are less than half of that. Together, this indicates Leu254 is likely distanced more from DAG, than it is from phorbol ester in three-dimensional space. This provides a restraint for the eventual structure determination of C1B bound to DAG and indicates a difference from the phorbol ester-bound structure.

DPS interacts with C1Bδ β34 loop and α-helix

In order to determine which residues bind to DPS in the mixed micelles used in these studies, the chemical shifts of DOG saturated C1Bδ in mixed micelles (DPC/DPS 7:3 ratio) is compared with those in micelles composed of only DPC. The HSQC of these two samples are overlayed with the apo-state as shown in Figure 31. The residues with a large change in chemical shift due to DPS incorporation in micelles are located at the N-terminal side of the α-helix, and in the hinge regions of the β34 ligand bind loop (indicated with red arrows in Figure 31A and mapped onto the structure in Figure 31C). Interestingly, the residues on the β12 loop and at the tip of the β34 loop, which show a strong response to DOG binding in DPC micelles, are not significantly affected by DPS incorporation (Figure 31C).

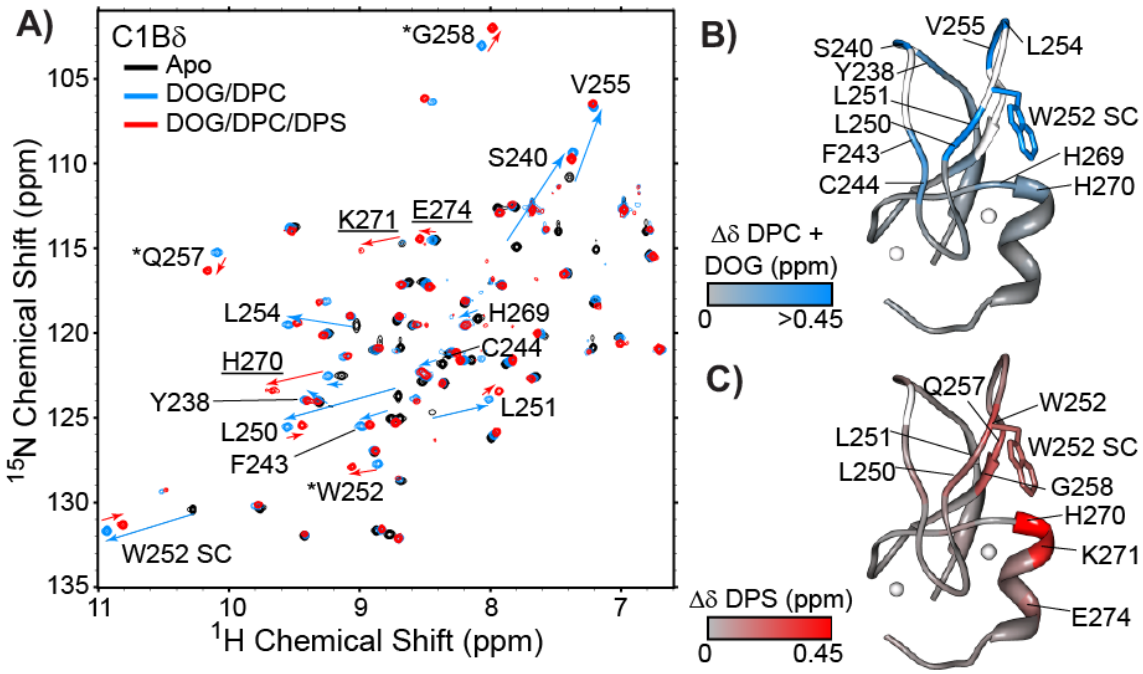

Figure 31. The effect of DPS micelle incorporation on C1Bδ chemical shifts. A) Overlay of C1Bδ ^{15}N-^{1}H HSQC spectra in the apo-state (black), bound to 0.5 mM DOG in the presence of 10 mM DPC micelles (blue), or the same DOG and micelle concentration with 30% DPS incorporated (red). Significantly affected residues are labeled on the spectra. Asterisks denote residues with missing apo peaks due to broadening and helix residue labels are underlined. The change in chemical shift due to binding DOG in DPC micelles is shown with blue arrows in (A) and mapped onto the C1Bδ crystal structure with a gray to blue gradient in (B). The difference in chemical shift due to DPS incorporation is shown with red arrows in (A) and mapped onto the structure with a gray to red gradient in (C). For both (B) and (C), the residues with missing data and zinc atoms are colored white. Residues in the β12 and β34 loops are drastically shifted due to DOG/DPC binding, while residues in the α-helix are mostly shifted due to DPS incorporation.

As shown by the red arrows compared to the blue arrows on the HSQC spectra, the vast majority of the perturbation experienced by the α-helix residues (underlined in Figure 31) when binding DOG in mixed micelles is due to the presence of DPS. The identities of the α-helix residues most perturbed by DPS incorporation are His270, Lys271, and Glu274. His, Lys, and Glu residues were also identified as the DPS binding

residues in the conserved membrane-targeting FYVE domain.[113] This indicates the changes in chemical shifts observed for these residues in C1Bδ are likely due to direct DPS binding rather than a change in protein or micelle structure from DPS incorporation. These residues and those in close proximity also respond to DPC/DPS micelle binding with a separate and weaker K_d from the loop residues in the previous section (Figure 29). Given the separation of residues by affinities looks very similar to the separation seen due to DPC versus DPS binding, the residues identified here likely represent the first known phosphoserine binding site in a C1 domain.

Comparison of the overall chemical shift changes due to DOG/DPC/DPS binding to those of DOG/DPC binding also indicates the C1B domain changes orientation in the micelle in such a way that the helix is closer to the micelle. This was also observed in the micelle binding study of the FYVE domain, which changes orientation 25º upon binding DPS.[113] To test changes in orientation of C1Bδ in micelles as well as test for direct micelle binding of the α-helix residues, the micelle proximity of each residue is measured in the next section.

DOG binding and position 22 identity change the depth and orientation of CIBδ in micelles

Differences in micelle orientation are indicated by the effect of DPS as discussed in the previous section. In addition, C1Bα and Y123W studies with ligand free micelles discussed above point to a difference in the protein interface with ligand-free micelles that could not be measured in these constructs due to the intermediate NMR timescale. To gain insight into the effect of ligand binding and the position 22 identity on the

interaction with micelles, the depth of insertion of C1Bδ and W252Y into micelles is probed in both the presence and absence of DOG. This was done through incorporation of small quantities of a lipid with a paramagnetic tag on the 14th carbon (14-doxyl PC) into the mixed DPC/DPS micelles. The paramagnetic relaxation effect (PRE) due to the proximity of a residue to the paramagnetic tag was determined by comparing the peak volumes in an fHSQC spectrum from identical samples with and without 14-doxyl PC. In addition to revealing differences in insertion due to residue 22 identity, the PRE values can be used as restraints in future structure refinement.

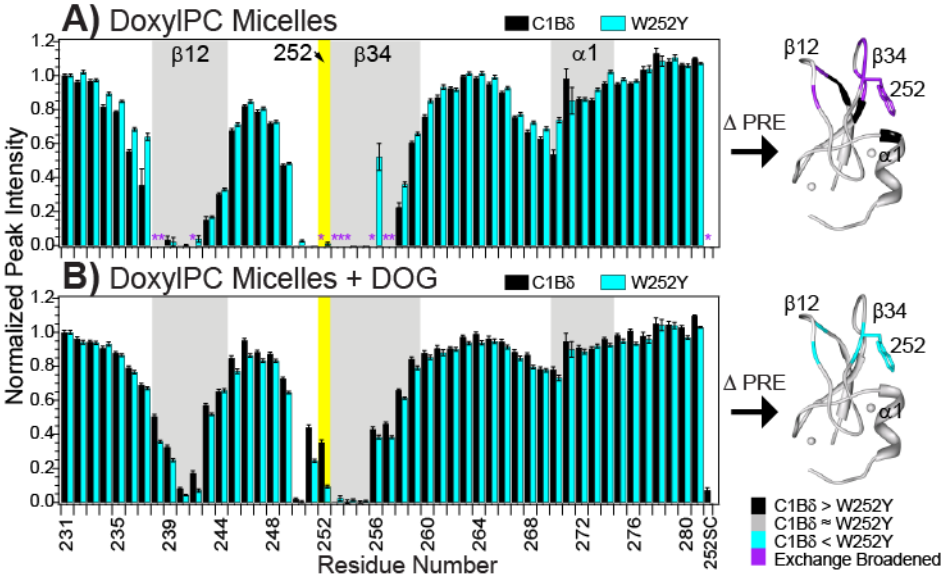

Figure 32. Depth of micelle insertion measured with paramagnetic relaxation enhancement (PRE). Doxyl-14 labeled PC is incorporated in mixed micelles (A) or mixed micelles with DOG (B). PRE is plotted for C1Bδ (black) and W252Y (cyan) normalized to His231. The differences in PRE between C1Bδ and W252Y are mapped onto the C1Bδ apo crystal structure to the right of the graphs.

In both the presence and absence of DOG, the largest PRE was seen for residues in the β12 and β34 loops, with significant PRE for residues on the N-terminal side of the α-helix (Figure 32). This is consistent with the two most N-terminal α-helix residues (His270 and Lys271) interacting with the DPS head groups as proposed in the previous section. An interaction with the DPS head groups would bring the helix residues close enough to the paramagnetic tag located in the hydrophobic core of the micelle to affect their relaxation properties. However, they would not be expected to be relaxed beyond detection as observed for the loop residues that are inserted into the hydrophobic core of the micelle.

Both constructs have a significantly larger PRE in the absence of DOG for residues in the β12 and β34 loops and two residues which are on the N-terminal side of the β34 loop (Ser249 and Leu251) when compared to the PRE in the presence of DOG (Figure 32). In addition, C1Bδ residues on the N-terminal side of the β12 loop (Tyr236 and Asn237), residues between the loops (245-258), and residues on the N-terminal side of the α-helix (267-270) are also more inserted in the absence of DOG than when it is present. In the context of the mutant these residues do not significantly change the depth of insertion based on DOG presence. This indicates that while both constructs have a more extensive interface with ligand-free micelles than in DOG-bound micelles, the Trp containing construct varies more due to ligand binding.

Residues with a significantly different PRE between C1Bδ and W252Y are highlighted in Figure 32 on the apo C1Bδ crystal structure (1PTQ). In the absence of DOG, C1Bδ residues at the back of the binding loops in the shown orientation are more

inserted than they are in W252Y (colored black in Figure 32A). However, once the constructs bind to DOG, both sides of the ligand binding loops are more inserted in the W252Y construct (cyan residues in Figure 32B). This means that both DOG binding and position 22 identity lead to different orientations in the membrane-like environment.

Discussion

The goals of the ligand and micelle studies presented in this chapter were twofold: 1) Determine the effect of residue 22 identity on affinity and interaction with micelles. 2) Establish which residues interact with the ligand, the micelles, or both for use as structural restraints in future NMR structure determination. For C1Bα constructs, ligand binding was assessed with solution NMR titrations of hydrophobic ligands (DOG and PDBu) in the presence of micelles, solution NMR titration of a hydrophilic ligand (P13A) without micelles, and solid-state NMR studies bound to a hydrophobic ligand (PDBu) in the absence of micelles. Micelle binding could not be accessed directly due to the intermediate exchange regime. However, in C1Bδ constructs, the effects of residue 22 identity on micelle binding can be determined, as well as differences in residues involved in micelle binding versus ligand binding.

Both Trp and Tyr have been found to localize to the same part of lipid bilayers: the interface of the hydrophobic tails and hydrophilic head groups.[114,115] However, Trp partitions more readily into the interface.[116] To determine the role of Trp at position 22 in C1 domain membrane partitioning, the affinity of C1Bδ and W252Y for DPC/DPS mixed micelles was determined in the absence of any additional ligand using NMR (Figure 29). Both constructs associate with micelles in a saturable fashion, indicating

they have at least one specific interaction site. This has important implications in the context of PKC maturation. Immature PKC protein has been reported to bind to membranes in the absence of second messengers, before becoming the phosphorylated mature form.[117] It is possible that one or both C1 domains supply a membrane interaction site.

The change in NMR chemical shifts that occur upon micelle titration were used to determine the micelle affinity. While C1Bβ was reported to bind to phosphatidylglycerol (PG) containing lipids with ~100 mM K_d,[10] the affinity of a C1 domain to the native anionic head group, PS, has not been measured. Here, the K_d measured using the loop residues in C1Bδ construct is significantly tighter for DPC/DPS micelles (< 10 mM). Because the number of detergent molecules per micelle is not known for this system, this K_d is determined from a fit using detergent concentration as the ligand. Once the number of molecules per micelles is available, this K_d will be much lower (likely 1-2 orders of magnitude).[113] However, in both cases, 1) PG containing lipids and 2) PS containing detergent micelles, the affinity is much weaker than in the presence of ligand (DAG or phorbol ester). From the C1Bα72 titration with P13A, it is clear that the affinity for ligand in the absence of micelles is also weak (0.6 mM). Together, these data point to the synergy of ligand *and* micelle binding to produce a stable complex capable of activating PKC.

Both the loop and helix residue K_d's were tighter in C1Bδ than W252Y by at least 2- to 3-fold. While this difference in micelle affinity is smaller than the difference in DAG affinity between C1Bδ and W252Y (> 30-fold as described in Chapter II), the

higher affinity for a ligand-free lipid environment where C1B is then restricted to a two-dimensional search for the ligand as proposed from analysis of the C1 binding kinetics,[86] could contribute to the higher DAG sensitivity seen in constructs containing Trp at position 22. This idea is supported by the finding that the C1Bδ W252G mutant, which still binds phorbol ester, is unable to bind to lipid bilayers containing phorbol ester.[101]

For both constructs, the loop residues fit with a K_d significantly tighter than residues in the helix. Because the residues all fit well to a single-site binding equation, one explanation is a single C1 molecule can bind to more than one micelle. This scenario is unlikely due to steric hindrance from the close proximity of the loop and helix residues. In addition, the line widths of the residues that do not shift upon binding micelles broaden significantly in response to the first binding event and then do not show a second broadening event. Because line widths report on the rate of the complex tumbling in solution, this indicates the tighter K_d site for the loop residues is the only micelle binding event. This also makes it unlikely that the micelle changes size or shape significantly due to the increase in detergent concentration, or this too would be reported in broadening of the line widths.

The best explanation for the second binding event involving the α-helix residues is that C1 bound to micelles recruits DPS from the unbound micelles at increasing concentrations of detergent. Specifically, this process must occur through DPS equilibrium between micelle-bound and free in solution, and the free DPS with the C1-micelle complex, in order for the line widths to remain the same during the second binding event. Little is known about the nature of DPC/DPS micelles and their critical

micelle concentration, so it is difficult to comment on how likely these equilibria are in solution. However, given the line widths report only one micelle binding event, the binding data fit to two separate single-site binding events (Figure 29), DPS appears to bind the residues which fit with the second K_d (Figure 31), and the helix residues bind but are not deeply inserted in the micelle (Figure 32), DPS redistribution to C1-bound micelles from micelles in excess of C1 fits all the available data.

Even though all PKC isoforms are activated by PS and PS specificity is thought to be conferred by the C1 domain in several isoforms, this is the first report of a specific PS binding site in C1.[104] The C1Bδ residues that respond the most to DPS incorporation, His270 and Lys271, have a similar identity to those seen in other PS binding sites.[113] These residues correspond to Lys141 and Gln142 in C1Bα, which also shift due to binding DPC/DPS micelles in the Y123W mutant (Figure 23). In all C1 domains found in conventional and novel PKC isoforms, there are positively charged residues in at least one of these two positions, and many have a positive residue at both positions (Figure 3). Consecutive positive residues has been identified as a common PS binding motif in proteins not related to PKC.[118] However, when comparing the C1 domains that bind specifically to PS to the ones that bind equally as well to any negatively charged phospholipid, there is not a clear trend in variability of the residues at this position. Future studies similar to the ones reported here using C1 domains from other isoforms along with mutagenesis will be useful for determining which residues confer PS specificity.

An NMR investigation of conventional C1Bα and its position 22 mutant, Y123W, points to the Trp containing construct having a more extensive interface with ligand-free mixed micelles (Figure 23). However, the binding was intermediate on the chemical shift timescale, so the affinity and depth of insertion could not be determined. Since C1Bδ is in the fast exchange regime for most residues, the effect of position 22 identity on the depth of micelle insertion can be measured. This was assessed by comparing the PRE due to proximity to a PC lipid tagged with doxyl on the 14th tail position that is incorporated into the mixed micelles. The pattern of insertion is similar overall for the observable residues, but four residues on the opposite side of the protein from position 22 are significantly more inserted in the Trp construct (Figure 32A). This likely represents a difference in orientation in the ligand-free micelles due to position 22 identity. *In vivo*, Trp at position 22 could orient the membrane-bound C1 domain in a position that is more favorable for DAG binding once it is encountered in the membranes.

However, once the domains bind to DOG the opposite trend is seen in insertion for four loop residues, including the residue at position 22 (Figure 32B). This is consistent with what is seen for C1Bα constructs when comparing micelle only binding in Figure 23 with DOG saturation in the presence of micelles in Figure 8. In C1Bα fewer residues are affected by micelles in the absence of DOG than in the presence, while Y123W has more residues which are affected by micelle binding in the absence of DOG than in the presence. This change in domain orientation that occurs due to DOG binding could signal release of the neighboring regulatory domains in order to activate

PKC. This type of signaling event was reported for a multi-domain membrane-binding protein which changes orientation upon binding the lipid second messenger phosphatidylinositol 4,5-bisphosphate.[119]

These studies also provide information to separate residues which are responsible for ligand binding from those responsible for micelle binding. This can be seen in Figure 32, where the α-helix residues and ligand hinge regions are deeper inserted in micelles before ligand binding. Chemical shift perturbation analysis of C1Bδ residues bound to micelles compared to DOG binding in the presence of micelles revealed that almost all of the perturbation of the residues in these regions occurs due to interactions with the micelles (Figure 14 and Figure 30). Both experiments indicate the loop hinges experience an environmental change due to micelle binding, rather than binding to DOG.

While it was not possible to directly assess differences between micelle-bound and ligand-bound states in C1Bα, a similar result was seen in the comparison of the chemical shift perturbation of C1Bα bound to phorbol esters in the presence and absence of micelles (Figure 25). In this case, the residues in the hinge regions shifted less than 20% when binding P13A as compared to PDBu in micelles. While some of this difference may be due to the hydrophobic tails found in PDBu (Figure 27), micelle binding still had a significantly larger effect on the hinge region than ligand binding alone.

Why do the hinge regions respond more to micelle binding than to binding DOG or phorbol ester? The ligand hinge region forms a series of hydrogen bonds seen in the C1Bδ crystal structure. As described in Chapter II, I propose these hydrogen bonds

stabilize the closed loop conformation competent for ligand binding. One possible explanation for the behavior observed here is that micelle binding also stabilizes the hydrogen bonds, selecting for the conformation more competent for DOG binding. This theory would be consistent with changes in amide chemical shifts for residues that are involved in hydrogen bond formation. However, because the conformational exchange is still seen in the presence of micelles for both constructs (Figure 23 and Figure 30), it is clear ligand binding is necessary to lock the protein in one conformation.

A second possibility is that the hinge regions interact with the polar ligand head groups. This theory is supported by the ^{15}N NOESY experiments, which revealed strong cross-peaks between loop hinge residues in C1Bα and atoms in detergent head groups (Figure 28) as well as in the changes in chemical shift seen in the β34 loop hinges of C1Bδ in response to DPS incorporation (Figure 31). If this is the case, determining the structure of C1B bound to ligand in a hydrophobic environment will be important for elucidating these specific interactions. In addition to the conclusions drawn here, the chemical shifts, PRE, and NOESY results presented provide valuable information that can be used directly as secondary structure and distance restraints for determining the ligand-bound structure of C1B. These will be discussed in more detail in Chapter V.

CHAPTER IV

ROLE OF CYS151 IN C1B REACTIVITY*

Background

In addition to the C1 domain's regulation of PKC via second messengers and membrane targeting, it also has been implicated in activation of PKC by reactive oxygen species. PKC activation by H_2O_2, in the absence of second messengers, was found to occur from modification of the regulatory domain.[120] Other studies narrowed down the modification to the C1 domain when they found that treatment of PKC with either superoxide[121] or H_2O_2[122] resulted in zinc release. These properties give PKC the ability to both sense and transmit signals based on the redox environment in the cell.[123] However, the manner in which PKC is activated by reactive oxygen species is still unknown.

Several zinc finger proteins have been implicated as redox-switches. Inactive Hsp33 exists with zinc coordinated to 4 cysteine residues under normal cellular conditions.[124] Upon oxidation, zinc is released and the cysteines form two disulfide bonds, leading to the zinc-binding domain unfolding and activation of Hsp33 which functions to defend the bacterial cell from oxidative damage.[125] Under normal cellular conditions the anti-sigma factors, RsrA and ChrR, bind to and inactivate sigma

---

* Parts of this chapter are reprinted with permission from Stewart MD & Igumenova TI (2012) Reactive cysteine in the structural Zn2+ site of the C1B domain from PKCα. Biochemistry 51: 7263–7277. Copyright 2012 American Chemical Society.

transcription factors. Upon oxidation, the anti-sigma factors form at least one disulfide bond, releasing zinc and sigma, allowing sigma to increase transcription of oxidative damage proteins.[126,127] Similarly, Keap1, a mammalian zinc binding protein holds Nrf2 in the cytosol until activated by stress inducers. Once activated, Keap1 releases zinc and Nrf2 allowing Nrf2 to translocate to the nucleus and activate the antioxidant response element.[128]

Through the work in this study, a similar type of mechanism for PKC activation by reactive oxygen species is proposed. H_2O_2 or iodoacetamide (IAC) treatment of C1B or the construct that contains C1B and the following C2 regulatory domain (C1B-C2) led to zinc loss and selective unfolding of the C1B domain. However, when the Zn(2) coordinating Cys151 was mutated to glycine (C151G), the construct reacted slower to H_2O_2 or IAC treatment. Only C1B and C1B-C2, which contain Cys151, reacted in an assay for solvent exposed cysteines. Together, the data point to modification of C1B cysteines, with the most reactive cysteine being Cys151, causing zinc release and domain unfolding. The loss of structure in the C1 domain could then lead to the loss of the auto inhibitory properties of the regulatory domain, thus PKC activation.

Consistent with the reactivity and solvent exposure assays, NMR revealed C1B exchanges between a conformation in which Cys151 is solvent exposed and easily accessible to reactive oxygen species, and the conformation in which it is coordinated to zinc. First, HSQC spectra of C1B revealed several residues surrounding Zn(2) site existed in two conformations, with the largest chemical shift difference for Cys151. ZZ-exchange NMR was used to calculate the rate of exchange between the two conformers

of about 3 per second with an activation energy of 70 kJ at pH 5.7 and 25˚C. Lowering the pH or mutating Cys151 to glycine eliminated the zinc coordinated population, while an increase in pH favored the zinc coordinated population. Finally, residual dipolar couplings were used to refine the structures of both protein conformations revealing the first structure of a C1 domain in which Cys151 is not zinc coordinated, leaving it more accessible to reactive oxygen species.

Methods

Protein over-expression and purification

The *E. coli* codon-optimized DNA sequence of C1Bα domain from *Mus musculus* coding for a 50-residue construct of C1Bα, comprising residues H102 through Cys151 of PKCα, was cloned into a pET-SUMO expression vector (Invitrogen) as a C-terminal fusion with histidine-tagged SUMO.[129] This construct will be referred to as C1Bα50. Mutagenic DNA for the C151G mutant was constructed from the wild-type C1Bα50 gene in the pET-SUMO vector using a Stratagene QuickChange™ site-directed mutagenesis kit and suitable PCR primers. The DNA sequence coding for a 194-residue construct encompassing the C1B-C2 domain (Ser99 - Gly292) from *Mus musculus* were amplified by PCR using the PKCα cDNA clone (Open Biosystems) as a template. These constructs were cloned into the pET-SUMO vector as above. Purified plasmids of all the constructs were transformed into BL21(DE3) *E.coli* cells for protein over-expression and purification.

The isolated C2 domain was expressed and purified as described previously.[130] C1B-C2 was purified using the C2 purification protocol with minor modifications.

Preparation of C1Bα50 and the C151G mutant differed slightly from the C1Bα53 purification described in chapter I. The fusion protein was purified using a HisTrap™ HP Ni affinity column (GE Healthcare Life Sciences). The fractions containing fusion protein were pooled and SUMO was cleaved from C1Bα50 or C151G at 25 °C using SUMO protease. The products of SUMO protease cleavage reaction were separated by gel-filtration using HiPrep 16/60 Sephacryl S-100 column (GE Healthcare Life Sciences) in 50 mM MES pH 6.5 and 150 mM KCl. For NMR experiments, unless otherwise stated, the protein was concentrated to ~0.5 mM, and exchanged in the buffer containing 10 mM [^{2}H-4]-imidazole at pH 6.5 (Cambridge Isotopes), 150 mM KCl, 8% ^2H_2O, 1 mM tris(2-carboxyethyl)phosphine (TCEP), and 0.02% NaN_3. The purity of all constructs was assessed using SDS-PAGE.

Resonance assignments

C1Bα50 ^{1}H, ^{13}Cα, ^{13}Cβ, and ^{15}N resonances were assigned from gradient-enhanced CBCA(CO)NH, HNCACB, and C(CO)NH 3D NMR spectra[61] obtained on a 600 MHz Varian Inova spectrometer at 25°C. Assignment experiments were carried out on a uniformly ^{15}N and ^{13}C enriched 0.5 mM sample in the above mentioned buffer at pH 6.5 or pH 5.7. The $H^{\delta 2}$ protons of histidine side-chains were assigned using the 2D (HB)CB(CGCD)HD experiment.[131] C151G mutant assignments were transferred from wild-type. The residue-specific differences in chemical shifts between the C1Bα50 conformers were calculated according to the following equation:[62]

Equation 11 $\Delta = [\Delta\delta H^2 + (0.152\Delta\delta N)^2 + (0.152\Delta\delta C_\alpha)^2 + (0.152\Delta\delta C_\beta)^2]^{1/2}$

where $\Delta\delta H$, $\Delta\delta N$, $\Delta\delta C_\alpha$, and $\Delta\delta C_\beta$ are the chemical shift differences between the ^1H_N, ^{15}N, $^{13}C_\alpha$, and $^{13}C_\beta$ nuclei, respectively. All NMR data was processed using NMRDraw 3.0[59] and assigned using Sparky 3.133.[132] For all NMR experiments the temperature was calibrated using methanol below 30°C and ethylene glycol above 30°C.

Exchange kinetics

The kinetics of the two populations in slow exchange for the uniformly ^{15}N enriched C1Bα50 was measured using a NMR ZZ-exchange experiment.[133] Peak volume analysis was carried out using a peak integration function for NMRDraw.[59] The time dependence ($\Xi(t)$) of the ratio of auto (a_{AA} and a_{BB}) and exchange (a_{AB} and a_{BA}) peak volumes:[134]

$$\Xi(t) = \frac{a_{AB}(t)a_{BA}(t)}{a_{AA}(t)a_{BB}(t) - a_{AB}(t)a_{BA}(t)} \cong \zeta t^2$$

Equation 12

was globally fit with IGOR as a quadratic coefficient (ζ) using 6 well resolved residues (103,104 133,147,149,and 151). Residue 149 was not used at 30˚C due to unresolved cross-peaks and autopeaks. Residue 103 experienced severe peak broadening at low temperatures and therefore it was not used in calculations between 10 and 20˚C. The experiments were carried out at 5 temperatures: 9.4, 15.0, 19.8, 25.0 and 30.2 °C. Residue-specific Ξ values were plotted as a function of mixing time and fitted to the following equation:

$$\Xi(t) = k_1 k_{-1}^{'} t^2$$

Equation 13

where k_1 and k_{-1}' are the forward and pseudo-first order reverse rate constants for the exchange reaction between *a* and *b*. The data for all residues were fitted globally to obtain the product of two rate constants, $k_1 k_{-1}'$.

The apparent equilibrium constant for the exchange reaction was defined as K_{app} = [*b*]/[*a*]. K_{app} was determined using an average of the ratio of the peak volumes from the two populations for 9 well-resolved residues (103, 131, 133, 134, 140, 145, 147, 149, and 151) in fully relaxed ^{15}N-^{1}H HSQC spectra collected with the 5 s relaxation delay. The kinetic rate constants were then calculated using the $k_1 k_{-1}'$ and k_1/k_{-1}' values obtained from the ZZ-exchange data and K_{app}, respectively. The activation enthalpies and entropies for the forward and reverse reactions were determined from fitting the data with the Eyring equation:

Equation 14 $$k = (k_B T\kappa / h) e^{\Delta S''/R} e^{\Delta H''/RT}$$

where *k* is the rate constant for the reaction; k_B is the Boltzmann constant; κ is the transmission coefficient assumed to be 1 in most types of analyses; *h* is the Planck constant; and $\Delta S^{\neq}$ and $\Delta H^{\neq}$ are the entropy and enthalpy of activation, respectively. Activation energies, E_a, were obtained from fitting the data with the Arrhenius equation:

Equation 15 $$k = A e^{-E_a/RT}$$

where *A* is the pre-exponential factor.

Probing for C1B reactivity

[U-^{15}N]-enriched C1Bα50, C151G, C1B-C2, and isolated C2 domains were treated with H_2O_2 solution to probe their response to reactive oxygen species. HSQC

experiments collected every 1-1.5 hours starting approximately 0.5 hours after addition of H_2O_2 to a final concentration of 1.25 mM. To ensure comparable signal-to-noise ratios in the NMR spectra, the protein concentration varied with the length of the protein construct: 0.1 mM C1Bα50 or C151G, 0.15 mM C2, and 0.25 mM C1B-C2. To quantify the rate of signal decay, the cross-peak intensities were plotted against the time elapsed from addition of H_2O_2 to the mid-point of each HSQC collected until ~20% of cross-peak intensity remained. The data were fit to an exponential decay using the Curvefit software available from Dr. Arthur G. Palmer's laboratory at Columbia University (http://www.palmer.hs.columbia.edu/software/curvefit.html). After the cross-peak intensities decayed to less than 10% of their original cross-peak intensity, the amount of Zn^{2+} released into solution was quantified spectroscopically using 4-(2-pyridylazo)-resorcinol (PAR) (Fisher Scientific).[135]

To determine the Zn^{2+} content of the intact C1Bα50, C151G, and C1B-C2 constructs, the protein solution was diluted to 2-5 μM in 4 mM H_2O_2 (VWR International) and 50 mM Tris buffer (pH 7.5) that was previously ran over the Chelex-100 resin (Sigma) to remove trace metal ions. This solution was incubated at 42 ºC for 50 minutes then cooled to room temperature. PAR was added to a final concentration of 0.1 mM. The increase in absorbance at 500 nm was measured and compared to that of the control sample treated identically but lacking the protein solute. The zinc content was quantified using a standard calibration curve (1-12 μM Zn^{2+} concentration range) under buffer conditions identical to those used for protein samples. Each measurement was repeated at least three times. The results showed that C1Bα50, C151G, and C1B-

C2 released 1.8 ± 0.1, 2.0 ± 0.1, and 2.2 ± 0.1 molar equivalents of zinc, respectively. This is in agreement with the results obtained on the MBP-C1Bα fusion protein, which released two molar equivalents of zinc when treated with H_2O_2.[136] The results also demonstrate that coordination to Zn(2) is maintained in C151G throughout purification despite the loss of Cys151Sγ-Zn(2) bond.

To establish if Zn^{2+} is released by C1B upon H_2O_2 treatment at 25 ºC, PAR assays were carried out on the supernatants of NMR samples treated with H_2O_2. After the intensity of the NMR signals had decayed to less than 10% of the original, the supernatant was removed and diluted into the above Tris buffer and 0.1 mM PAR. No additional H_2O_2 was added. The protein concentration was varied such that the zinc released was 3-12 μM to be within the range of the standard calibration curve. The calibration curve samples consisted of 1-12 μM Zn^{2+} standard solution, the same volume of NMR buffer as the supernatant assays, Tris buffer, and 0.1 mM PAR. After dilution, all the samples were equilibrated for five minutes at room temperature before measuring the absorbance at 500 nm.

Mass-tagging of C1Bα50 (50 μM), C151G (35 μM), and C1B-C2 (10 μM) was accomplished by incubation with 0.25 mM polyethylene glycol maleimide 5,000 (PEG-mal, NANOCS) at room temperature for 5 hours in a buffer containing 10 mM imidazole at pH 6.5, 150 mM KCl, and 1 mM TCEP. In addition, either 0.1 mM Ca^{2+} or 0.1 mM ethylenediaminetetraacetic (EDTA) was added to two of the C1B-C2 samples. After 5 hours, the reactions were quenched by the addition of 50 mM dithiothreitol (DTT) and incubation at room temperature for 15 minutes.[137] The samples were subsequently

boiled for 5 minutes in an equivalent volume of 2X SDS-PAGE loading buffer (BioRad) and loaded onto a 15% SDS-PAGE. All chemicals were obtained from Fisher Scientific unless otherwise stated.

To alkylate the reactive cysteines, [U-^{15}N]-enriched C1Bα50, C151G, and C1B-C2 were treated with IAC at 10 times the cysteine concentration for one hour in the dark at room temperature before quenching the reaction with dithiothreitol. The final concentration of IAC in the NMR samples was 6, 6, and 12 mM for the C1Bα50, C151G, and C1B-C2 constructs, respectively. HSQC experiments were recorded to evaluate the state of the protein samples.

Determining pKa values

^{15}N uniformly enriched C1Bα50 in the above mentioned NMR buffer was titrated between pH 5 and 8.5 using concentrated HCl and NaOH. Similarly, ^{15}N uniformly enriched C151G mutant and C1Bα53 were titrated between pH 5 and 8.25 except without the presence of buffer. The pKa values were the same within error regardless of the construct or presence of buffer. The pH was measured with an accumet AB15 pH meter from Fisher Scientific with a Hamilton biotrode electrode before and after each NMR experiment and the pH values were averaged if they differed. The values are not corrected for the 8% D_20. The chemical shift of ^{15}N - ^{1}H backbone and aromatic side-chain resonances at varying pH were monitored by HSQC and fHSQC[106] respectively on a 600 MHz Varian Inova at 25°C.

The dependence on pH of residue-specific ^{15}N or $^{1}H_N$ chemical shifts, whichever was larger, was fit to a modified Henderson-Hasselbach equation:[138]

$$\delta = offset + \frac{delta}{1+10^{pH-pKa1}} \quad \textbf{Equation 16}$$

where δ is the observed chemical shift at a given pH, *offset* is the chemical shift offset, and *delta* is the chemical shift change in the titration process with the acid dissociation constant Ka1. The chemical shifts of residues that responded to two titration events were fit to the following equation:

$$\delta = offset + \frac{delta_1}{1+10^{pH-pKa1}} + \frac{delta_2}{1+10^{pH-pKa2}} \quad \textbf{Equation 17}$$

where 1 and 2 designate the parameters associated with the first and second ionization events.

The pH dependence of the populations was determined by integrating the area under the peaks using Sparky. Then the fraction of a given population at each pH was calculated for each residue by dividing the intensity of each peak (*a* or *b*) by the sum of the intensities of both populations (*a*+*b*). The fraction in either population *a* or *b* (F_a or F_b) were globally fit using IGOR to the following equations:

$$f_a = 1/(1+10^{pH-pKa_{app}}) \quad \textbf{Equation 18}$$

$$f_b = 1 - f_a \quad \textbf{Equation 19}$$

where the pKa_{app} is the apparent pKa of Cys151.

Dynamics measurements

The R_1, R_2, and NOE relaxation rate constants were collected and analyzed as described in Chapter II.

Structure determination with residual dipolar couplings

Partially aligned samples of C1Bα50 were made in stretched or compressed 7% polyacrylamide gels. The stretched gels, composed of 7% acrylamide with 37.5:1 bis-acrylamide (BIORAD), 0.1% w/v ammonium persulfate (Fisher Scientific) and 0.08% v/v N,N,N',N'-Tetramethylethylenediamine (Fisher Scientific), were cast at a diameter of 6 mm. The gel was removed from the cast and washed in water for at least 3 hours. The gels were then dried overnight on a parafilm support. The dried gel was placed back into the 6 mm chamber and soaked overnight with 0.5 mM protein. The soaked gel was stretched into a 4.2 mm NMR tube using a tube and apparatus[78] obtained from New-Era to reach a 0.7 stretch ratio. The compressed gels were made and treated in the same way except the cross-linker ratio was 20:1 acrylamide:bis-acrylamide and the gel cast was 3.2 mm internal diameter. The 25 mm length dried gel was placed into a 4.2 mm diameter shighemi tube with 0.5 mM protein and the plunger was placed so that the gel expanded to a length of 17.5 mm for a compression ratio of 0.7.

All RDC experiments were performed on a 600 MHz Varian Inova at 25°C for an isotropic sample and the partially aligned samples. In phase anti-phase (IPAP)[79] HSQC spectra were collected for 15.2 hours with 512 complex points in the indirect dimension. ^{1}H was apodized with a cosine-bell window function and zero filled to 2K points. 64 points were added to the indirect dimension by forward backward linear

prediction, followed by apodization with a cosine-bell window function and zero filling to 1K points. HNCOCA spectra were collected in an IPAP manner for 98 hours with 64 complex points in the ^{15}N dimension and 140 complex points in the ^{13}C dimension. Spectra were processed as reported previously.[139]

134 RDC values obtained from population *b* and residues not undergoing conformational exchange in stretched and compressed gel samples were utilized to refine the Cys151 coordinated C1B structure with the simulated annealing protocol described previously[140] in XPLOR.[141] The starting structure for refinement was the recently deposited NMR structure of PKCα C1B (PDB ID 2ELI).[142] This structure was determined from NOEs present at pH 7.0 where greater than 90% of the protein is in the Cys151 coordinated conformation, thus it should be very close to the RDC refined structure. The first structure of the 2ELI conformational ensemble was taken as a starting model. All RDC values were scaled to $^{1}D_{NH}$ to take into account the differences in bond lengths and gyromagnetic ratios of the nuclei involved. In addition, the force constants used for different RDC types were scaled to the $^{1}D_{NH}$ force constant according to the inverse of the relative experimental error ratios squared. These calculations resulted in the following scaling factors for the force constants: $^{1}D_{NH}$=1 (by default), $^{1}D_{C\alpha H\alpha}$=2.104, $^{1}D_{NCO}$= 0.238, and $^{2}D_{HNCO}$= 0.151. The (ϕ, ψ) dihedral angles and 80 long range NOEs from the 2ELI NMR restraint deposit file in the PDB were used as additional restraints. Long-range NOEs were defined as those separated in primary structure by two or more residues, and were only used if both residues *did not* have significantly different RDC values or chemical shifts in the two conformations.

Additionally, 6 backbone hydrogen-bonds were identified using WHATIF[87] and used in refinement. The zinc coordination restraints differed for conformers *a* and *b*. For C1Bα50*b*, the distances from the zinc atoms to the coordinating atoms were restrained to 2.3 Å and 2.5 Å for nitrogen and sulfur, respectively, in tetrahedral coordination geometry. For C1Bα50*a*, the distance and angles involving the S_γ of Cys151 in the zinc coordination sphere were not restrained due to the thiolate protonation at low pH. All other zinc-coordinating residues were restrained with the same distances and geometry as for conformation *b*. Because TALOS dihedral angle predictions for residues with different RDC values in conformers *a* and *b* did not make a significant difference in the final structure of *a*, the NMR structure-derived angles were used for the first step of the refinement.

The overall refinement protocol was as reported by Chou and Bax with minor modifications.[140] The parameters are summarized in Table 4. The axial (D_a) and rhombic (R_h) components of the alignment tensor were allowed to vary during the minimization steps. Two high-temperature and one low-temperature simulated annealing steps were carried out. The final values for the tensor components were: D_a=7.78(8.06) and R_h=0.54(0.49) for conformer *b*(*a*) in a compressed gel, and D_a=-22.6(-22.0) and R_h=0.53(0.55) for conformer *b*(*a*) in a stretched gel. The reported structures of *a* and *b* are the regularized average structures determined using the top 5% of the 50 lowest-energy structures obtained in the final refinement step.

The average of the best 10% of structures determined above of the Cys151 coordinated conformation was used as a starting structure for refinement of the Cys151

solvent exposed structure with the 130 RDC values for population *a* and residues not undergoing conformational exchange. The same procedure as above was used for refinement. Starting dihedral angle restraints were chosen to match the starting structure except where TALOS[143] predictions using the chemical shifts of $^{1}H_{N}$, ^{15}N, $^{13}C\alpha$, and $^{13}C\beta$ for population *a* differed by more than 30 degrees, then the TALOS predictions were used as described previously for refinement of liganded versus apo calmodulin.[140] All images of structures were created using Chimera.[144]

Table 4. Parameters of the simulated annealing protocol.

Restraint Type or Parameter	High Temperature Refinement	Low Temperature Refinement
Temperature	200 → 20 K, ΔT = 10 K	20 K → 1 K, ΔT = 1 K
Dihedral angles (φ and ψ)	200 kcal mol^{-1} rad^{-2}	200 → 50 kcal mol^{-1} rad^{-2}
RDCs (Normalized to $^{1}D_{NH}$)	0.0005 → 1.0 kcal mol^{-1} Hz^{-2}	1.0 kcal mol^{-1} Hz^{-2}
Radius of gyration	50 kcal mol^{-1} $Å^{-2}$	50 kcal mol^{-1} $Å^{-2}$
Hydrogen bonds	2 → 20 kcal mol^{-1} $Å^{-2}$	20 kcal mol^{-1} $Å^{-2}$
Ramachandran potential	0.02 → 0.2 unitless	0.2 unitless
Van der Waals radius	0.002 → 4.0 kcal mol^{-1} $Å^{-4}$	4.0 kcal mol^{-1} $Å^{-4}$
Improper angles	0.1 → 1.0 kcal mol^{-1} deg^{-2}	1.0 kcal mol^{-1} deg^{-2}
Bond angles	0.4 → 1.0 kcal mol^{-1} deg^{-2}	1.0 kcal mol^{-1} deg^{-2}
Long-range NOEs	2.0 → 20 kcal mol^{-1} $Å^{-2}$	20 kcal mol^{-1} $Å^{-2}$
Pre-annealing dynamics	10 ps at 200 K, 0.2 K tolerance	10 ps at 20 K, 0.02 K tolerance
Time per temperature step	5.0 ps	5.0 ps

Results

Cys151 is reactive irrespective of the protein context

C1Bα50 corresponds to the minimum folded core of the C1B domain, in which the side-chains of the first (His102) and last (Cys151) residues are involved in Zn(2) coordination. C151G variant has Cys151 mutated to the Gly residue. The primary structure and zinc coordinating residues for these two constructs are shown in Figure 33. The rationale behind constructing this variant was two-fold: (i) to gain insight into the relative reactivity of cysteine residues in C1B, and (ii) to eliminate the coordination bond between Zn(2) and Cys151. This mutation preserves the overall fold of C1B, according to the NMR data discussed below. The C1B-C2 construct (see Figure 2) is 194 amino acids long and comprises both the C1B and C2 domains of PKCα. The C2 domain is a Ca^{2+}-responsive peripheral membrane domain lacking native cysteines. Having the C2 domain in this construct mimics the protein context of C1B in the full-length PKCα.

Figure 33. Primary structures of the two 50 residue C1Bα constructs. The mutation site is highlighted in yellow; zinc-coordinating residues are highlighted in cyan; the loop residues are underlined.

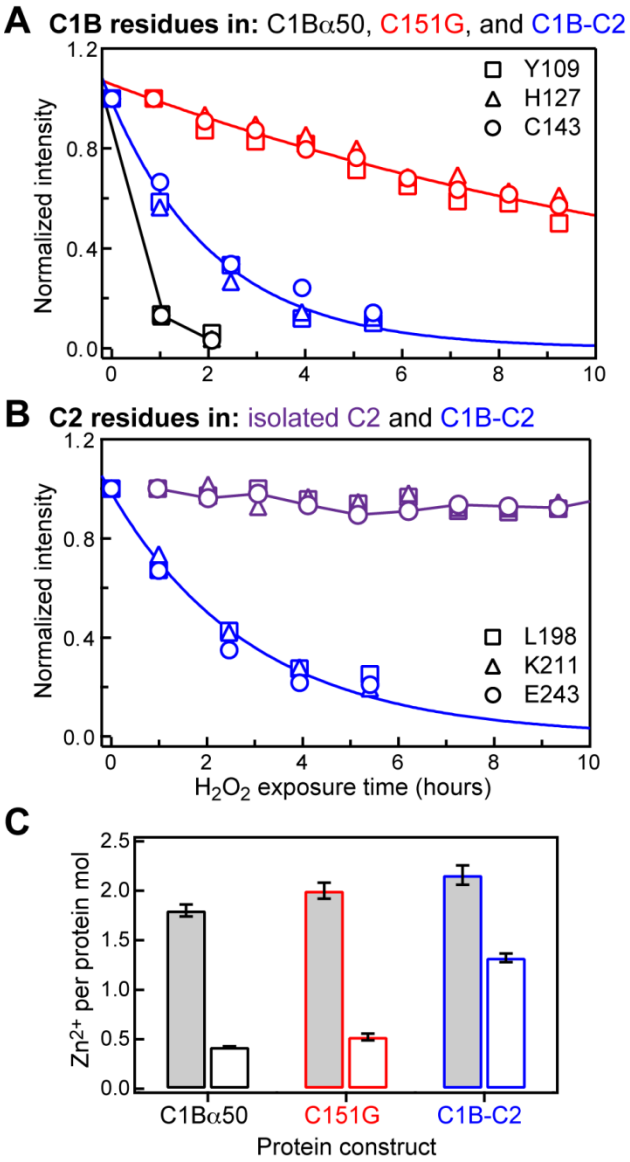

Figure 34. H_2O_2 treatment of C1B-containing proteins results in the loss of native structure. (A) Representative data for three C1B residues in C1Bα50 (black), C151G (red), and C1B-C2 (blue). (B) Representative data for three C2 residues in isolated C2 (purple) and C1B-C2 (blue). Curves represent the exponential fits to the C151G and C1B-C2 data; C1Bα50 and C2 points are connected with lines for illustration purposes. (C) The number of Zn^{2+} ions released per protein molecule in solution when treated with 1.25 mM H_2O_2 at 25 ºC until 10% NMR cross-peak intensity remained (open bars) and with 4 mM H_2O_2 at 42 ºC for one hour (shaded bars).

To oxidize the reactive cysteine(s), all three constructs were treated with 1.25 mM hydrogen peroxide. As a negative control, the isolated Ca^{2+}-complexed C2 domain that lacks native cysteine residues was also treated. The progress of the protein reactions with H_2O_2 was monitored by NMR. For all C1B-containing constructs, the H_2O_2 treatment resulted in the gradual disappearance of NMR cross-peaks from the ^{15}N-^{1}H HSQC spectra. Because the solution remains clear for the duration of ~12-24 hour NMR experiments, this phenomenon is attributed to the formation of soluble high-molecular weight aggregates that are unobservable due to slow rotational diffusion and/or aggregation processes that are intermediate on the NMR chemical shift timescale. Figure 34 shows the data for three representative residues that belong either to the C1B (A) or the C2 (B) domains.

It is evident from Figure 34A that the stability of C1B with respect to oxidation by H_2O_2 depends on whether Cys is present at position 151. The signal corresponding to the native population of C1Bα50 decays within 2 hours of initiating the H_2O_2 treatment. However, the C151G variant lacking one coordination bond to Zn(2) (see Figure 33) is more stable, with a quantifiable average signal decay rate of 0.06 hr^{-1}. The residue-specific decay rates are rather uniform throughout C151G, with a standard deviation of 0.01 hr^{-1} (Figure 35). Peroxide treatment of the two-domain construct C1B-C2, where Cys151 immediately precedes the linker region connecting the two domains, results in the average signal decay rate of 0.45 hr^{-1}, about ~8-fold higher than that of the C151G variant. The residue-specific decay rates of C1B-C2 are plotted in Figure 35.

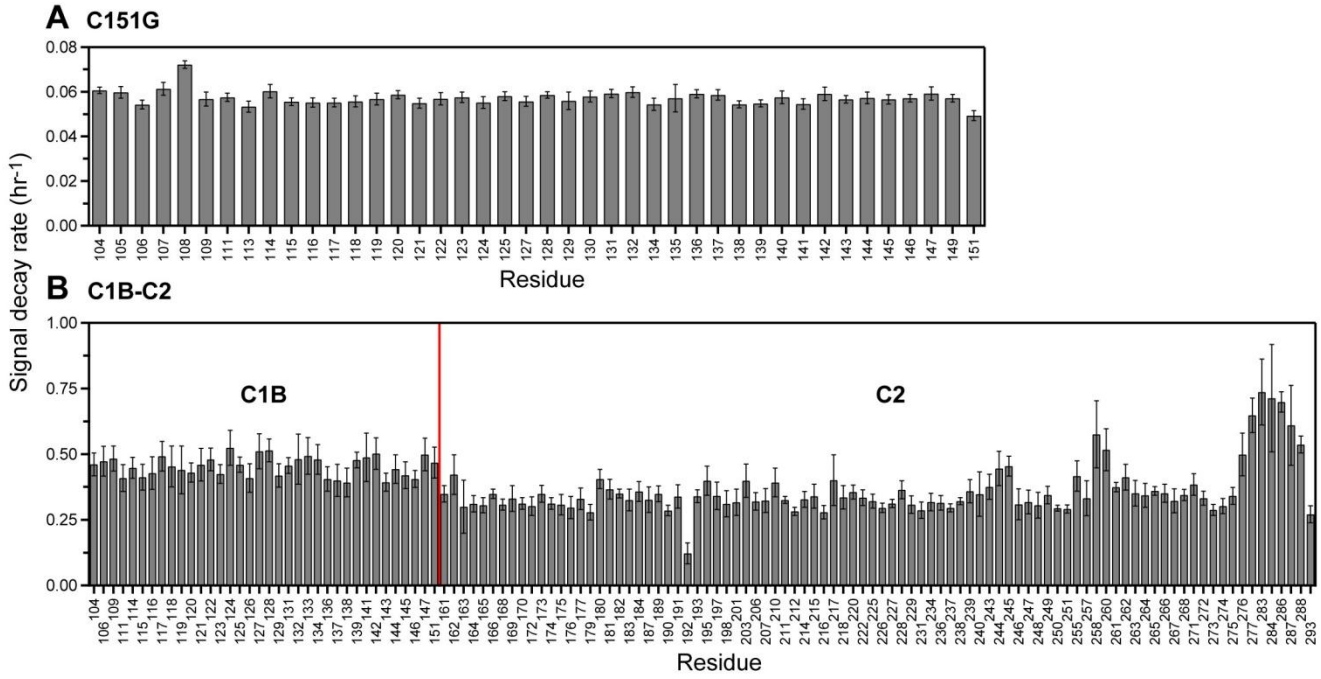

Figure 35. Rates of cross-peak disappearance as a result of H_2O_2 treatment. Constructs treated were (A) C151G and (B) C1B-C2. The red line marks Cys151 in C1B.

Figure 34B shows the results of the negative control experiment carried out on the isolated Ca^{2+}-complexed C2 domain that lacks native cysteine residues. The signal intensity does not change significantly in the course of the NMR experiment indicating that the isolated C2 domain is not susceptible to oxidation by H_2O_2. In contrast, the N-H_N cross-peaks corresponding to the C2 domain in the C1B-C2 construct decay with an average rate of 0.36 hr^{-1}. These data demonstrate that H_2O_2 acts specifically on the cysteine-containing C1B domain, but the resulting aggregation process affects C2 when linked to C1B.

Fully folded C1B-containing constructs including the C151G variant contain two Zn^{2+} ions per protein molecule (Figure 34C, shaded bars). These data were obtained using PAR assay under conditions favoring complete Zn^{2+} release: 1-hour incubation with 4 mM H_2O_2 at 42 °C. PAR assay was also carried out on the supernatants of all H_2O_2-treated NMR samples at 25 °C, with no additional H_2O_2 added to the protein solutions. In all three constructs, a partial release of Zn^{2+} ions from C1B is observed (Figure 34C, open bars).

Given the release of structural Zn^{2+} ions and extensive protein precipitation observed for H_2O_2-treated NMR samples after ~24-48 hours, it can be concluded that the treatment with H_2O_2 results in at least partial loss of the native C1B structure.

To test for cysteine solvent exposure, mass-tagging assays were conducted on C1Bα50, C151G, and C1B-C2. Mass-tagging was accomplished by reacting the proteins with PEG-maleimide (PEG-mal 5,000), as shown in Figure 36A. Covalent modification of each cysteine residue adds 5 kDa of molecular weight. The mass-tagged

protein species are subsequently resolved on the SDS-PAGE gel (Figure 36B), in which the 5 kDa increase in molecular weight manifests itself as an ~8-10 kDa shift on the gel.

C1Bα50 is modified primarily at one cysteine residue (lane 6). C151G is not modified by PEG-mal (lane 8), which means that Cys151 is the most reactive residue in C1Bα50. C1B-C2 shows a "ladder" pattern of one, two, and >3 modified Cys residues, with the primary species being the single Cys-modified protein (lane 2). Addition of Ca^{2+} to C1B-C2 does not influence the "ladder" pattern (lane 3); indicating that Ca^{2+} binding by the C2 domain has little effect on the reactivity of cysteines in the C1B domain. Treating C1B-C2 with EDTA unfolds the protein by removing the structural Zn^{2+} ions. As a result, all cysteine residues become solvent-exposed and modified by PEG-mal with the formation of high molecular weight species (lane 4).

A similar pattern of cysteine reactivity was obtained upon treating the protein constructs with cysteine-specific alkylating agent, IAC. Modification of C1Bα50 by IAC completely unfolded the C1B domain as was evident from the ^{15}N-^{1}H HSQC spectra (Figure 37A). In contrast, the population of the fully folded protein was still present in the C151G variant after the completion of IAC reaction. Treatment of C1B-C2 with IAC selectively unfolded the C1B domain but left the C2 domain unaffected in the C1B-C2 construct (Figure 37B). Similar to H_2O_2 treatment at 25ºC, IAC treatment resulted in partial zinc loss for all of the constructs (1.1-1.9 zinc atoms/ C1B were released into solution). This suggests that while all three protein constructs have one or more reactive cysteines whose alkylation results in the loss of native structure of C1B,

the presence of Cys151 in the protein (C1Bα50 and C1B-C2) makes it more susceptible to such a reaction.

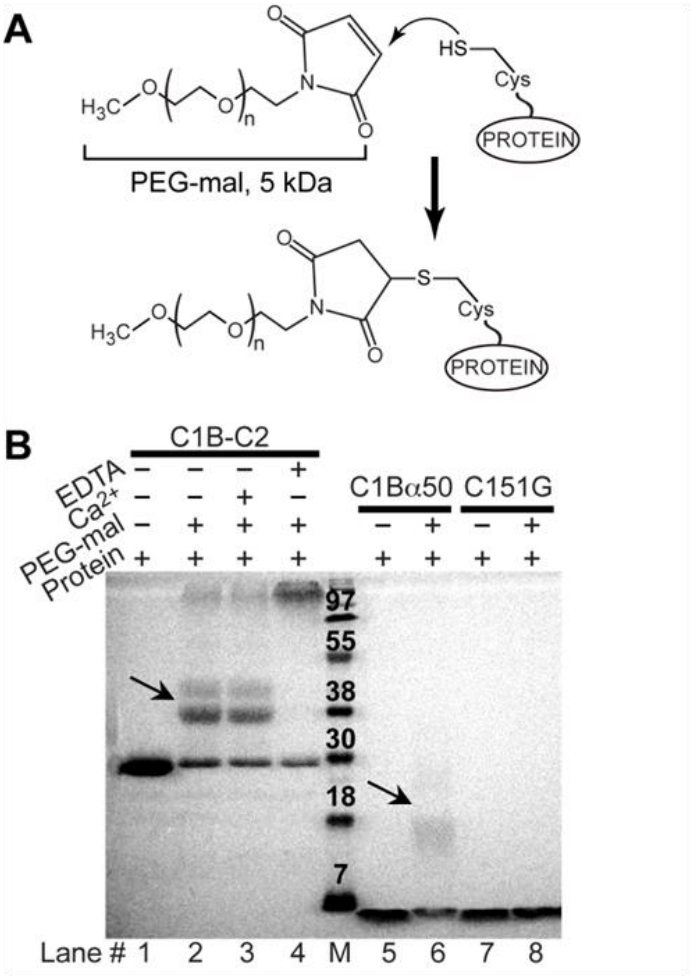

Figure 36. Mass-tagging assays carried out on C1Bα50, C151G, and C1B-C2. (A) Reaction between the sulfhydryl groups of exposed cysteine residues and PEG-mal. (B) SDS-PAGE results of the PEG-mal treatment of three C1Bα constructs. Arrows point to the single-Cys modified species in C1Bα50 and C1B-C2.

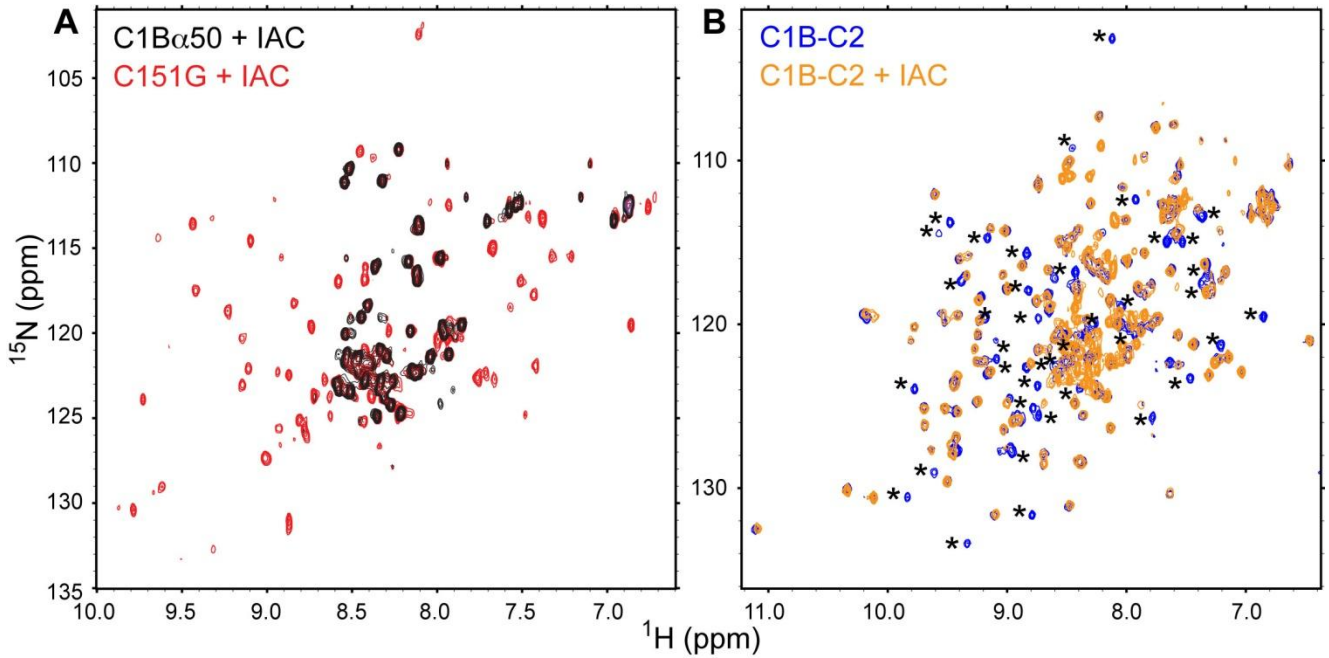

Figure 37. Modification of C1B containing constructs with IAC. (A) Overlay of the ^{15}N-^{1}H HSQC spectra of the IAC-treated C1Bα50 (black) and C151G (red). (B) Overlay of the ^{15}N-^{1}H HSQC spectra of the native (blue) and IAC-treated C1B-C2 (orange). Cross-peaks labeled with asterisks correspond to the C1B domain in the native C1B-C2 construct. Upon IAC treatment, these cross-peaks shift to the central region of the spectrum.

In summary, the oxidation and alkylation data are consistent with Cys151 being the most reactive among the six cysteines in C1Bα. Its covalent modification results in the loss of C1B native structure and subsequent covalent modification of all other cysteines accompanied by partial Zn^{2+} release. C1Bα50 shows unique dynamics of the Zn(2) coordination sphere that includes Cys151. This dynamics was characterized using solution NMR techniques.

C1Bα50 exists in two conformations

The structural and functional cores of C1 domains are formed by 50 amino acid residues.[145] C1Bα50 behaved as a homogeneous protein preparation in all purification steps. However, the ^{15}N-^{1}H HSQC spectrum of the [U-^{15}N]-enriched C1Bα50 showed a larger number of ^{15}N-$^{1}H_N$ cross-peaks than was expected based on the size of the protein construct. Using triple-resonance NMR experiments, sequence-specific assignment of [U-^{13}C,^{15}N]-enriched C1Bα50 was carried out. Out of 48 non-proline residues, 17 gave rise to a pair of N-H_N cross-peaks with distinct chemical shifts. The cross-peak pairs are labeled with the double-headed arrows in the HSQC spectrum of C1Bα50 (Figure 38A**)**. This behavior indicates the presence of two conformations of C1Bα50 that co-exist in solution. The exchange between the conformers is slow on the NMR chemical-shift timescale.

To gain insight into the identity of the exchanging conformers, the chemical shift differences calculated according to Equation 11 are mapped onto the ensemble-averaged NMR structure of C1Bα.[67] The results are shown in Figure 38B. The residues whose electronic environment differs most between the two conformations are located in the

vicinity of the Zn(2) coordination site. Cys151, the most C-terminal residue of the domain, experiences the largest combined chemical shift perturbation with the Δ value of 1.3 ppm. The Sγ atom of the Cys151 side-chain is involved in the coordination bond with Zn(2), according to all known C1 domain structures. However, most of these structures were determined using NMR, which cannot be used to determine zinc coordination directly. The coordination geometry of Zn(2) is shown in Figure 38C.

The C151G variant of C1Bα50 presents only three protein ligands to Zn(2) instead of four. The C151G mutation was shown to preserve the functionality of a homologous C1B domain from PKCδ, as determined by the ability of the domain to bind phorbol esters.[146] In Figure 38A, the HSQC spectrum of the [U-^{15}N]-enriched C151G variant is shown in red and overlaid onto the spectrum of the wild-type protein. It is evident that C151G exists in one conformation only, and this conformation is one of the two sampled by the wild-type C1Bα50. The molar ratio of Zn^{2+} ions to protein is 2 in the C151G variant (Figure 34C), indicating that the protein maintains coordination to Zn(2) despite the loss of the Cys151Sγ–Zn(2) bond.

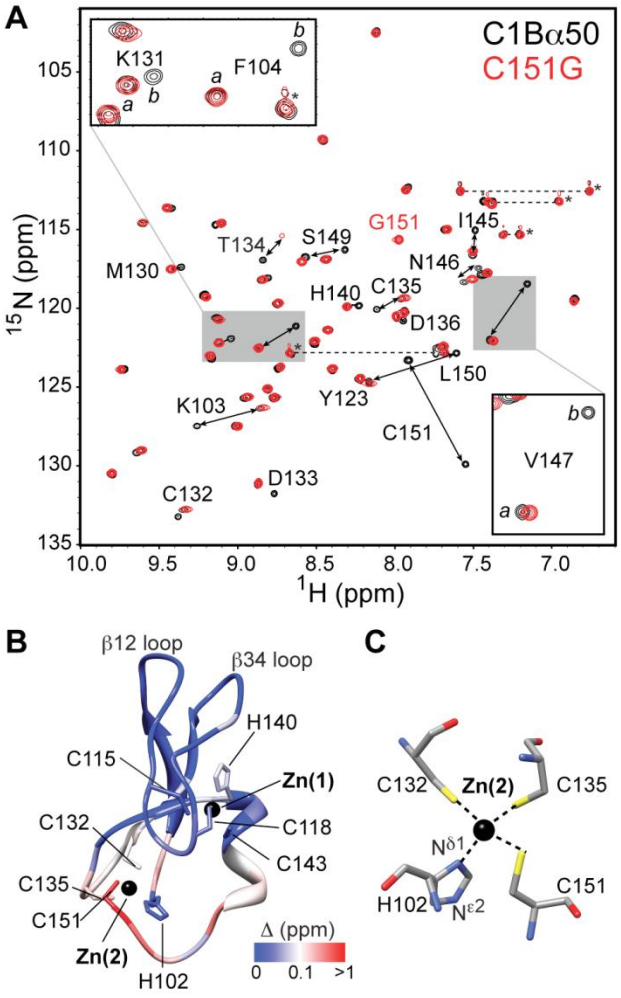

Figure 38. C1Bα50 exists in two slowly exchanging conformations. (A) Overlay of the ^{15}N-^{1}H HSQC spectra of C1Bα50 and C151G variant. The insets show the expansions for Lys131, Phe104, and Val147. (B) Chemical shift perturbation (Δ) mapped onto the structure of C1Bα.[67] The coordinates are the courtesy of Dr. U. Hommel. (C) Coordination geometry of Zn(2) showing four protein ligands.

Based on this set of experiments, it can be concluded that the conformational exchange process in the wild-type C1Bα50 corresponds to Cys151 alternating between Zn(2)-coordinated and uncoordinated states.

The conformational exchange process is modulated by the pKa of the Cys151 side-chain

There were significant changes in the fractional populations of the conformers in the C1Bα50 NMR spectra recorded at two different pH values. To explore the pH dependence systematically ^{15}N-^{1}H HSQC spectra of C1Bα50 were recorded at pH values ranging from 5.0 to 8.5.

For the 17 residues that have distinct cross-peaks in the two conformers of C1Bα50, there was a complete redistribution of conformer populations over the sampled pH range. The low-pH conformer designated *a* for "acidic" conditions is the dominant form at pH < 6; the high-pH conformer designated *b* for "basic" conditions is the dominant form at pH > 6. Conformer *a* corresponds to the uncoordinated Cys151, based on the near-identity between its spectrum and that of the C151G variant (Figure 38A). For several residues, including some from the aforementioned group of 17, there was a pH-dependent shift in their N-H_N cross-peak positions. The shift reflects the titration behavior of the proximal ionizable side-chain(s) and is "fast" on the NMR chemical shift timescale.

Three specific examples illustrating the pH titration behavior of C1Bα50 are shown in Figure 39A**.** All three residues, Phe104, Asp133, and Cys132, have two populations that give rise to distinct cross-peaks. In Asp133, the pH change results

simply in the redistribution of populations *a* and *b*. In Phe104 and Cys132, this process is accompanied by the pH-dependent shift of the conformer *b* cross-peaks.

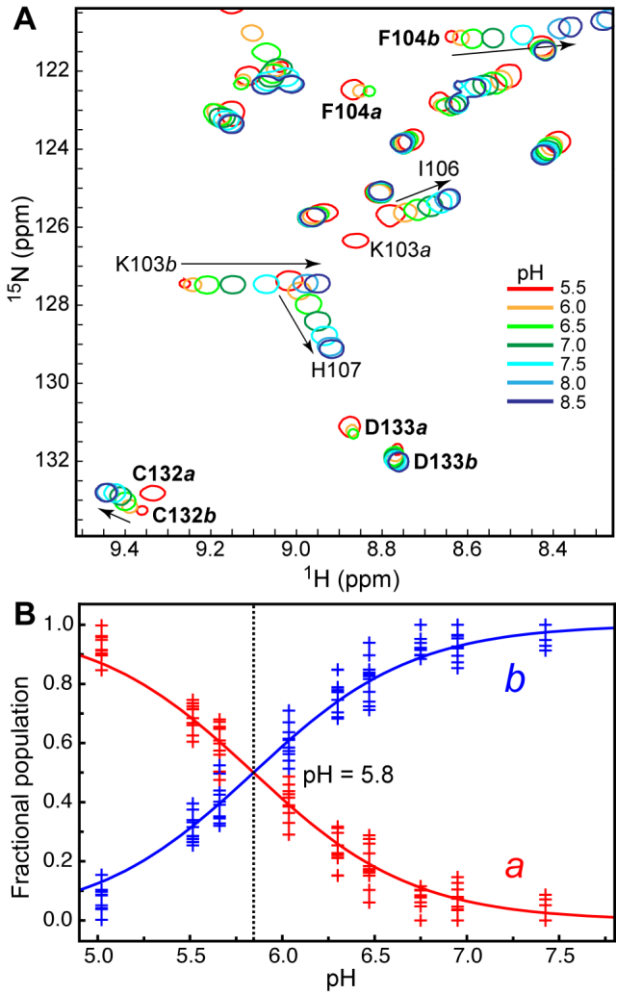

Figure 39. pH dependence of the C1Bα50 HSQC spectra. (A) Expansion of the ^{15}N-^{1}H HSQC spectra showing examples of residues with fast and/or slow exchange behavior. (B) pH dependence of populations *a* and *b*. The fractional populations were calculated using the cross-peak volumes of all residues that have well-resolved peaks in the two conformations. The solid line represents a global fit of the data to Equation 18 and Equation 19.

For all protein residues that are not subject to extensive line-broadening at high and low pH values, the fractional populations of conformers *a* and *b* were calculated. The fractional populations are plotted against pH in Figure 39B. The solid line represents a global fit of the data to Equation 18 and Equation 19. Equal populations of *a* and *b* are present at pH 5.8. The data indicate that the loss of coordination bond between the Sγ of Cys151 and Zn(2) is a pH-dependent process with an apparent pKa of 5.8. This pKa_{app} value either represents the side-chain pKa of the Cys151 itself, or the pKa of some other ionizable group in the protein. The most likely candidates would be titratable histidine residues – their average pKa value in proteins is 6.6, with a standard deviation of 1.[147]

To test if any of the five histidines are responsible for the pH dependence of the conformational exchange, the titration curves for all pH-responsive residues were constructed by plotting the change in ^{15}N and ^{1}H chemical shifts as a function of pH. The NMR-detected titration curves for His107, His117, and His127 are shown in Figure 40. The three histidines titrated with pKa values of 6.7 ± 0.1 (His107), 5.6 ± 0.1 (His117), and 6.1 ± 0.1 (His127). None of these residues are in slow exchange on the NMR chemical-shift timescale.

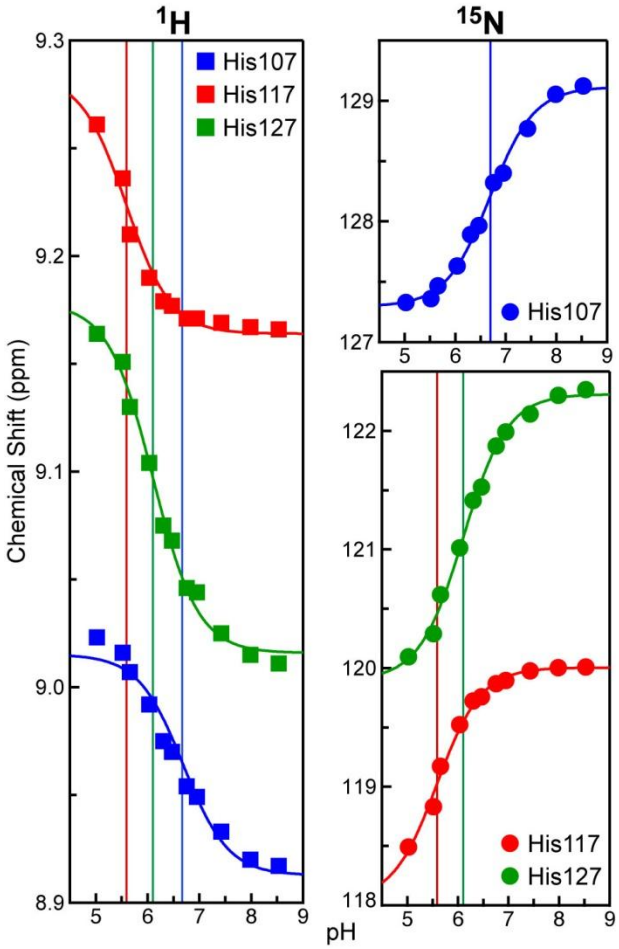

Figure 40. ^{1}H and ^{15}N-detected pH titration curves of His107, His117, and His127. Vertical lines mark the corresponding pKa values. Curves are a result of fitting to Equation 16.

The two remaining histidines – His102 and His140 – coordinate Zn(2) and Zn(1), respectively. The amine group of the N-terminal His102 is not detectable in the NMR spectra. The backbone cross-peak of His140 is in slow exchange between the populations *a* and *b* (see Figure 38A). To estimate the pKa values of His102 and His140, fHSQC[106] experiments tuned for the detection of side-chain resonances were collected.[148,149] The NMR spectra at two pH values, 4.7 and 7.0, and the table of chemical shifts are given in Figure 41. The $N^{\delta 1}$ and $N^{\varepsilon 2}$ shifts at both pH values are consistent with those observed for the Zn^{2+}-coordinated histidines in proteins.[150-152] There is no indication that the protonation state of either His102 or His140 side-chain changes in the pH range from 4.7 to 7.0. This means that the pKa values of His102 and His140 are less than 4.7.

Based on these results, the histidine residue(s) can be ruled out as the primary ionizable group with pKa_{app} of 5.8. The pH dependence of the conformational exchange process likely stems from the de-protonation of the Cys151 side-chain that occurs concomitantly with the loss of its coordination bond with Zn(2). Hence, the pKa_{app} of Cys151 in the C1Bα50 is 5.8.

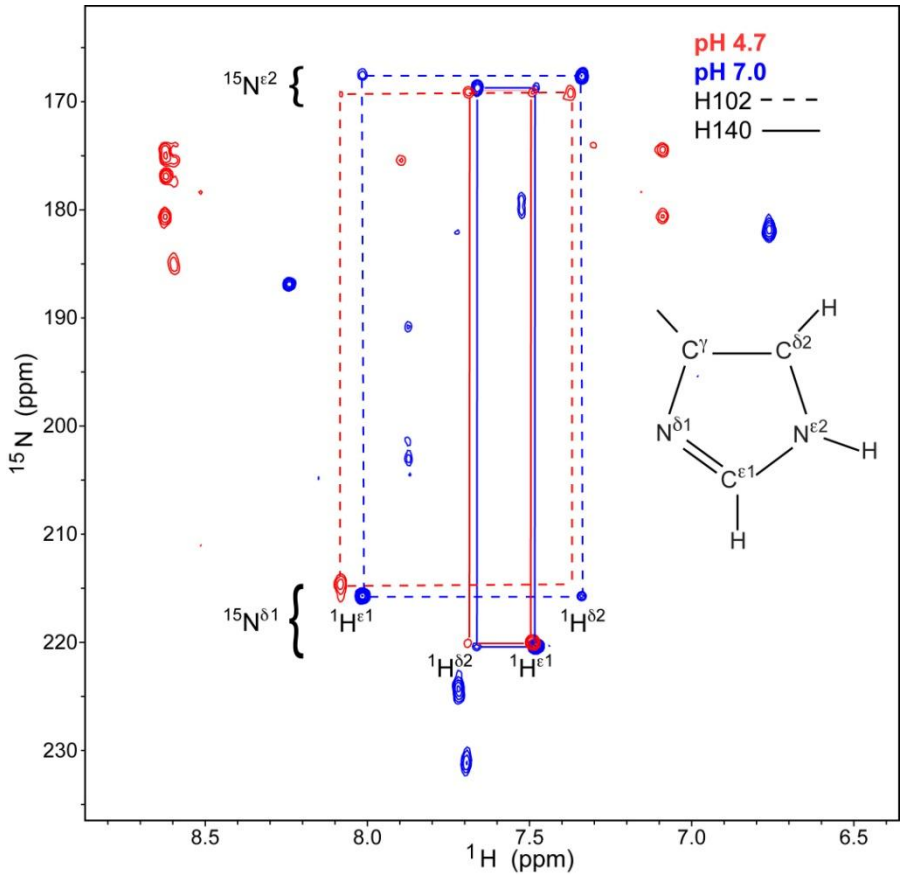

Nucleus	His102		His140	
	pH = 4.7	pH = 7.0	pH = 4.7	pH = 7.0
$^{15}N^{\delta 1}$	215.1	216.2	220.6	220.9
$^{15}N^{\varepsilon 2}$	168.9	167.2	168.8	168.4
$^{1}H^{\delta 2}$	7.37	7.34	7.69	7.66
$^{1}H^{\varepsilon 1}$	8.09	8.02	7.49	7.48

Figure 41. Histidine side-chain pH titration. Overlay of the C1Bα50 ^{15}N-^{1}H fHSQC spectra at pH 7.0 (blue) and 4.7 (red). The cross-peaks corresponding to the side-chains of the Zn^{2+}- coordinating histidines His102 and His140 are connected with dashed and solid lines, respectively. The chemical shifts are summarized in the table.

There is an ionizable group with pKa 7.1-7.2

In addition to three histidine side-chains, another ionizable group was detected with an apparent pKa of 7.2 ± 0.1 in C1Bα50 and 7.1 ± 0.1 in C151G. The NMR-detected titration curves for the residues that responded to this pKa are given in Figure 42A. The parameters of the individual fit to Equation 16 or Equation 17 are summarized in Table 5. It is evident that the C151G variant mirrors the behavior of conformer *a* of C1Bα50 and thereby enables probing of the "high-pH" response of conformer *a*, whose population in the wild-type protein becomes less than 10% at pH 7.0.

The residues responding to the ionizable group with pKa 7.1-7.2 are mapped onto the ensemble-averaged NMR structure in Figure 42B. The responsive residues are located in the vicinity of the Zn(2) coordination sphere, which comprises Cys132, Cys135, His102, and Cys151.

The assignment of the functional group with pKa 7.1-7.2 is ambiguous. There are four possible candidates for this ionizable group: the C-terminal carboxyl, N-terminal amine, Cys135, and Zn^{2+}-coordinated water molecule. The carboxyl and amine groups are the least likely candidates because they are solvent exposed and hence unlikely to have perturbed pKa values. In addition, the most C-terminal residues, Cys151 in C1Bα50 and Gly151 in C151G, do not respond to the pKa of 7.1-7.2.

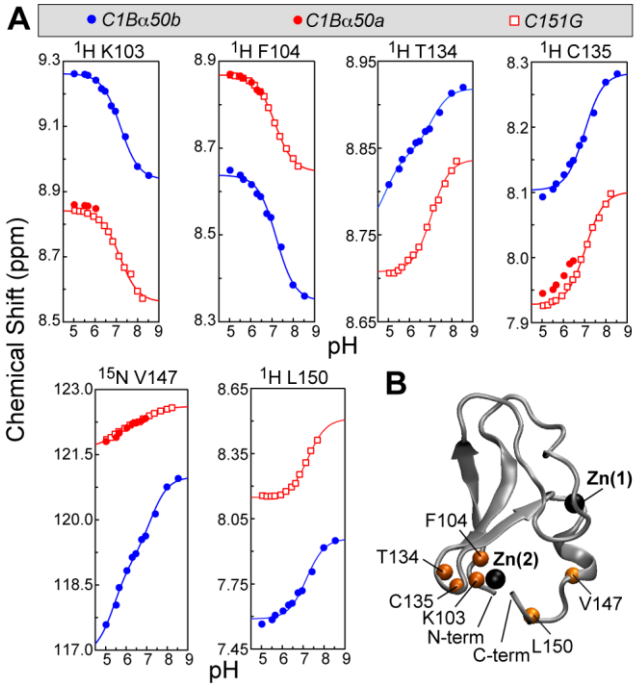

Figure 42. pH titration of an ionizable group close to Zn(2). (A) NMR-detected pH titration curves for the nuclei/residues that respond to the protonation event with an apparent pKa of 7.1-7.2 in C1Bα50 and C151G. Low-pH points for L150*a* and T134*a* could not be obtained because of the peak broadening/overlap. (B) N-H_N groups of residues in (A) mapped onto the C1Bα structure.

Table 5. pKa values determined from fitting of residues in Figure 42.

Residue	*pKa, C1Bα50 b*	*pKa, C151G*
K103	7.2 ± 0.1	7.2 ± 0.1
F104	7.2 ± 0.1	7.1 ± 0.1
T134	7.4 ± 0.1 5.4 ± 0.1	7.0 ± 0.1
C135	7.0 ± 0.1	7.0 ± 0.1
V147	7.4 ± 0.1 5.6 ± 0.1	7.2 ± 0.1 5.4 ± 0.1
L150	7.2 ± 0.1	7.2 ± 0.1

The prerequisite for Cys135 being the primary ionizable group is that its thiol – not thiolate – is involved in coordination with Zn(2). The thiol versus thiolate

coordination in structural Zn^{2+} sites has been a subject of much discussion in the literature.[153-156] According to the *ab initio* calculations, the structural signature of thiol coordination is the increase of the Sγ–Zn distance by 0.3-0.4 Å.[156] In the same study, the Zn^{2+} sites in a homologous C1B domain from PKCδ (PDB ID 1PTQ[22]) were identified as having a geometry compatible with thiol coordination. The longest Sγ–Zn distance, 2.51 Å, was observed in Cys264; the equivalent of this residue in C1Bα is Cys135.

Another viable candidate is a Zn^{2+}-coordinated water molecule. A conversion of Cys151 side-chain to the thiol form in the C1Bα50*a* conformer or its replacement with Gly in the C151G variant creates a coordination vacancy in the Zn(2) site. Given the solvent accessibility of Zn(2), a water molecule will most likely fill this vacancy. Coordination of water by Zn^{2+} depresses its pKa to ~7.[157,158] The presence of water in the coordination sphere of Zn(2) in C1Bα50*b* would require a distortion of the tetrahedral geometry to accommodate an extra ligand. This distortion was observed in C1Bα molecular dynamics simulations.[97]

Kinetics and thermodynamics of the Cys151Sγ–Zn(2) bond formation

The formation of the Cys151Sγ–Zn(2) bond can be represented as an inter-conversion between conformer *a*, in which Sγ is a thiol, and conformer *b*, in which Sγ is a thiolate coordinated to Zn(2). The pH dependence of the process is incorporated into the pseudo-first order rate constant to reflect the constant pH values in the sample maintained by the buffering agent.

To characterize the exchange process between *a* and *b*, the populations of the conformers was adjusted to roughly equal parts by setting the pH to 5.75. At this pH,

the equilibrium constant K_{app} obtained by direct integration of *a* and *b* peaks in the NMR spectra, is 1.15 at 25 ˚C. Within the experimental error, $K_{app} = \exp[-\Delta G^0/RT]$ does not depend on temperature in the investigated temperature range, from 10 to 30 ˚C. This means that the enthalpic contribution to the ΔG^0 of the exchange reaction is rather small. Given a rather modest value of ΔG^0 associated with $K_{app} \approx 1.2$, it can be concluded that both ΔH^0 and ΔS^0 make small individual contributions to ΔG^0 rather than acting via an enthalpy-entropy compensatory mechanism.

Two-dimensional ZZ-exchange NMR experiments were used to characterize the kinetics of C1Bα50 inter-conversion between conformations *a* and *b*. These experiments probe the slow exchange processes with k_{ex} values in the range from 0.1 to 10 s^{-1}. k_{ex} is the sum of the forward and reverse rate constants, k_1 and k_{-1}'.

The expansions of the ZZ-exchange spectra showing the behavior of Cys151 peaks at two mixing times, 70 ms and 360 ms, are presented in Figure 43A. The gradual build-up of the cross-peaks due to exchange between populations *a* and *b* is evident. To enable the determination of activation parameters, the ZZ-exchange experiments were carried out at 5 temperature values. For each temperature and mixing time, the parameter Ξ was calculated according to Equation 12. Ξ is plotted against the mixing time in Figure 43B, with solid lines showing the fits to Equation 13.

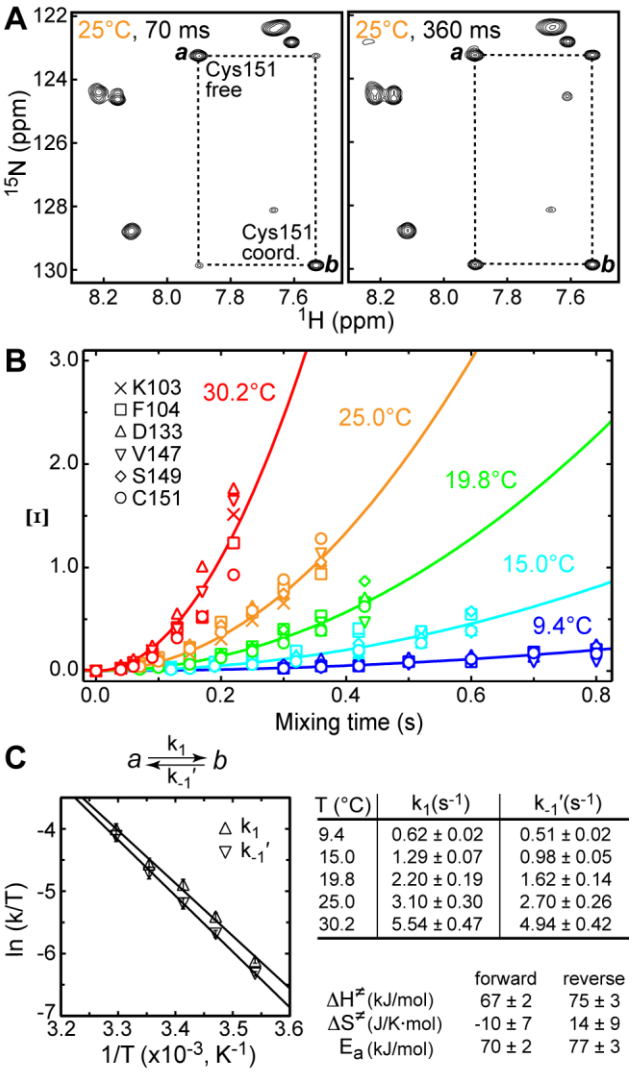

T (°C)	k_1 (s^{-1})	k_{-1}' (s^{-1})
9.4	0.62 ± 0.02	0.51 ± 0.02
15.0	1.29 ± 0.07	0.98 ± 0.05
19.8	2.20 ± 0.19	1.62 ± 0.14
25.0	3.10 ± 0.30	2.70 ± 0.26
30.2	5.54 ± 0.47	4.94 ± 0.42

	forward	reverse
$\Delta H^{\neq}$ (kJ/mol)	67 ± 2	75 ± 3
$\Delta S^{\neq}$ (J/K·mol)	-10 ± 7	14 ± 9
E_a (kJ/mol)	70 ± 2	77 ± 3

Figure 43. Kinetics of Cys151 inter-conversion between thiolate and thiol forms. (A) Expansions of the ZZ-exchange spectra showing the buildup of the Cys151 exchange cross-peaks at two mixing times, 70 and 360 ms. (B) Ξ at pH = 5.75 as a function of mixing time and temperature. Solid lines are the fits to Equation 13. (C) Eyring plots for the forward (k_1) and reverse (k_{-1}') kinetic rate constants that are summarized in the table. $\Delta H^{\neq}$, $\Delta S^{\neq}$, and E_a are the activation enthalpy, entropy, and energy, respectively.

The rate constants k_1 and k_{-1}' calculated from Ξ and K_{app} are summarized in the table of Figure 43C. The temperature dependence of k_1 and k_{-1}' was used to construct the Eyring plots shown in the same figure. The fit of these plots generated the enthalpy and entropy of activation, $\Delta H^{\neq}$ and $\Delta S^{\neq}$. These values are given in Figure 43C for the forward and reverse reactions. In both cases, the $\Delta S^{\neq}$ values are close to zero, which indicates that the total number of degrees of freedom available to the system does not change significantly between the transition state and the corresponding ground state.

The Arrhenius analysis was carried out to obtain the activation energies of Cys151Sγ–Zn(2) bond formation/breakage: 70 and 77 kJ/mol for the forward and reverse reactions, respectively. These energies are rather large, giving rise to small values of the kinetic rate constants; extrapolation of the data to 37 ˚C produces the rate constants of ~9.6 s^{-1}.

Elimination of one thiolate ligand alters the C1Bα dynamics

To determine the consequences of Zn(2) losing one of its protein ligands on the C1Bα dynamics, backbone relaxation parameters (R_1, R_2, and ^1H-^{15}N NOE) were obtained for the C151G and C1Bα50 variants at pH 6.5.

Residue-specific transverse relaxation rate constants, R_2, report on the sub-nanosecond (sub-ns) dynamics of N-H_N groups through their dependence on the spectral density function J sampled at three frequencies: 0, ω_H, and ω_N, where ω_H (ω_N) are the Larmor frequencies of ^1H (^{15}N). In addition, conformational exchange processes that occur on the microsecond-to-millisecond (μs-ms) timescale contribute to R_2 via the R_{ex} term. For proteins with moderate rotational diffusion anisotropy like C1Bα, elevated R_2

values indicate that a particular N-H_N group is subject to chemical exchange, i.e. its $R_{ex} > 0$.

In Figure 44A, the differences in site-specific R_2 values are plotted for C151G and C1Bα50*b*. Many residues in C151G have elevated R_2 values compared to those in C1Bα50*b*. This behavior indicates an increase in the μs-ms conformational dynamics of the protein backbone. The perturbed residues belong to the N-terminal region (Lys103 and Phe104), the QG motif (Gly129), Zn(2) "knuckle" and its vicinity (Asp133, Cys135, Asp136, Met137), and the C-terminal helix (Cys143, Ile145, Val147). Mapping ΔR_2 values onto the C1Bα structure illustrates that most of the dynamically perturbed residues are clustered at the bottom half of C1Bα near the Zn(1) and Zn(2) structural sites (Figure 44B).

To compare the high-frequency motions in C1Bα constructs, the residue-specific spectral density values $J(0.87\omega_H)$ were calculated using the reduced spectral density mapping approach. ω_H was $2\pi \times 600$ MHz for all relaxation experiments. $J(0.87\omega_H)$ values report on the sub-nanosecond dynamics of the N-H_N groups of the protein backbone. Figure 44C compares the $J(0.87\omega_H)$ values for the two C1Bα constructs at pH 6.5. The spectral density profile is mostly flat throughout the primary structure and does not differ significantly between the variants. However, the C-terminal region spanning the Val147-Cys151 segment shows a high degree of flexibility. C151G, with its uncoordinated C-terminus, has the largest value of $J(0.87\omega_H)$. The dynamics of

Cys151 in C1Bα50*b* is attenuated due to its coordination to Zn(2), but Leu150 retains substantial mobility.

In summary, eliminating one protein ligand from the Zn(2) coordination sphere results in the increase of the backbone dynamics of C1Bα on at least two timescales: sub-ns and μs-ms. The C-terminal region acquires substantial flexibility on the sub-ns timescale when not constrained by the thiolate–Zn(2) bond. Residues in the vicinity of the Zn(1) and Zn(2) structural sites, including the C-terminal helix, become more dynamic on the μs-ms timescale. The effect is most evident for Asp133 and Asp136 of the Zn(2) "knuckle" motif (Figure 44A). Adding Zn^{2+} to the C151G NMR sample had little effect on the R_2 values. This means that the conformational exchange in C151G is not due to the inter-conversion between Zn^{2+}(2)-bound and Zn^{2+}(2)-free forms. The identity of the conformer sampled by C151G remains to be determined.

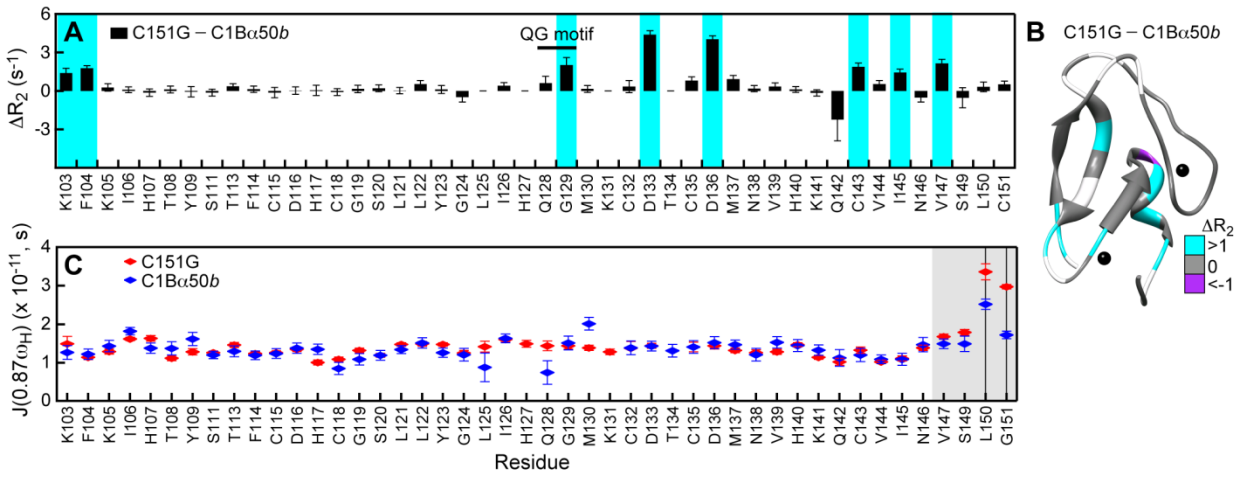

Figure 44. Elimination of Cys151 ligand perturbs the C1Bα dynamics. (A) ΔR_2, calculated as the difference between the residue-specific R_2 values of C151G and those of C1Bα50*b* are plotted against the primary structure. Residues that experienced > 1 s^{-1} increase in R_2 values in the C151G variant are highlighted in cyan. (B) ΔR_2 for the C151G and C1Bα50*b* pair mapped onto the three-dimensional structure of C1Bα. Residues, for which ΔR_2 values are not available, are in shown in white. (C) Spectral density values $J(0.87\omega_H)$ for C151G and C1Bα50*b*. The C-terminal region, highlighted in grey, is flexible on the sub-ns timescale. The vertical lines mark two residues for which the differences in flexibility between the constructs are most pronounced, Leu150 and Cys151.

Zinc coordination dynamics occur on a faster timescale in longer constructs

The studies of PKCα C1B domain in Chapter II were conducted on a 53 residue construct which contains an additional two N-terminal residues (Ser and Lys) and one additional C-terminal residue (Gly) as shown in Figure 45A. This construct does *not* have two slow exchanging populations. The difference plots between the N-H_N chemical shifts of C1Bα53 and those of *a* and *b* conformers of C1Bα50 are given in Figure 45B. It is evident from the plots that the chemical shift differences between the constructs are quite substantial in the N- and C-terminal regions. Moreover, extending C1Bα50 by three amino acids does not lock the protein in conformation *b*. In fact, for some residue/nuclei combinations, the pattern of chemical shift perturbations has opposite signs for *a* and *b*. These residues are highlighted with gray in Figure 45B; the most dramatic examples are shown in HSQC overlays of C1Bα50 and C1Bα53 in the insert. This pattern suggests the presence of a dynamic averaging process in C1Bα53 that is fast on the NMR chemical-shift timescale and involves protein conformations similar (but not identical) to those of *a* and *b* of the C1Bα50. The elevated R_2 values observed for the C-terminal residues in C1Bα53 lend support to the existence of this dynamic process.

R_2 measurements of C1Bα53 in chapter II show elevated R_2 values for residues in the C-terminus. Elevated R_2 is indicative of conformational exchange on a microsecond to millisecond timescale. This chemical exchange process was too fast to be characterized by ^{15}N relaxation dispersion experiments. It is tempting to speculate that the elevated R_2 values reflect the conformational exchange between two C-terminal

conformations that are similar to those in conformers *a* and *b* of C1Bα50. Consistent with this theory, the C151G mutant and C1Bα50*b* which represent the two conformations in exchange have decreased R_2 for residues in the C-terminus, as shown in Figure 46. This is expected because the process is on the seconds timescale in C1Bα50 instead of the microsecond to millisecond timescale. The increased disorder in the C-terminal region compared to the core residues of C1Bα53 as reported by the order parameter in chapter II, also indicates the C-terminus is not restricted by zinc coordination like the other zinc coordinating residues, even in this longer construct.

However, unlike the C1Bα50 exchange, the process in C1Bα53 is not pH dependent. A pH titration of C1Bα53 observed by HSQC revealed the cross-peak position, which represents the average of two exchanging conformations, does not shift between positions representative of conformation *a* and *b* in C1Bα50. This could be due to the Zn(2) being more shielded from solvent from the addition of three amino acids adjacent to the zinc coordinating residues. In addition, the positively charged Lys101 which is not present in C1Bα50 (Figure 45A), could stabilize the negatively charged Cys_3His coordination sphere of Zn(2). Also, evident from the pH titration was the presence of the ionizable group with pKa of 7.4 in the vicinity of Zn(2). The change in chemical shift for residues which show a strong response to this pKa are plotted in Figure 47. This indicates some solvent accessibility still exists in the Zn(2) site in order for ionization to occur of either a zinc coordinated water molecule or zinc coordinated Cys135 if this is the same ionizable group present in C1Bα50.

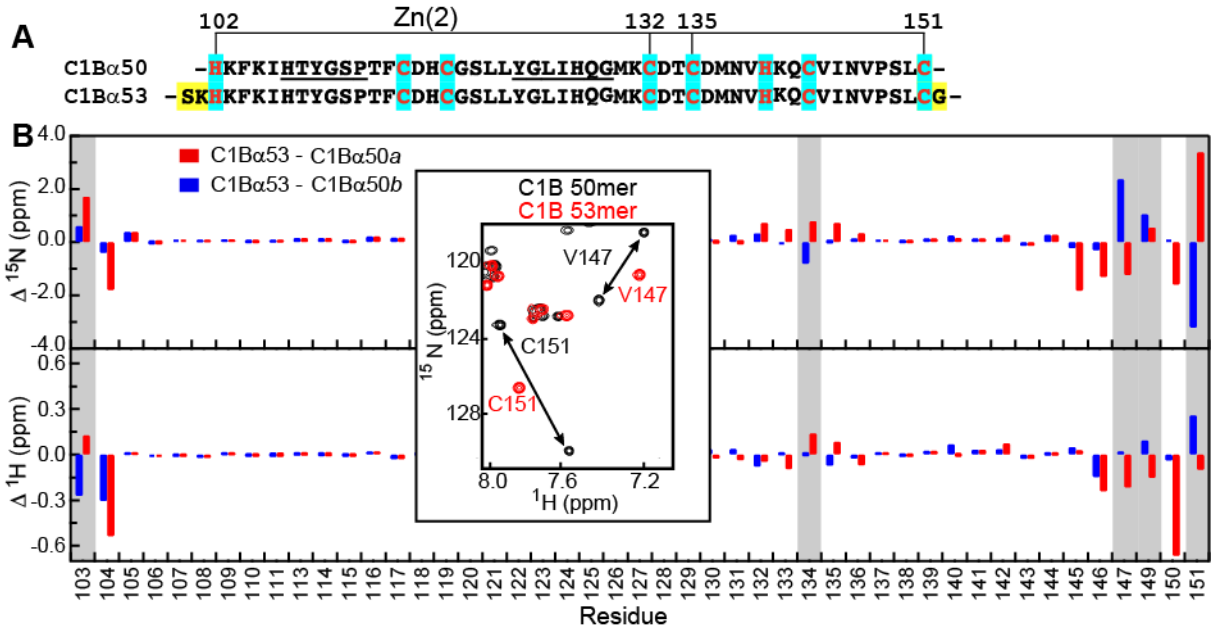

Figure 45. C1Bα50 versus C1Bα53. (A) Comparison of C1Bα50 and C1Bα53 primary structures. Zn^{2+}-coordinating residues are highlighted in cyan; amino acids that are different between the constructs are highlighted in yellow. (B) Chemical shift differences between C1Bα53 and those of the C1Bα50 *a* and *b* conformers. Residues 112 and 148 are prolines with no N-H_N groups. Amino acids, for which chemical shift perturbations with opposite signs were observed for at least one nucleus, are highlighted in grey. For clarity of presentation, identical chemical shifts are used for the C1Bα50 residues whose shifts are coincident in populations *a* and *b*.

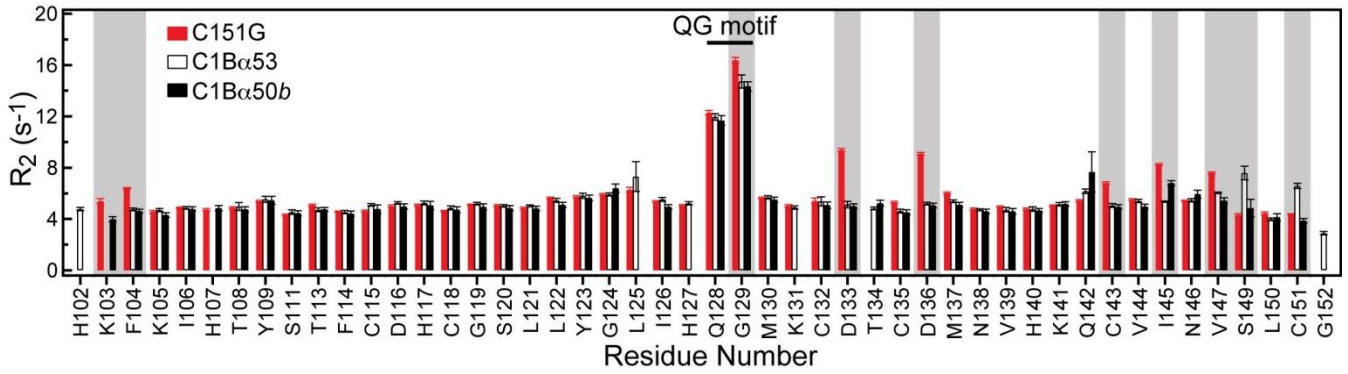

Figure 46. Transverse relaxation rate constants R_2 measured for three C1Bα variants: C1Bα50*b*, C151G, and C1Bα53. The conserved QG motif, whose dynamics is important for ligand binding, has elevated R_2 values in all three constructs. Residues with significantly perturbed conformational dynamics in either C151G or C1Bα53 are shaded.

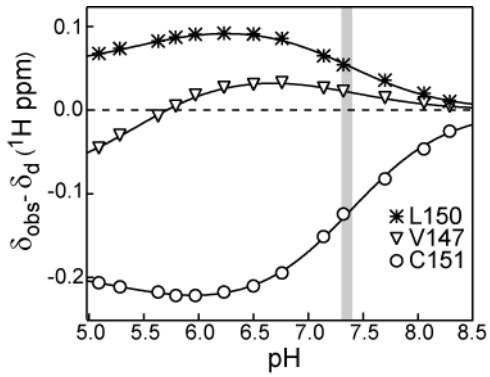

Figure 47. Zn(2) site is solvent accessible in C1Bα53. The difference between the observed chemical shift and the chemical shift of the deprotonated form corrected for the gyromagnetic ratio of ^{1}H for residues significantly affected by ionization with pKa of 7.4 in C1Bα53. Curves represent a fit to Equation 17.

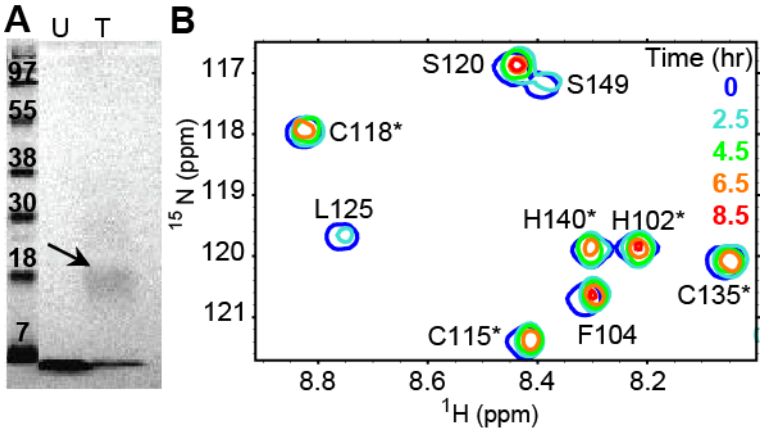

Figure 48. C1Bα53 is reactive. (A) C1Bα53 untreated (U) and treated (T) with PEG-MAL and (B) H_2O_2 as observed by SDS PAGE gel and NMR HSQC spectra overlay respectively. (*) denotes zinc coordinating residues.

To determine if Cys151 is still reactive in C1Bα53, the reactivity of C1Bα53 was tested in the same manner as C1Bα50. The same PEG-MAL exposure was conducted on C1B53mer and two higher molecular weight products appear just as in C1Bα50 (Figure 36 and Figure 48A). Sensitivity to reactive oxygen species was monitored with HSQC spectra taken after H_2O_2 exposure. C1Bα53 peaks also disappear with time, however the rate is more similar to C1B-C2 than C1Bα50 (Figure 34 and Figure 48B). This is consistent with the theory that the three additional residues provide some solvent protection of Cys151, but it remains reactive regardless of the construct length.

Thiolate-to-thiol conversion of Cys151 "opens up" the C1Bα domain

To evaluate the effect of the loss of Cys151-Zn(2) coordination on secondary structure, the temperature dependence of the chemical shifts was measured for both conformations. HSQC spectra of C1Bα50 collected at 9.4, 15.0, 19.8, 25.0, 30.2, and 35.4 ºC are overlaid in Figure 49. The temperature coefficients of ^1H_N calculated from those spectra ranged from -15.5 (Ile145*a*) to 0.2 (His117) ppb/K. According to the previous reports, the coefficients more positive than -4.5[159] or -5 ppb/K[160] are typical for amide protons engaged in hydrogen-bonding interactions. Ser149 is the only residue in C1Bα50*a* and C1Bα50*b* that crosses the -5 ppb/K "cutoff": its temperature coefficient changes from -4.3 ppb/K in conformation *b* to -8.8 ppb/K in conformation *a*. The amide group of Ser149 does not have any hydrogen-bonding partners in the known C1Bα structure. It is likely the loss of Cys151Sγ–Zn(2) coordination bond does not significantly alter the hydrogen-bonding network of C1Bα50.

To determine if the conversion of Cys151 into the thiol form affects the protein structure in non-secondary structure elements, refinement was carried out using the existing NMR structure of C1Bα and the residual dipolar couplings (RDCs) measured for conformers *a* and *b*. It was evident from the HSQC spectra and temperature titrations that the overall protein fold was preserved upon Cys151 protonation and that the conformational changes were not drastic. For such cases, the RDC-based approach is more efficient than the de novo structure determination.

The RDC measurements were carried out simultaneously for both conformers on the same protein sample with pH of 5.75. A total of 228 and 210 RDCs were measured for C1Bα50*b* and C1Bα50*a*, respectively. The largest differences between the RDC values of conformers *a* and *b* were observed in the C-terminal region of the protein. An example is given in Figure 50A for the two residues, Ser149 and Cys151. The splitting between the cross-peaks is the sum of the one-bond J-coupling constant, $^{1}J_{NH}$, and the residual dipolar coupling, $^{1}D_{NH}$. Because the $^{1}J_{NH}$ coupling constants are fairly uniform for all amide groups (~92 Hz), the differences in the observed splittings mostly reflect the differences in RDCs.

The data in Figure 44C indicate that the C-terminal region is flexible. To properly account for this flexibility in the refinement procedure, half-open square well RDC potential was used for all dynamic residues in the protein with NOE values less than 0.5. Other important details of the refinement procedure were the use of long-range NOEs to constrain the loop regions and definition of Zn^{2+} coordination geometry. The refinement was carried out as a two-step protocol that included high- and low-

temperature simulated annealing steps. The parameters of the simulated annealing are given in Table 4.

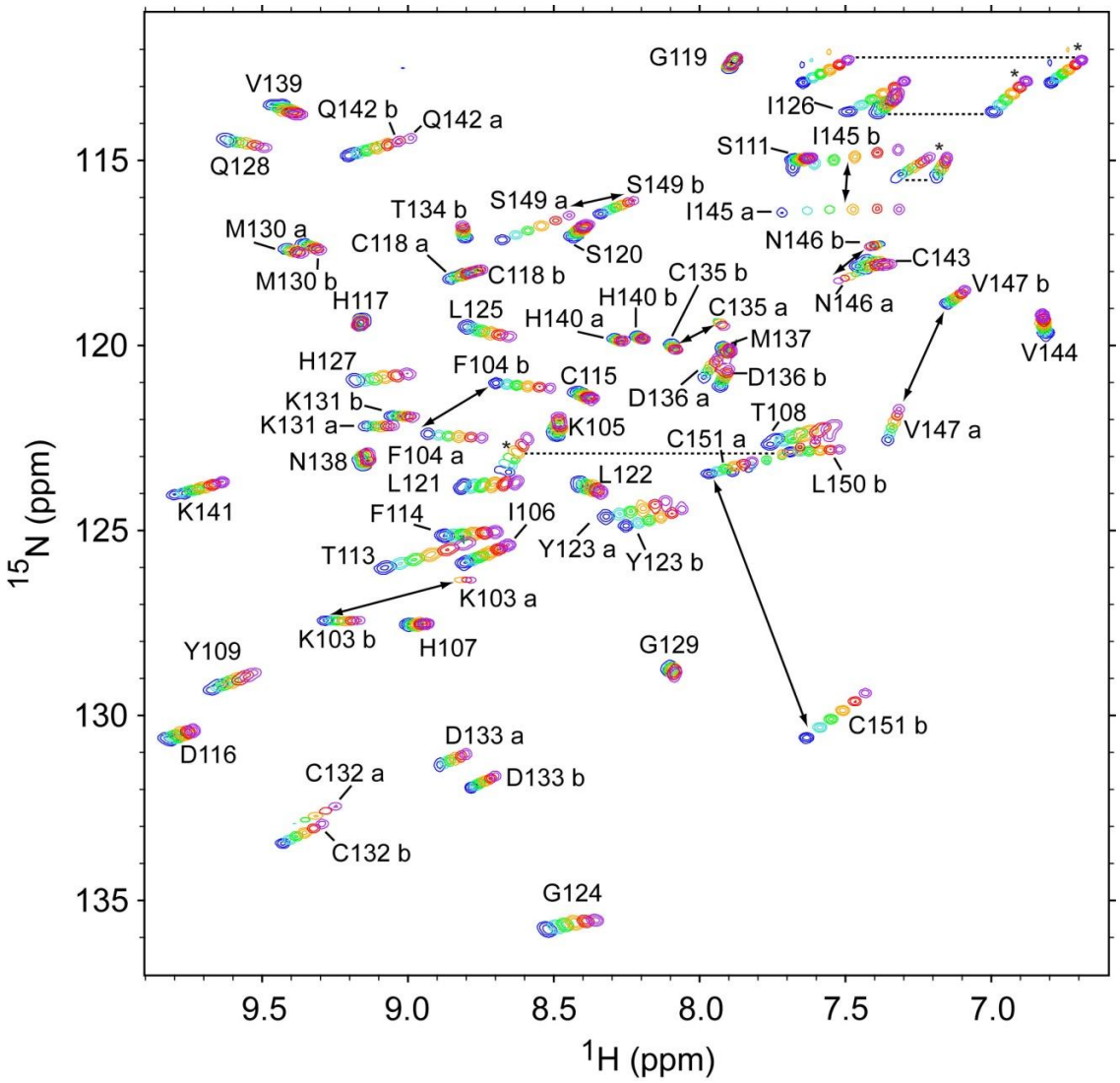

Figure 49. Temperature titration of C1Bα50. An overlay of C1Bα50 HSQC spectra at increasing temperatures from 9.4 (blue) to 35.4 ºC (magenta) in 5º increments.

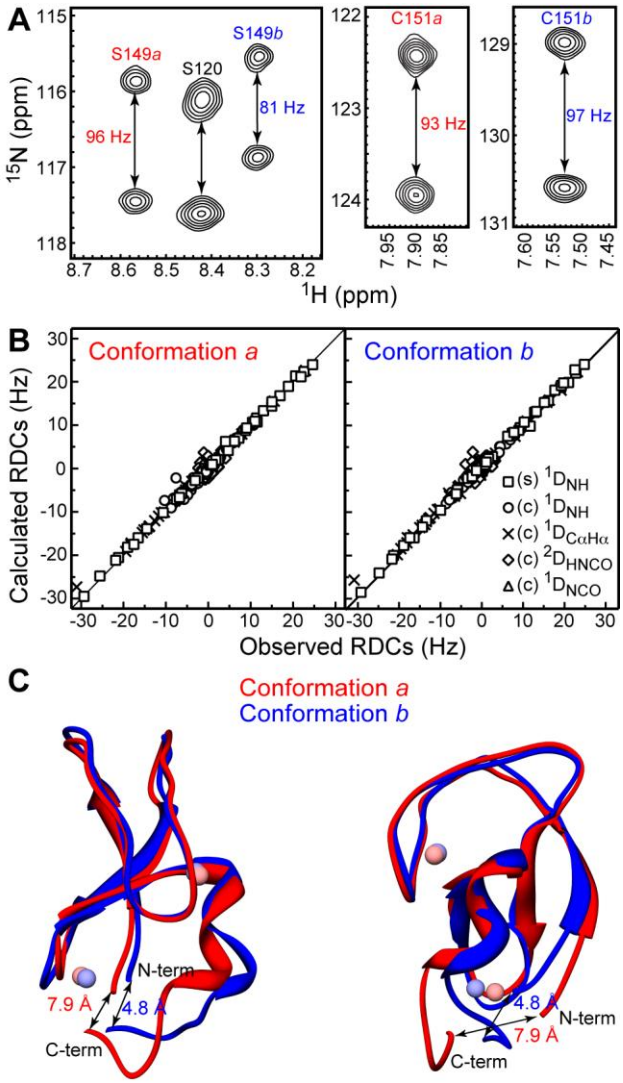

Figure 50. RDC-based structure refinement of C1Bα50*a* and C1Bα50*b*. (A) Expansions of the ^{15}N-^{1}H IPAP spectra of C1Bα50 in stretched gels. The differences between the doublet splittings of Ser149 and Cys151 in conformers *a* and *b* are evident. (B) Calculated versus observed RDCs for stretched (s) and compressed (c) gels. (C) Two views of superimposed regularized average structures of C1Bα50*a* and C1Bα50*b*. The distances between the N- and C-termini are defined as the distances between the Cα atoms of His102 and Cys151.

The agreement between calculated and observed RDCs is shown in Figure 50B. The agreement is excellent for most residues, with the R_{NH} factor of 10% and 6% for the conformers *a* and *b* aligned in the compressed gel. The top 5% of the structures from the low-temperature simulated annealing step were used to generate the regularized average structures given in Figure 50C.

Relative to the starting model, the backbone RMSD values are 1.4 Å for both conformers. These values reduce to 1.0 Å (*b*) and 1.1 Å (*a*) if the N- and C-termini are excluded and only residues 6-44 are used. Superposition of conformers *a* and *b* gives RMSD values of 1.6 Å (residues 1-50) and 1.0 Å (residues 6-44). The structures are essentially super-imposable in the top half that includes ligand-binding loops. The largest differences are observed in the N- and C-terminal regions, as well as the "knuckle" region of the Zn(2) site. The structural changes result in the bottom half of the domain opening up. The distance between the N- and C-termini, measured between the Cα atoms of His102 and Cys151 increases from 4.8 Å to 7.9 Å upon the formation of Cys151 thiol.

The implications of this conformational change for the C1Bα structure and function are two-fold. First, any modification of the Cys151 thiolate is likely to increase the accessibility of the solvent (and other reactants) to the Zn(2) site. Second, the conformational change could be transmitted to the linker region that connects C1Bα to C2 and thereby influence the relative orientation of the two domains.

Discussion

By using NMR to monitor the C1B domain from PKCα it was demonstrated that the C-terminal cysteine (Cys151) is in exchange between a deprotonated zinc coordinated conformation (*b*) and a free protonated conformation (*a*). This was established by the observation that the chemical shifts of the C151G mutant are analogous to the conformation of C1Bα50 at low pH (Figure 38). Dynamics in zinc coordination number and geometry have been reported for proteins with catalytic zinc sites.[161] However, zinc coordination dynamics of a structural zinc site have never been well characterized. NMR of the structural zinc finger from the mengovirus leader protein revealed two conformations of the zinc binding region in slow exchange (lifetimes >1ms),[162] but a direct link to zinc binding dynamics was not established. In a classical zinc finger of a human enhancer binding protein the kinetics of a slow exchange process between one major form and two minor forms was characterized.[163] The two zinc coordinating histidine residues exhibited the largest chemical shift differences between the different populations, but changes in zinc coordination state were never confirmed. Zinc finger proteins play a role in regulation of almost all cellular processes. Thus, further characterization of these dynamics could reveal a wide spread mechanism of regulation.

Similar to the dynamics reported for these structural zinc fingers,[162,163] the 50 amino acid construct of C1B produced NMR spectra with two populations for several residues. The existence of two slowly exchanging conformations was demonstrated with ZZ-exchange NMR (Figure 43). ZZ-exchange calculations reveal the exchange to be

about 3 s^{-1} at pH 5.75 and 25ºC, on the same time scale as the exchange reported by Clore et Al for zinc binding histidines.[163] This indicates a large activation energy for the exchange.

By changing the pH the populations could be reversibly shifted with an apparent pKa of 5.8 (Figure 39), a clear indication that the equilibrium process involves ionization of one the exchanging residues. The only ionizable residues in slow exchange are Lys103 and Cys151. The side-chain of Lys103 is solvent exposed in all of the structures in the NMR ensemble[67] and therefore should have a pKa well above 10. However, Cys151 is predicted to coordinate one of the two structural zinc atoms in C1B (Figure 38C) and not be available for protonation. This result could be explained by Cys151 being solvent exposed in one of the two slow exchanging conformations and thus able to be protonated. To test this hypothesis, a mutant was made in which Cys151 was mutated to glycine, providing a side-chain which is incapable of coordinating zinc. The chemical shifts mimic that of the acidic conformation, consistent with the low pH conformer being protonated and no longer zinc coordinated.

The available structures of C1 domains represent only the Cys151 coordinated conformation. To experimentally determine the structure of the Cys151 exposed conformer, RDCs were collected and used for structure refinement. As hypothesized, the structure determined using population *b* RDCs was the conformer with Cys151 coordinated to zinc and similar to the structures of the other C1 domains that have been determined. The structure that dominates at low pH determined from population *a* RDCs shows significant changes in the structure in the C-terminal region. The

proximity of this region to the following C2 domain provides a potential mechanism for the type of large domain rearrangements that occur upon PKC activation by second messengers. While this structure was determined of the isolated C1B domain, cysteine exposure and reactivity assays (Figure 34, Figure 36, Figure 37, and Figure 48), the presence of an ionizable group with pKa 7.4 (Figure 47), dynamics measurements (Figure 46), as well as molecular dynamics simulation of longer constructs supports similar conformational exchange process in the context of the full length protein.

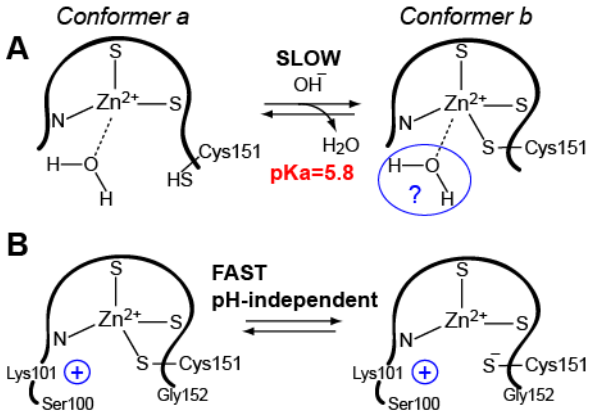

Figure 51. Zn(2) site model in (A) C1Bα50 and (B) C1Bα53. Species represented are those predicted to be the dominate species in solution.

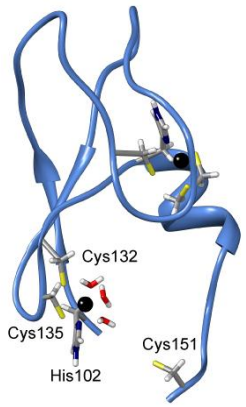

Figure 52. Snapshot taken at the end of the 10ns MD simulation. Zn(2) has octahedral geometry with three coordinated water molecules (shown in red and white) and three coordinated protein residues (His102, Cys132, and Cys135). Cys151 Sγ is 7.1Å from zinc at this time in the simulation.

When Cys151 is not coordinated to zinc, chemistry dictates there be another zinc coordinating ligand. Zinc bound to protein is most commonly coordinated by four ligands, with a fifth ligand not being unusual if one of the ligands is water.[51] Water is the most likely candidate for the additional ligand. This is supported by the C1B residues in close proximity to zinc titrating with a 7.3 pKa (Figure 42), consistent with water that is coordinated to zinc[157]. The same titration behavior is seen in C151G and C1Bα53 (Figure 47) indicating that the water is present in longer constructs and regardless of the zinc coordination state. Figure 51 illustrates this hypothesis for C1Bα50, showing water coordination at low pH and a possible water molecule present even at high pH. C1Bα53 is depicted with the Lys101 stabilizing the zinc coordination sphere, however there is also a possibility of zinc coordinated water in the longer construct as well.

In addition to the experimental evidence, the model presented in Figure 51 is also supported by molecular dynamics simulations of the C1Bα53.[97] The simulations start with a member of the NMR ensemble[67] in which both zinc atoms are tetrahedrally coordinated by one histidine and three cysteine residues. In one trajectory, after 2.6 ns the terminal-zinc adopts trigonal bipyramidal coordination with the histidine, three cysteines, and a water molecule which enters the coordination sphere. A second water molecule enters the coordination sphere at 3.1 ns at which point zinc takes on an octahedral coordination with the histidine, three cysteines, and two water molecule ligands. At 5.8 ns a third water molecule enters the zinc coordination sphere as Cys151 moves away maintaining the octahedral geometry. The same three water molecules remain coordinated to zinc for the remainder of the 10ns simulation. Figure 52 shows a snapshot taken at the end of the 10ns simulation highlighting the three zinc coordinated water molecules and the increased distance between Cys151 and zinc. Once cysteine leaves the zinc coordination sphere the distance from Sγ to zinc varies up to 9.5Å. In an independent 10 ns trajectory, Cys151 lost and then regained zinc coordination twice.

Consistent with the PEG-mal solvent exposure assay which revealed that only Cys151 loses zinc coordination, Zn(1) maintains all four protein ligands in 3 independent MD simulation trajectories. Zn(1) spent most of the time in tetrahedral geometry, but adopted trigonal bipyramidal geometry several times when a very short lived water (0.01-2 ns) entered the Zn(1) coordination sphere. The tetrahedral geometry can be seen clearly at the end of the MD simulation as shown in Figure 52. In this way Zn(1) serves as an internal control to show that loss of Cys151 coordination by the

terminal-zinc is not likely due to the type of zinc interaction model applied during the simulation. The presence of zinc bound water and non-tetrahedral geometry was observed in the simulation regardless of the type of zinc model used. [97] While these simulations were performed on a shorter time scale than the process that leads to the observed conformational exchange in the C1B spectra, the Cys151 zinc coordination dynamics and the presence of zinc bound water mimics the zinc coordination dynamics observed in NMR experiments and cysteine exposure assays.

Exposure of C1Bα50, C1Bα53, C1B-C2 and C151G to a cysteine modification agent, revealed Cys151 is the most solvent exposed cysteine (Figure 36 and Figure 48A). It is also the most reactive cysteine as revealed by treatment with H_2O_2 and IAC (Figure 34, Figure 37, and Figure 48B). Constructs which contained Cys151 reacted faster than C151G. Also evident from these studies is that the C1B domain releases zinc and unfolds upon modification, revealing a possible activation mechanism for PKC proteins. Oxidative conditions *in vivo* and *in vitro* have been shown to activate PKC in the absence of second messengers and lead to the release of zinc,[121,122] however it was unclear how the oxidation agents gained access to the cysteines that were thought to all be tightly coordinated to zinc. The dynamic sampling of a conformation in which Cys151 is solvent exposed provides a possible site for reactive oxygen species attack. The unfolding of the regulatory domain due to modification would likely free PKC from its auto-inhibited state and bring about activation by reactive oxygen species.

In conclusion, this is the first identification and characterization of zinc coordination dynamics in a zinc finger protein. C1Bα50 samples a previously unknown

structure which differs in zinc coordination number and geometry from any known C1 domain structures. This alternate conformation, in which a zinc coordinating cysteine loses coordination and becomes solvent exposed, provides a possible mechanism for PKC activation by oxidative stress. These findings shed new light on the more active functional role that zinc coordination can play in zinc finger proteins.

CHAPTER V

SUMMARY OF FINDINGS AND FUTURE DIRECTIONS

The findings presented here are a significant advancement toward understanding the C1 domain ligand specificities and reactivity and their effect on PKC activity. PKC signaling is involved in the processes of cell division, adhesion, and death. C1 ligand binding is a required step in the canonical PKC activation mechanism. The various regulatory domain ligand affinities and specificities dictate the conditions in which PKC is activated, its localization in the cell, and therefore the signaling cascades that take place that lead to differing cellular events. Controlled cell death and regeneration are key processes in the treatment of many human diseases and disorders; thus understanding PKC regulation is an important step toward developing treatments.

As discussed in Chapter I, several naturally occurring small molecules that bind to the C1 domain have proved useful for treatment of cancer, stroke, and Alzheimer's disease. However, in order to design drugs with a specific mode of action we must first understand how the PKC isoforms are regulated differently. One established difference is the identity of a hydrophobic residue at position 22 in the C1B domain of conventional and novel PKC that dictates the ligand affinity and specificity. To determine how this residue differentially regulates PKC, the structure, dynamics, and ligand binding properties of C1B domains from the conventional PKCα isoform and the novel PKCδ isoform along with position 22 mutants of these constructs are reported in Chapter II.

For both C1Bα and C1Bδ, the identity of residue 22 had little effect on the structure of the domain in the apo-state or bound to ligand as judged by the similarity in chemical shifts and residual dipolar couplings. Measurement of sub-nanosecond dynamics also revealed that fast vibrational motions were not affected by position 22 identity. However, ligand binding studies demonstrated that when Trp is at position 22 in either C1Bα or C1Bδ, the domain increases DOG affinity by more than an order of magnitude compared to Tyr.

Relaxation dispersion experiments revealed conformational exchange in the ligand binding loops in both conventional and novel isoforms in the absence of ligand. However, the rate of exchange is decreased and the number of residues affected by the exchange is increased when Trp is at position 22. Because of the location of the dynamic residues in the ligand binding loop hinges and the role of conserved residues in forming loop stabilizing hydrogen bonds observed in the C1Bδ crystal structure, I hypothesize that the exchange the loops experience is between open and closed conformations. These findings, in combination with available structural information from C1 domains of different PKC isoforms and molecular dynamics simulations, lead to the conclusion that Trp at position 22 stabilizes the higher energy closed loop conformation that is required for binding small ligands, such as diacylglycerol, better than Tyr. This is an important difference established between novel and conventional PKC C1B domains that can be exploited in future drug design studies in order to develop treatments with a single mode of action.

For future studies, it would be useful to determine the structure of both the open and closed loop conformations. This is difficult to accomplish in the apo-state since the high energy closed loop conformation is only weakly populated. However, some insight could be gained by determining the structure of C1 bound to both a small ligand, such as DOG, and a larger ligand, such as PDBu, if the two ligands bind to and stabilize different loop conformations. From these structures it could be possible to determine the interactions of the Trp side-chain that stabilize the closed loop conformation in the apo-state, which are absent when Tyr is at position 22.

Progress toward this objective has already been accomplished and reported in Chapter III. Two conditions of PDBu-bound C1Bα suitable for structure determination were described. The first is a method for efficiently precipitating C1Bα with PDBu for solid-state NMR data collection. The backbone atom assignment of this state is complete and shows that it is a feasible method for determining C1 domain ligand-bound structures. These assignments and chemical shift perturbations reported here can be used as structural restraints for the secondary structure and ligand binding interface. Solution NMR data has been collected in the second condition for an all-atom assignment and NOE restraint calculations of C1Bα bound to PDBu in micelles. The lipid PRE assay described for measuring the depth of C1Bδ insertion in micelles can be applied to this system as an additional structure restraint. Furthermore, these conditions may also be suitable for determining the structure of C1 domains bound to potential drugs, such as the bryostatin compounds. These structural studies could shed a much-

needed light on what dictates the drastic differences reported for C1 domain ligand affinities and specificities.

The identity of the residue at position 22 was also observed to play a role in the interaction with micelles in the absence of a ligand. For the C1Bα constructs, micelle binding of the Trp containing mutant led to intermediate exchange or peak shifting for approximately half the residues in the domain compared to just one ligand binding loop in the case of Tyr. From this drastic change in the number of affected micelle-binding residues it can be concluded that the identity of residue 22 impacts the micelle-binding affinity, structure, or interaction interface. However, because of the intermediate exchange regime, this could not be determined. For C1Bδ constructs, Trp at position 22 increased the affinity for micelles at least 2-3 fold and increased the depth of insertion when compared to Tyr. Because C1 domains likely first insert into the membrane and then undergo a two-dimensional search for membrane bound ligand, these differences in affinity and depth of insertion could play a large role in dictating diacylglycerol binding kinetics. Future simulation and docking studies could take advantage of the experimentally determined depths of insertion for the loop and helix residues to visualize the positioning of the residue 22 side-chain in the membrane-bound structure and assess the binding surface accessibility to a membrane-bound ligand.

In addition to the activation of PKC by regulatory domain membrane binding, PKC signaling is also triggered in response to reactive oxygen species. Chapter IV reports the investigation into the reactivity of C1B in relation to the activation of PKC by reactive oxygen species. Reaction of C1B with hydrogen peroxide, iodoactemide, and

polyethylene glycol maleimide and observation of the products using NMR or gel electrophoresis, showed that modification leads to loss of zinc and protein unfolding. This behavior also persists in the context of the subsequent regulatory domain as demonstrated by the reaction and modification of the C1B-C2 construct. When these experiments were carried out on a Cys151 to Gly mutant (C151G), it is clear Cys151 is the most reactive cysteine in C1B from PKCα. Future investigation of the C151G mutation in the context of the full length PKC under conditions reactive oxygen species signaling could be used to determine the role of Cys151 reactivity *in vivo*. Similar studies could also be used to test the reactivity of the equivalent residue in the C1A domain, Cys86.

The structure, dynamics, and kinetics of an exchange between two conformations in C1Bα50 due to changes in ionization of the Cys151 side-chain were characterized using pH titrations, residual dipolar coupling measurements, relaxation experiments, and zz-exchange NMR experiments. In one conformation, Cys151 side-chain is coordinated to zinc as observed in all available C1 structures. In the second conformation, zinc coordination of Cys151 is lost, and the C-terminal tail adopts a structure in which Cys151 is exposed to solvent. The solvent exposed Cys151 is more accessible to reactive oxygen species; a possible explanation for the observed increase in reactivity. The tail also becomes dynamic on the microsecond-millisecond timescale. Future dynamics studies of the C151G mutant could be done to characterize the conformational exchange in this alternate conformation. Elevated dynamics were also seen in C1Bδ C-terminal residues, but more studies need to be done to determine if the exchange seen in

this isoform is also due to changes in zinc coordination. Taken together, these results suggest that zinc coordination dynamics have an effect on C1B structure and could be a key finding in understanding how PKC is activated under conditions of oxidative stress.

In conclusion, the findings presented here provide insight into the role of the C1B domain in the activation and differential regulation of PKC isoforms. Future investigations using similar methods will be fundamental in elucidating the mechanisms used for complex regulation of other multi-domain signaling proteins.

REFERENCES

(1)Anilkumar, N.; Parsons, M.; Monk, R.; Ng, T.; Adams, J. C. *EMBO J* **2003**, *22*, 5390.

(2)Dempsey, E. C.; Newton, A. C.; Mochly-Rosen, D.; Fields, A. P.; Reyland, M. E.; Insel, P. A.; Messing, R. O. *Am. J. Physiol. Lung Cell. Mol. Physiol.* **2000**, *279*, L429.

(3)Poole, A. W.; Pula, G.; Hers, I.; Crosby, D.; Jones, M. L. *Trends Pharmacol. Sci.* **2004**, *25*, 528.

(4)Newton, A. C. *Biochem. J.* **2003**, *370*, 361.

(5)Mochly-Rosen, D.; Gordon, A. S. *The FASEB Journal* **1998**, *12*, 35.

(6)Braz, J. C.; Gregory, K.; Pathak, A.; Zhao, W.; Sahin, B.; Klevitsky, R.; Kimball, T. F.; Lorenz, J. N.; Nairn, A. C.; Liggett, S. B.; Bodi, I.; Wang, S.; Schwartz, A.; Lakatta, E. G.; DePaoli-Roach, A. A.; Robbins, J.; Hewett, T. E.; Bibb, J. A.; Westfall, M. V.; Kranias, E. G.; Molkentin, J. D. *Nat. Med.* **2004**, *10*, 248.

(7)Masur, K.; Lang, K.; Niggemann, B.; Zanker, K. S.; Entschladen, F. *Mol. Biol. Cell* **2001**, *12*, 1973.

(8)Alkon, D. L.; Sun, M.-K.; Nelson, T. J. *Trends Pharmacol. Sci.* **2007**, *28*, 51.

(9)Hains, A. B.; Vu, M. A. T.; Maciejewski, P. K.; van Dyck, C. H.; Gottron, M.; Arnsten, A. F. T. *Proceedings of the National Academy of Sciences* **2009**, *106*, 17957.

(10)Newton, A. C. *Chemical Reviews* **2001**, *101*, 2353.

(11)Saito, N. In *Protein Kinase C Protocols*; Newton, A., Ed.; Humana Press: 2003; Vol. 233, p 93.

(12)Orr, J. W.; Newton, A. C. *Biochemistry* **1992**, *31*, 4661.

(13)Cho, W.; Stahelin, R. V. *Biochimica et Biophysica Acta (BBA) - Molecular and Cell Biology of Lipids* **2006**, *1761*, 838.

(14)Brodie, C.; Blumberg, P. M. *Apoptosis* **2003**, *8*, 19.

(15)Carrasco, S.; Merida, I. *Mol. Biol. Cell* **2004**, *15*, 2932.

(16)Kazi, J. U.; Soh, J.-W. *Biochem. Biophys. Res. Commun.* **2007**, *364*, 231.

(17)Graybill, C.; Wee, B.; Atwood, S. X.; Prehoda, K. E. *J. Biol. Chem.* **2012**.

(18)Wang, Y.; Seibenhener, M. L.; Vandenplas, M. L.; Wooten, M. W. *J. Neurosci. Res.* **1999**, *55*, 293.

(19)Leonard, T. A.; Ró; ycki, B.; Saidi, L. F.; Hummer, G.; Hurley, J. H. *Cell* **2011**, *144*, 55.

(20)Slater, S. J.; Seiz, J. L.; Cook, A. C.; Buzas, C. J.; Malinowski, S. A.; Kershner, J. L.; Stagliano, B. A.; Stubbs, C. D. *J. Biol. Chem.* **2002**, *277*, 15277.

(21)Stahelin, R. V.; Wang, J.; Blatner, N. R.; Rafter, J. D.; Murray, D.; Cho, W. *J. Biol. Chem.* **2005**, *280*, 36452.

(22)Zhang, G.; Kazanietz, M. G.; Blumberg, P. M.; Hurley, J. H. *Cell* **1995**, *81*, 917.

(23)Sánchez-Bautista, S.; Corbalán-García, S.; Pérez-Lara, A.; Gómez-Fernández, J. C. *Biophys. J.* **2009**, *96*, 3638.

(24)Ananthanarayanan, B.; Stahelin, R. V.; Digman, M. A.; Cho, W. H. *J. Biol. Chem.* **2003**, *278*, 46886.

(25)Zhou, M.; Horita, D. A.; Waugh, D. S.; Byrd, R. A.; Morrison, D. K. *J. Mol. Biol.* **2002**, *315*, 435.

(26)Geczy, T.; Peach, M. L.; El Kazzouli, S.; Sigano, D. M.; Kang, J.-H.; Valle, C. J.; Selezneva, J.; Woo, W.; Kedei, N.; Lewin, N. E.; Garfield, S. H.; Lim, L.; Mannan, P.; Marquez, V. E.; Blumberg, P. M. *J. Biol. Chem.* **2012**, *287*, 13137.

(27)Pu, Y.; Peach, M. L.; Garfield, S. H.; Wincovitch, S.; Marquez, V. E.; Blumberg, P. M. *J. Biol. Chem.* **2006**, *281*, 33773.

(28)Dries, D. R.; Gallegos, L. L.; Newton, A. C. *J. Biol. Chem.* **2007**, *282*, 826.

(29)Ogbourne, S. M.; Suhrbier, A.; Jones, B.; Cozzi, S.-J.; Boyle, G. M.; Morris, M.; McAlpine, D.; Johns, J.; Scott, T. M.; Sutherland, K. P.; Gardner, J. M.; Le, T. T. T.; Lenarczyk, A.; Aylward, J. H.; Parsons, P. G. *Cancer Res.* **2004**, *64*, 2833.

(30)Hampson, P.; Kavanagh, D.; Smith, E.; Wang, K.; Lord, J.; Ed Rainger, G. *Cancer Immunology, Immunotherapy* **2008**, *57*, 1241.

(31)Yi, P.; Schrott, L.; Castor, T.; Alexander, J. *J. Mol. Neurosci.* **2012**, *48*, 234.

(32)Hongpaisan, J.; Sun, M.-K.; Alkon, D. L. *The Journal of Neuroscience* **2011**, *31*, 630.

(33)Sun, M.-K.; Hongpaisan, J.; Nelson, T. J.; Alkon, D. L. *Proceedings of the National Academy of Sciences* **2008**, *105*, 13620.

(34)Sun, M.-K.; Hongpaisan, J.; Alkon, D. L. *Proceedings of the National Academy of Sciences* **2009**, *106*, 14676.

(35)Korin, Y. D.; Brooks, D. G.; Brown, S.; Korotzer, A.; Zack, J. A. *J. Virol.* **2002**, *76*, 8118.

(36)Williams, S. A.; Chen, L.-F.; Kwon, H.; Fenard, D.; Bisgrove, D.; Verdin, E.; Greene, W. C. *J. Biol. Chem.* **2004**, *279*, 42008.

(37)Marquez, V. E.; Blumberg, P. M. *Accounts of Chemical Research* **2003**, *36*, 434.

(38)Truman, J.-P.; Rotenberg, S. A.; Kang, J.-H.; Lerman, G.; Fuks, Z.; Kolesnick, R.; Marquez, V. E.; Haimovitz-Friedman, A. *Cancer Biology & Therapy* **2009**, *8*, 54.

(39)Nakagawa, Y. *Bioscience, Biotechnology, and Biochemistry* **2012**, *76*, 1262.

(40)Wang, Q. J.; Fang, T.-W.; Fenick, D.; Garfield, S.; Bienfait, B.; Marquez, V. E.; Blumberg, P. M. *J. Biol. Chem.* **2000**, *275*, 12136.

(41)Wang, Q. J.; Bhattacharyya, D.; Garfield, S.; Nacro, K.; Marquez, V. E.; Blumberg, P. M. *J. Biol. Chem.* **1999**, *274*, 37233.

(42)Nakagawa, Y.; Irie, K.; Yanagita, R. C.; Ohigashi, H.; Tsuda, K.-i.; Kashiwagi, K.; Saito, N. *J. Med. Chem.* **2006**, *49*, 2681.

(43)Wender, P. A.; Baryza, J. L.; Brenner, S. E.; DeChristopher, B. A.; Loy, B. A.; Schrier, A. J.; Verma, V. A. *Proceedings of the National Academy of Sciences* **2011**, *108*, 6721.

(44)LaValle, C. R.; George, K. M.; Sharlow, E. R.; Lazo, J. S.; Wipf, P.; Wang, Q. J. *Biochimica et Biophysica Acta (BBA) - Reviews on Cancer* **2010**, *1806*, 183.

(45)Yang, C.; Liu, Y.; Coluccio Leskow, F.; Weaver, V. M.; Kazanietz, M. G. *J. Biol. Chem.* **2005**, M411629200.

(46)Yang, D.; Kedei, N.; Li, L.; Tao, J.; Velasquez, J. F.; Michalowski, A. M.; Tóth, B. I.; Marincsák, R.; Varga, A.; Bíró, T.; Yuspa, S. H.; Blumberg, P. M. *Cancer Res.* **2010**, *70*, 7905.

(47)Takeishi, K.; Taketomi, A.; Shirabe, K.; Toshima, T.; Motomura, T.; Ikegami, T.; Yoshizumi, T.; Sakane, F.; Maehara, Y. *J. Hepatol.* **2012**, *57*, 77.

(48)Wilkinson, S.; Paterson, H. F.; Marshall, C. J. *Nat. Cell Biol.* **2005**, *7*, 255.

(49)Heikkila, T.; Wheatley, E.; Crighton, D.; Schroder, E.; Boakes, A.; Kaye, S. J.; Mezna, M.; Pang, L.; Rushbrooke, M.; Turnbull, A.; Olson, M. F. *PLoS ONE* **2011**, *6*, e24825.

(50)Andreini, C.; Banci, L.; Bertini, I.; Rosato, A. *J. Proteome Res.* **2005**, *5*, 196.

(51)Auld, D. S. *Biometals* **2001**, *14*, 271.

(52)Frederickson, C. J.; Koh, J.-Y.; Bush, A. I. *Nat. Rev. Neurosci.* **2005**, *6*, 449.

(53)Li, W.; Zhang, J.; Wang, J.; Wang, W. *J. Am. Chem. Soc.* **2007**, *130*, 892.

(54)Grishin, N. V. *Nucleic Acids Res.* **2001**, *29*, 1703.

(55)Ilbert, M.; Graf, P. C.; Jakob, U. *Antioxid. Redox Signal.* **2006**, *8*, 835.

(56)Kroncke, K. D.; Klotz, L. O. *Antioxid. Redox Signal.* **2009**, *11*, 1015.

(57)Cosentino-Gomes, D.; Rocco-Machado, N.; Meyer-Fernandes, J. R. *Int J Mol Sci* **2012**, *13*, 10697.

(58)Marley, J.; Lu, M.; Bracken, C. *J. Biomol. NMR* **2001**, *20*, 71.

(59)Delaglio, F.; Grzesiek, S.; Vuister, G. W.; Zhu, G.; Pfeifer, J.; Bax, A. *J. Biomol. NMR* **1995**, *6*, 277.

(60)Goddard, T. D.; Kneller, D. G. Computer Software. University of California, San Francisco, 2003.

(61)Muhandiram, D. R.; Kay, L. E. *Journal of Magnetic Resonance, Series B* **1994**, *103*, 203.

(62)Schumann, F.; Riepl, H.; Maurer, T.; Gronwald, W.; Neidig, K.-P.; Kalbitzer, H. *J. Biomol. NMR* **2007**, *39*, 275.

(63)Wilcox, C. S. *Frontiers in Supramolecular Organic Chemistry and Photochemistry* **1991**, 123.

(64)Farrow, N. A.; Muhandiram, R.; Singer, A. U.; Pascal, S. M.; Kay, C. M.; Gish, G.; Shoelson, S. E.; Pawson, T.; Forman-Kay, J. D.; Kay, L. E. *Biochemistry* **1994**, *33*, 5984.

(65)García de la Torre, J.; Huertas, M. L.; Carrasco, B. *Journal of Magnetic Resonance* **2000**, *147*, 138.

(66)Tjandra, N.; Kuboniwa, H.; Ren, H.; Bax, A. *Eur. J. Biochem.* **1995**, *230*, 1014.

(67)Hommel, U.; Zurini, M.; Luyten, M. *Nature Structural and Molecular Biology* **1994**, *1*, 383.

(68)Hall, J. B.; Fushman, D. *J. Biomol. NMR* **2003**, *27*, 261.

(69)Lipari, G.; Szabo, A. *J. Am. Chem. Soc.* **1982**, *104*, 4546.

(70)Mandel, A. M.; Akke, M.; Palmer, I. I. I. A. G. *J. Mol. Biol.* **1995**, *246*, 144.

(71)Cole, R.; Loria, J. P. *J. Biomol. NMR* **2003**, *26*, 203.

(72)Farrow, N. A.; Zhang, O.; Forman-Kay, J. D.; Kay, L. E. *Biochemistry* **1995**, *34*, 868.

(73)Farrow, N. A.; Zhang, O. W.; Szabo, A.; Torchia, D. A.; Kay, L. E. *J. Biomol. NMR* **1995**, *6*, 153.

(74)Peng, J. W.; Wagner, G. *Biochemistry* **1992**, *31*, 8571.

(75)Peng, J. W.; Wagner, G. *Journal of Magnetic Resonance* **1992**, *98*, 308.

(76)Sass, H.-J.; Musco, G.; Stahl, S. J.; Wingfield, P. T.; Grzesiek, S. *J. Biomol. NMR* **2000**, *18*, 303.

(77)Tycko, R.; Blanco, F. J.; Ishii, Y. *J. Am. Chem. Soc.* **2000**, *122*, 9340.

(78)Chou, J. J.; Gaemers, S.; Howder, B.; Louis, J. M.; Bax, A. *J. Biomol. NMR* **2001**, *21*, 377.

(79)Ottiger, M.; Delaglio, F.; Bax, A. *Journal of Magnetic Resonance* **1998**, *131*, 373.

(80)Hwang, T. L.; van Zijl, P. C.; Mori, S. *J. Biomol. NMR* **1998**, *11*, 221.

(81)Hwang, T. L.; Shaka, A. J. *Journal of Magnetic Resonance, Series A* **1995**, *112*, 275.

(82)Piotto, M.; Saudek, V.; Sklenář, V. *J. Biomol. NMR* **1992**, *2*, 661.

(83)Sklenar, V.; Piotto, M.; Leppik, R.; Saudek, V. *Journal of Magnetic Resonance, Series A* **1993**, *102*, 241.

(84)Zhang, O.; Kay, L. E.; Olivier, J. P.; Forman-Kay, J. D. *J. Biomol. NMR* **1994**, *4*, 845.

(85)Lemmon, M. A. *Nat. Rev. Mol. Cell Biol.* **2008**, *9*, 99.

(86)Dries, D. R.; Newton, A. C. *J. Biol. Chem.* **2008**, *283*, 7885.

(87)Vriend, G. *Journal of Molecular Graphics* **1990**, *8*, 52.

(88)Millet, O.; Mittermaier, A.; Baker, D.; Kay, L. E. *J. Mol. Biol.* **2003**, *329*, 551.

(89)Oxenoid, K.; Rice, A. J.; Chou, J. J. *Protein Sci.* **2007**, *16*, 1977.

(90)Xu, R. X.; Pawelczyk, T.; Xia, T.-H.; Brown, S. C. *Biochemistry* **1997**, *36*, 10709.

(91)Hritz, J.; Ulicny, J.; Laaksonen, A.; Jancura, D.; Miskovsky, P. *J. Med. Chem.* **2004**, *47*, 6547.

(92)Steffel, L. R.; Cashman, T. J.; Reutershan, M. H.; Linton, B. R. *J. Am. Chem. Soc.* **2007**, *129*, 12956.

(93)Skalicky, J. J.; Selsted, M. E.; Pardi, A. *Proteins: Structure, Function, and Bioinformatics* **1994**, *20*, 52.

(94)Mori, S.; Abeygunawardana, C.; Berg, J. M.; van Zijl, P. C. M. *J. Am. Chem. Soc.* **1997**, *119*, 6844.

(95)Clore, G. M.; Bax, A.; Wingfield, P. T.; Gronenborn, A. M. *Biochemistry* **1990**, *29*, 5671.

(96)Kleckner, I. R.; Foster, M. P. *Biochimica et Biophysica Acta (BBA) - Proteins and Proteomics* **2011**, *1814*, 942.

(97)Stewart, M. D.; Morgan, B.; Massi, F.; Igumenova, T. I. *J. Mol. Biol.* **2011**, *408*, 949.

(98)Choi, Y.; Pu, Y.; Peach, M. L.; Kang, J.-H.; Lewin, N. E.; Sigano, D. M.; Garfield, S. H.; Blumberg, P. M.; Marquez, V. E. *J. Med. Chem.* **2007**, *50*, 3465.

(99)Shanmugasundararaj, S.; Das, J.; Sandberg, Warren S.; Zhou, X.; Wang, D.; Messing, Robert O.; Bruzik, Karol S.; Stehle, T.; Miller, Keith W. *Biophys. J.* **2012**, *103*, 2331.

(100)Pak, Y.; Enyedy, I. J.; Varady, J.; Kung, J. W.; Lorenzo, P. S.; Blumberg, P. M.; Wang, S. *J. Med. Chem.* **2001**, *44*, 1690.

(101)Kazanietz, M. G.; Wang, S.; Milne, G. W. A.; Lewin, N. E.; Liu, H. L.; Blumberg, P. M. *J. Biol. Chem.* **1995**, *270*, 21852.

(102)van Meer, G.; de Kroon, A. I. P. M. *J. Cell Sci.* **2011**, *124*, 5.

(103)Medkova, M.; Cho, W. *Biochemistry* **1998**, *37*, 4892.

(104)Johnson, J. E.; Giorgione, J.; Newton, A. C. *Biochemistry* **2000**, *39*, 11360.

(105)Steinberg, S. F. *Physiol. Rev.* **2008**, *88*, 1341.

(106)Mori, S.; Abeygunawardana, C.; Johnson, M. O.; van Zijl, P. C. *Journal of Magnetic Resonance. Series B* **1995**, *108*, 94.

(107)Baldus, M.; Petkova, A. T.; Herzfeld, J.; Griffin, R. G. *Molecular Physics* **1998**, *95*, 1197.

(108)Takegoshi, K.; Nakamura, S.; Terao, T. *Chemical Physics Letters* **2001**, *344*, 631.

(109)Pauli, J.; Baldus, M.; van Rossum, B.; de Groot, H.; Oschkinat, H. *ChemBioChem* **2001**, *2*, 272.

(110)Fernández, C.; Hilty, C.; Wider, G.; Wüthrich, K. *Proceedings of the National Academy of Sciences* **2002**, *99*, 13533.

(111)Sanson, A.; Monck, M. A.; Neumann, J.-M. *Biochemistry* **1995**, *34*, 5938.

(112)MacRaild, C. A.; Howlett, G. J.; Gooley, P. R. *Biochemistry* **2004**, *43*, 8084.

(113)Kutateladze, T. G.; Capelluto, D. G. S.; Ferguson, C. G.; Cheever, M. L.; Kutateladze, A. G.; Prestwich, G. D.; Overduin, M. *J. Biol. Chem.* **2004**, *279*, 3050.

(114)Killian, J. A.; von Heijne, G. *Trends Biochem. Sci.* **2000**, *25*, 429.

(115)MacCallum, J. L.; Bennett, W. F. D.; Tieleman, D. P. *Biophys. J.* **2008**, *94*, 3393.

(116)Wimley, W. C.; White, S. H. *Nature Structural and Molecular Biology* **1996**, *3*, 842.

(117)Newton, A. C. *Am. J. Physiol. Endocrinol. Metab.* **2010**, *298*, E395.

(118)Caberoy, N. B.; Zhou, Y.; Alvarado, G.; Fan, X.; Li, W. *Biochem. Biophys. Res. Commun.* **2009**, *386*, 197.

(119)Kuo, W.; Herrick, D. Z.; Cafiso, D. S. *Biochemistry* **2011**, *50*, 2633.

(120)Gopalakrishna, R.; Anderson, W. B. *Proceedings of the National Academy of Sciences U. S. A.* **1989**, *86*, 6758.

(121)Knapp, L. T.; Klann, E. *J. Biol. Chem.* **2000**, *275*, 24136.

(122)Korichneva, I.; Hoyos, B.; Chua, R.; Levi, E.; Hammerling, U. *J. Biol. Chem.* **2002**, *277*, 44327.

(123)Maret, W. *Antioxid. Redox Signal.* **2006**, *8*, 1419.

(124)Janda, I.; Devedjiev, Y.; Derewenda, U.; Dauter, Z.; Bielnicki, J.; Cooper, D. R.; Graf, P. C. F.; Joachimiak, A.; Jakob, U.; Derewenda, Z. S. *Structure* **2004**, *12*, 1901.

(125)Graf, P. C. F.; Martinez-Yamout, M.; VanHaerents, S.; Lilie, H.; Dyson, H. J.; Jakob, U. *J. Biol. Chem.* **2004**, *279*, 20529.

(126)Li, W.; Bottrill, A. R.; Bibb, M. J.; Buttner, M. J.; Paget, M. S. B.; Kleanthous, C. *J. Mol. Biol.* **2003**, *333*, 461.

(127)Newman, J. D.; Anthony, J. R.; Donohue, T. J. *J. Mol. Biol.* **2001**, *313*, 485.

(128)Dinkova-Kostova, A. T.; Holtzclaw, W. D.; Wakabayashi, N. *Biochemistry* **2005**, *44*, 6889.

(129)Butt, T. R.; Edavettal, S. C.; Hall, J. P.; Mattern, M. R. *Protein Expr. Purif.* **2005**, *43*, 1.

(130)Morales, K. A.; Lasagna, M.; Gribenko, A. V.; Yoon, Y.; Reinhart, G. D.; Lee, J. C.; Cho, W.; Li, P.; Igumenova, T. I. *J. Am. Chem. Soc.* **2011**, *133*, 10599.

(131)Yamazaki, T.; Forman-Kay, J. D.; Kay, L. E. *J. Am. Chem. Soc.* **1993**, *115*, 11054.

(132)Lee, W.; Westler, W. M.; Bahrami, A.; Eghbalnia, H. R.; Markley, J. L. *Bioinformatics* **2009**, *25*, 2085.

(133)Farrow, N. A.; Zhang, O. W.; Forman-Kay, J. D.; Kay, L. E. *J. Biomol. NMR* **1994**, *4*, 727.

(134)Miloushev, V. Z.; Bahna, F.; Ciatto, C.; Ahlsen, G.; Honig, B.; Shapiro, L.; Palmer, A. G., 3rd *Structure* **2008**, *16*, 1195.

(135)Hunt, J. B.; Neece, S. H.; Ginsburg, A. *Anal. Biochem.* **1985**, *146*, 150.

(136)Zhao, F.; Ilbert, M.; Varadan, R.; Cremers, C. M.; Hoyos, B.; Acin-Perez, R.; Vinogradov, V.; Cowburn, D.; Jakob, U.; Hammerling, U. *Antioxid. Redox Signal.* **2011**, *14*, 757.

(137)Kosolapov, A.; Deutsch, C. *Nat. Struct. Mol. Biol.* **2009**, *16*, 405.

(138)Webb, H.; Tynan-Connolly, B. M.; Lee, G. M.; Farrell, D.; O'Meara, F.; Sondergaard, C. R.; Teilum, K.; Hewage, C.; McIntosh, L. P.; Nielsen, J. E. *Proteins* **2011**, *79*, 685.

(139)Yang, D.; Tolman, J. R.; Goto, N. K.; Kay, L. E. *J. Biomol. NMR* **1998**, *12*, 325.

(140)Chou, J. J.; Li, S.; Bax, A. *J. Biomol. NMR* **2000**, *18*, 217.

(141)Schwieters, C. D.; Kuszewski, J. J.; Clore, G. M. *Progress in Nuclear Magnetic Resonance Spectroscopy* **2006**, *48*, 47.

(142)N.Tochio, S. K., K.Saito, T.Tomizawa, S.Watanabe, T. Harada, T. Kigawa, S. Yokoyama; Structural Genomics Proteomics Initiative, Ed. 2007.

(143)Cornilescu, G.; Delaglio, F.; Bax, A. *J. Biomol. NMR* **1999**, *13*, 289.

(144)Pettersen, E. F.; Goddard, T. D.; Huang, C. C.; Couch, G. S.; Greenblatt, D. M.; Meng, E. C.; Ferrin, T. E. *Journal of Computational Chemistry* **2004**, *25*, 1605.

(145)Hurley, J. H.; Newton, A. C.; Parker, P. J.; Blumberg, P. M.; Nishizuka, Y. *Protein Sci.* **1997**, *6*, 477.

(146)Kazanietz, M. G.; Wang, S.; Milne, G. W.; Lewin, N. E.; Liu, H. L.; Blumberg, P. M. *J. Biol. Chem.* **1995**, *270*, 21852.

(147)Pace, C. N.; Grimsley, G. R.; Scholtz, J. M. *J. Biol. Chem.* **2009**, *284*, 13285.

(148)Schubert, M.; Poon, D. K.; Wicki, J.; Tarling, C. A.; Kwan, E. M.; Nielsen, J. E.; Withers, S. G.; McIntosh, L. P. *Biochemistry* **2007**, *46*, 7383.

(149)Pelton, J. G.; Torchia, D. A.; Meadow, N. D.; Roseman, S. *Protein Sci.* **1993**, *2*, 543.

(150)Schmiedeskamp, M.; Rajagopal, P.; Klevit, R. E. *Protein Sci.* **1997**, *6*, 1835.

(151)Gooley, P. R.; Johnson, B. A.; Marcy, A. I.; Cuca, G. C.; Salowe, S. P.; Hagmann, W. K.; Esser, C. K.; Springer, J. P. *Biochemistry* **1993**, *32*, 13098.

(152)Urbani, A.; Bazzo, R.; Nardi, M. C.; Cicero, D. O.; De Francesco, R.; Steinkuhler, C.; Barbato, G. *J. Biol. Chem.* **1998**, *273*, 18760.

(153)Fabris, D.; Zaia, J.; Hathout, Y.; Fenselau, C. *J. Am. Chem. Soc.* **1996**, *118*, 12242.

(154)Larabee, J. L.; Hocker, J. R.; Hanas, J. S. *Arch. Biochem. Biophys.* **2005**, *434*, 139.

(155)Dudev, T.; Lim, C. *J. Am. Chem. Soc.* **2002**, *124*, 6759.

(156)Simonson, T.; Calimet, N. *Proteins* **2002**, *49*, 37.

(157)Kiefer, L. L.; Fierke, C. A. *Biochemistry* **1994**, *33*, 15233.

(158)Parkin, G. *Chemical Reviews* **2004**, *104*, 699.

(159)Baxter, N. J.; Williamson, M. P. *J. Biomol. NMR* **1997**, *9*, 359.

(160)Skalicky, J. J.; Selsted, M. E.; Pardi, A. *Proteins-Structure Function and Genetics* **1994**, *20*, 52.

(161)Maret, W.; Li, Y. *ChemInform* **2010**, *41*.

(162)Cornilescu, C. C.; Porter, F. W.; Zhao, K. Q.; Palmenberg, A. C.; Markley, J. L. *FEBS Lett.* **2008**, *582*, 896.

(163)Clore, G. M.; Omichinski, J. G.; Gronenborn, A. M. *J. Am. Chem. Soc.* **1991**, *113*, 4350.